A SPIN-LATTICE DYNAMICS STUDY OF EFFECTS OF MAGNON EXCITATIONS ON PHYSICAL PROPERTIES OF BCC IRON

WEN HAOHUA

Ph. D

The Hong Kong Polytechnic University

2013

The Hong Kong Polytechnic University

Department of Electronic and Information Engineering

A Spin-Lattice Dynamics Study of Effects of Magnon Excitations on Physical Properties of BCC Iron

by

WEN, Haohua

A thesis submitted in partial fulfillment of the requirements

for the degree of Doctor of Philosophy

June, 2012

CERTIFICATE OF ORIGINALITY

I hereby declare that this thesis is my own work and that, to the best of my knowledge and belief, it reproduces no material previously published or written nor material that has been accepted for the award of any other degree or diploma, except where due acknowledgement has been made in the text.

_____ (Signed)

WEN, Haohua (Name of Student)

Dedicate to my wife and parents

Abstract

Spin-lattice dynamics (SLD) study of the effects of spin vibrations on physical properties in body-centred-cubic (BCC) iron has been performed in the thesis. Since the exchange integral governing spin-spin correlation depends on the atomic distance, the degrees of freedom of spin and lattice in BCC iron are coupled, so that the participation of spins leads to the change of anharmonicity of the crystal potential of BCC iron for both lattice dynamics and spin dynamics. Consequently, through the spin-lattice coupling, the enhanced phonon- and magnon scattering give rise to the more softening and shorter lifetimes for both elementary thermal excitations, which are revealed from the dispersion curves for phonons and magnons, respectively. For instance, the spin-lattice coupling results in the shift of Curie temperature from ~1100K to ~1000K. In addition, the spin stiffness confirms such effects in spin dynamics.

By using the thermodynamic integration method, we calculated the free energy and other thermodynamic quantities, e.g. entropy and heat capacity are calculated. The results show that the spin vibrations give rise to not only the energetic contribution, but also entropic contributions, which leads to the anomalous temperature dependence of the thermal, magnetic and mechanical properties in BCC iron, especially near FM/PM phase boundary. Examples are the thermal expansion coefficient, Grüneisen parameter, specific heat, as well as

the isothermal elastic constants. Contributions from spin vibrations are particularly large compared with the effects of multi-phonon interactions.

The effects of spin vibrations are studied in the self- and mono-vacancy diffusion in BCC iron. Based on the scheme of SLD and modified thermodynamics integration (TI) method, the free energies of vacancy migration and formation are calculated over a wide range of temperature, across FM/PM phase boundary in BCC iron, from which the attempt frequency of vacancy migration is calculated for the first time atomistically. The non-Arrhenius behavior of vacancy activation is also first time found from the atomistic simulation, from which the migration enthalpy increases ~0.15eV attributed to the long-range magnetic order. The results are in good quantitative agreement with other calculations and experimental data. Furthermore, the effects of spin vibration on vacancy formation and migration entropies and enthalpies are investigated by using the modified conjugated gradient (MCG) and TI methods. It is found that the change of spin configuration is the principal origin to the energetic change in vacancy migration and formation. Otherwise, the dynamical relaxation of spin vibrations near Curie temperature gives arising to the extra heat dissipation during the vacancy formation and migration processes, which result in the cusps of temperature dependence of entropies of vacancy migration and formation. Our calculation results are in principle consistent with the theoretic predictions.

Publications arising from the thesis

[1] “Temperature dependence and anisotropy of self- and mono-vacancy diffusion in α-Zr”, Haohua Wen and C. H. Woo, J. Nucl. Mater. **420**, 362 (2012).

[2] “Magnetic effect on vacancy diffusion in BCC iron”, Haohua Wen, Pui-Wai Ma, and C. H. Woo, in P. Gumbsch and E. van der Giessen (Ed.), Conference Proceedings: Radiation Effects, pp. 751-754, MMM2010, the Fifth International Conference on Multiscale Materials Modeling, October 04-08, 2010, Freiburg, Germany.

[3] “Change of thermal and mechanical properties of BCC iron during magnetic transition”, Haohua Wen and C. H. Woo, Conference Session G: Multiscale Modeling of Crystal Plasticity: From Discrete Models to Generalized Continua, MMM2012, the Sixth International Conference on Multiscale Materials Modeling, October 15-19, 2012, Biopolis, Singapore. (Publishing).

Acknowledgements

Firstly, I would like to express my deepest gratitude to my Chief Supervisor, Prof. C. H. Woo, for his patient guidance, many suggestions, scientific ambition, invaluable advice and encouragement. In the past five years, he taught me how to become a qualified scientific researcher, not only in academics, but also people skills. For example, rather than generating the credible data and explaining the results, the crucial aspect of scientific research is finding the significance of the research and the contributions to the human knowledge. As a researcher, the publication of academic paper is one of the approaches to communicate with the scientific community, rather than the aim. The aspiration of finding the unknown physical rules should be the only thing for the researchers to do the scientific research, not matter what difficulties we meet in academics or in reality.

Secondly, I am also profoundly grateful to Prof. Zheng Yue, who introduced me to study with Prof. Woo, and encouraged me when I was frustrated. Thanks should also be given to Dr. Ma Decai, Dr. Ma Pui Wai and Mr. Chui Chun Pon, who presented the experiences and skills in academic research, as well as the valuable discussions. Apparently, it would be far more difficult to finish my thesis without their supports.

Thirdly, I am also indebted to the Hong Kong Polytechnic University (PolyU) and the department of Electronic and Information Engineering (EIE), who give

me the financial support to finish this Ph.D thesis, as well as other official help from the staffs, i.e. Prof. Michael Tse (department head of EIE), and the colleagues in EIE's general office.

Finally, thanks should be given to all my friends for their heartfelt encouragements, especially Mr. Liu Qingyuan and Mr. Tang Lei, who are my best friends and classmates of Wuhan University in Mainland China. Their optimism leads me to tackle difficulties bravely.

Table of Contents

III. METHODOLOGY

IV. PHONON AND MAGNON SPECTRA

V. THERMAL AND MECHANICAL PROPERTIES NEAR MAGNETIC-PHASE TRANSITION

VII. SUMMARY AND CONCLUSION

List of Figures

List of Tables

CHAPTER I

INTRODUCTION

1.1 Magnetic Effects

Magnetic effect plays a pivotal role in almost all physical properties of ferromagnetic materials. For instance, magnetic phase instability of the iron-based steel is considered to be a possible cause to its loss of strength at elevated temperatures, and the consequent collapse of the U. S. World Trade Center in the 9.11 disaster [1]. In another aspect, the body-centred cubic (BCC) crystal structure of iron at zero-Kelvin is induced by magnetic effect. Otherwise, the stable structure of iron could be hexagonal closed packed (HCP) structure instead [2,3,4]. The investigation of magnetic effects has been extended to a much larger interdisciplinary research field studying coupled multi-physical properties, such as thermal, mechanical and electromagnetic. Representative phenomena include thermal-magnetic, magnetomechanics and magnetostriction, and the list goes on.

In non-magnetic materials, anharmonic phenomena such as thermal expansion are induced by phonon-phonon interaction, which depends on the phonon density as a function of temperature. However, the participation of

magnons in ferromagnetic material, such as BCC iron, brings out addition anharmonicity due to scattering of phonons by magnon, thus producing changes in many physical properties related to processes involving the atomic lattice, especially near the FM/PM phase boundary. The interaction between the two elementary excitations is the result of the spin-dependent exchange correlation interaction among the valence electrons of neighboring atoms. The challenge associated with the mechanistic studies of magnetic effects of this kind is the lack of an accurate thermodynamic description of the strongly coupled spin and lattice degrees of freedom in these materials at the high temperatures, especially across the ferro/paramagnetic (FM/PM) phase boundary. Such a thermodynamic picture requires processing of the microscopic dynamical information of the full ensemble of spins and atoms. Solving this problem is the subject of this thesis.

1.2 Overview

Many peculiarities of the physical properties of magnetic materials, such as those mentioned in the foregoing, may be traced to their strong crystalline anharmonicity due to the scattering of phonons by the magnons.

First discovered by Joule [5] in 1842, the typical example of this magnetic effect on anharmonicity is the magnetostrictive effect, namely, the isotropic or anisotropic structural deformation in crystalline solid caused by spontaneous magnetic transition or forced by an external magnetic field. The Invar alloy, i.e.

quenched FCC $Fe_{65}Ni_{35}$, is the famous application of magnetostrictive effect [6,7,8,9], whose thermal expansion coefficient is near zero in a wide range of temperatures. In addition to phase instabilities of iron-based steel, magnetic effects are also suggested to be responsible for the structures of radiation defects in transition metals. For instance, self-interstitial defects in iron adopt the $\langle 110 \rangle$ dumbbell configuration rather than the common $\langle 111 \rangle$ crowdion configuration in other non-magnetic BCC metals [10,11]. Furthermore, the famous "Stage III" controversy, whether it is due to the migration of vacancies or self-interstitials in resistivity recovery experiment of iron [12], have been debated for over thirty years in literatures [13]. Besides, the interpretation for the curved Arrhenius' plot of the self-diffusion experiment [14] in iron is another challenge.

It has been recognized that effects of phonon-magnon interaction are closely related to the free energy required for the corresponding atomic process. Not only the energetic impact is involved, but the entropic impact associated with the heat transferred is also involved. To elucidate the role played by phonon-magnon interaction in these processes, it requires the implementation of the full dynamics of spin and lattice in the coupled system. However, in atomistic simulations, the treatments of the coupled spin and lattice systems are almost always based on the adiabatic approximation that the phonon, electron and magnon reside on different relaxation time scales, so that a simple separation of phonon and magnon excitations can be used in the free-energy calculations.

Antropov *et al.* [15,16] suggested that the interactions between the spin and lattice systems can be modeled by using *ab initio* spin dynamics (SD) based on the local spin density approximation (LSDA) and *ab initio* molecular dynamics (MD). Later on, Stokes *et al.* [17] introduced the non-collinear spin states by using the constrained local moment method to model the spin-lattice dynamics at finite temperature. Körmann *et al.* [18] separated the free energy of the coupled spin and lattice system into vibrational, electronic and magnetic parts based on the adiabatic approximation mentioned above, in which the vibrational and electronic free energies are evaluated under the harmonic approximation, and the magnetic part is calculated by many-body Heisenberg Hamiltonian under mean-field approximation. Similarly, Lavrentiev *et al.* [19] proposed the magnetic cluster expansion (MCE) model for spin dynamics, while the lattice degrees of freedom are carried out by the harmonic treatment.

However, in the fore-going calculations, the self-consistent nature of the relationship between the crystal field that governs the lattice dynamics and the molecular field that controls the spin dynamics has to be carefully taken into account. In particular, at temperatures near FM/PM phase transition, the molecular field tends to vanish, and the characteristic frequencies of the spin waves are shifted down towards those of the lattice waves [20]. When the two dynamics are significantly correlated, the accuracy of the adiabatic approximation may become questionable.

The correlated dynamics of the spin and lattice systems, i.e., with phonon-magnon interaction fully accounted for, is best treated with their different degrees of freedom considered on equal footing in their equations of motion. Ma, Woo and Dudarev (MWD) [21] developed the spin-lattice dynamics (SLD) simulation model for this purpose. By treating the exchange interaction as a function of the interatomic separation, MWD successfully realized a description of the interactive nature of spin and lattice dynamics, from which the SLD simulation scheme is developed [21,22]. SLD provides a useful tool for the study of magnetic effects, particularly where the coupling between the spin and lattice dynamics is strong.

1.3 Objective

In this thesis, we first present the effective Hamiltonian for the ferromagnetic iron, involving the interactive spin and lattice degrees of freedom. The thermodynamics of phonon and magnon, respectively, associated to the lattice and spin vibrations underlying our investigations are reviewed, followed by the origin of the coupling between phonons and magnons. To identity effects on the lattice and the spin subsystem separately, the effective Hamiltonian is resolved into the spin, lattice and spin-lattice interaction components.

Subsequently, we briefly review the statistical thermodynamics and the simulation scheme of SLD, from which phase-space trajectories are obtained for

calculating the corresponding physical properties as functions of temperature. In addition, the thermodynamic integration (TI) method is introduced for the calculations of free energies in the atomic process, linking the thermodynamics with micro-dynamics in this way for understanding changes of physical properties near magnetic transitions.

We then present our results and findings. Firstly, the phonon and magnon spectra are calculated at finite temperatures, with and without the impacts of phonon-magnon interaction. We find for first time effects of anharmonicity, arising from the phonon-magnon interaction at finite temperatures, on the dispersion relations and lifetimes for both elementary excitations in ferromagnetic materials. Secondly, the thermodynamic, magnetic and mechanical properties near FM/PM transition of the ferromagnetic material are investigated to examine the role of phonon-magnon on the thermodynamics and anharmonicity. Finally, we calculate the free energies in the mono-vacancy and self-diffusion processes by using the modified TI method to investigate the contributions from magnons to migration and formation processes of vacancy.

Reference

[1] T. W. Eagar and C. Musso, JOM Journal of the Minerals, Metals and Materials Society **53**, 8-11 (2001).

[2] D. G. Pettifor, *Bonding and Strucutre of Molecules and Solids* (Oxford University Press, Oxford, 1995).

[3] H. C. Herper, E. Hoffmann, and P. Entel, Phys. Rev. B **60**, 3839 (1999).

[4] M. Friák, M. Šob, and V. Vitek, Phys. Rev. B **63**, 052405 (2001).

[5] J. Joule, Sturgeon's Annals of Electricity **8**, 219 (1842).

[6] M. Shiga, in *Materials Science and Technology*, edited by R. W. Cahn, P. Hassen, and E. J. Kramer (VCH, Weinheim, 1993), pp. 159.

[7] M. Dubé, P. R. L. Heron, and D. G. Rancourt, J. Magn. Magn. Mater. **147**, 122 (1995).

[8] M.-Z. Dang, M. Dubé, and D. G. Rancourt, J. Magn. Magn. Mater. **147**, 133 (1995).

[9] M.-Z. Dang, and D. G. Rancourt, Phys. Rev. B **53**, 2291 (1996).

[10] D. Nguyen-Manh, A. Horsfield, and S. L. Dudarev, Phys. Rev. B **73**, 020101 (2006).

[11] P. M. Derlet. D. Nguyen-Manh, and S. L. Dudarev, Phys. Rev. B **76**, 054107 (2007).

[12] S. Takaki, J. Fuss, H. Kugler, U. Dedek, and H. Schultz, Radiat. Eff. **79**, 87 (1983).

[13] H. J. Blythe, H. Kronmuller, A. Seeger, and F. Walz, Phys. Status Solidi A **181**, 233 (2000).

[14] Y. Iijima, and K. Hirano, in *Diffusion Processes in Nuclear Materials*, edited by R. P. Agarwala, (Elsevier Science Publications, B. V., 1992), pp. 169 and the reference therein.

[15] V. P. Antropov, M. I. Katsnelson, M. van Schilfgaarde, and B. N. Harmon, Phys. Rev. Lett. **75**, 729 (1995).

[16] V. P. Antropov, M. I. Katsnelson, B. N. Harmon, M. van Schilfgaarde, and D. Kusnezov, Phys. Rev. B **54**, 1019 (1996).

[17] G. M. Stocks, B. Ujfalussy, X. Wang. D. M. C. Nicholson, W. A. Shelton, Y. Wang, A. Canning, and B. L. Györffy, Philos. Mag. B **78**, 665 (1998).

[18] F. Körmann, A. Dick, B. Grabowski, B. Hallstedt, T. Hickel, and J. Neugebauer, Phys. Rev. B **78**, 033102 (2008).

[19] M. Y. Lavrentiev, D. Nguyen-Manh, and S. L. Dudarev, Phys. Rev. B **81**, 184202 (2010).

[20] K. P. Sinha, and U. N. Upadhyaya, Phys. Rev. **127**, 432 (1962).

[21] P.-W. Ma, C. H. Woo, and S. L. Dudarev, Phys. Rev. B 78, 024434 (2008).

[22] P.-W. Ma, and C. H. Woo, Phys. Rev. E **79**, 046703 (2009).

CHAPTER II

REVIEW OF BASIC THEORY

In this Chapter, we will review the effective Hamiltonian for BCC iron, involving the spin and lattice degrees of freedom. Subsequently, the lattice dynamics is presented to investigate the relevant physical properties arising from the lattice vibration, i.e. phonon. Correspondingly, magnetic excitations are treated classically as correlated spin vibrations, i.e. spin waves or magnons. Finally, the free energy of BCC iron is presented, with the participation of magnons and the mutual interactions between phonons and magnons.

2.1 Effective Hamiltonian of Ferromagnetic Iron

2.1.1 Condensed matter Hamiltonian

In condensed matter, the physical properties can be roughly divided into two categories: those determined by the valence electrons and the rest associated with the vibrations of ion core,[*] i.e. nuclei and core electrons, around their equilibrium positions. The many-body Hamiltonian of condensed matter involving interactive electrons and nuclei is generally written as [1]

$$\begin{aligned}\hat{H} &= -\sum_i \frac{\hbar^2}{2m_e}\nabla_i^2 + \frac{1}{2}\sum_{i\neq j}\frac{e^2}{|\boldsymbol{r}_i-\boldsymbol{r}_j|} - \sum_{I,i}\frac{Z_I e^2}{|\boldsymbol{r}_i-\boldsymbol{R}_I|} \\ &\quad -\sum_I \frac{\hbar^2}{2M_n}\nabla_I^2 + \frac{1}{2}\sum_{I\neq J}\frac{Z_I Z_J e^2}{|\boldsymbol{R}_I-\boldsymbol{R}_J|} \\ &\equiv \hat{T}_e + \hat{V}_{e-e} + \hat{V}_{e-n} + \hat{T}_n + \hat{V}_{n-n}\end{aligned}, \tag{2.1}$$

where the uppercase and lowercase subscripts label the nuclei and electrons, respectively; $\hbar$ is the reduced Plank's constant; M_n and m_e are the respective nuclear and electronic mass; $\boldsymbol{R}_I$[†] is the nuclear position and Z_I is the atomic number of ion I; $\boldsymbol{r}_i$ is the electronic position, in which the electronic spin operator is involved. In Eq. (2.1), the canonical kinetic and potential energy operator for nuclei and electrons can be defined as:

$$\hat{T}_e \equiv -\sum_i \frac{\hbar^2}{2m_e}\nabla_i^2, \tag{2.2a}$$

[*] The meaning of *ion core* or *nuclear* is equivalent to *lattice* in this Chapter.
[†] Here and in the rest of this thesis, bold-face variables denote vectors.

$$\hat{V}_{e-e} \equiv \frac{1}{2}\sum_{i\neq j}\frac{e^2}{\left|\boldsymbol{r}_i-\boldsymbol{r}_j\right|}, \tag{2.2b}$$

$$\hat{V}_{e-n} \equiv -\sum_{I,i}\frac{Z_I e^2}{\left|\boldsymbol{r}_i-\boldsymbol{R}_I\right|}, \tag{2.2c}$$

$$\hat{T}_n \equiv -\sum_{I}\frac{\hbar^2}{2M_n}\nabla_I^2, \tag{2.2d}$$

$$\hat{V}_{n-n} \equiv \frac{1}{2}\sum_{I\neq J}\frac{Z_I Z_J e^2}{\left|\boldsymbol{R}_I-\boldsymbol{R}_J\right|}, \tag{2.2e}$$

where $\hat{T}_e$ and $\hat{T}_n$ are the electronic and nuclear kinetic energy, respectively; $\hat{V}_{e-e}$ is the electron-electron interaction, involving the spin-spin exchange interaction arising from partial filled electrons, e.g., 3*d*-electrons in BCC iron; $\hat{V}_{e-n}$ is the Coulombic attraction between electrons and nuclei; $\hat{V}_{n-n}$ is the Coulombic repulsion energy of the nuclei. The Hamiltonian in Eq. (2.1) operates on the many-body wave-function in position representation $\psi\left(\left\{\boldsymbol{R}_I,\boldsymbol{r}_i\right\}\right)$, i.e. the so-called Schrödinger equation in the form:

$$\hat{H}\psi\left(\left\{\boldsymbol{R}_I,\boldsymbol{r}_i\right\}\right) = E_{tot}\psi\left(\left\{\boldsymbol{R}_I,\boldsymbol{r}_i\right\}\right), \tag{2.3}$$

where E_{tot} is the total energy of the nuclei and electrons, being the eigenvalue corresponding to ψ, which should be antisymmetric under the exchange of electrons due to the requirement of Pauli's exclusion principle. By solving Eq. (2.3), all the information of the condensed matter can be derived from the spectroscopy of E_{tot}. However, direct solution of Eq. (2.3) is difficult, thus

approximations have to be called for to reduce it as manageable.

2.1.2 Born-Oppenheimer approximation

We may rewrite the Hamiltonian in Eq. (2.1) in the form,

$$\hat{H} = \hat{T}_n + \hat{H}_0 , \tag{2.4}$$

where $\hat{H}_0$ containing the electronic kinetic energy and the total Coulombic energy of electrons and nuclei, as

$$\hat{H}_0 = \hat{T}_e + \hat{V}_{e-e} + \hat{V}_{e-n} + \hat{V}_{n-n} . \tag{2.5}$$

We recognize that $\hat{H}_0$ does not involve the momentum operator of nuclei, so that it can be treated as the electronic Hamiltonian at a fixed nuclei configuration, $\{\boldsymbol{R}_I\}$. Since the kinetic energy of nuclear $\hat{T}_n$ is very small due to its larger mass, it can be treated as a perturbation of $\hat{H}_0$ in Eq. (2.1) and the total energy E_{tot} can be obtained by using the perturbation theory [2].

If we only consider the zero-order approximation, the Hamiltonian $\hat{H}$ is reduced as $\hat{H}_0$. As shown in Eq. (2.4), $\hat{H}_0$ only involves the static positions of the nuclear. For determining the electronic motions in Eq. (2.4), $\hat{V}_{n-n}$ is treated as constant and the configuration of nuclear $\{\boldsymbol{R}_I\}$ is effectively treated as a set of external parameters. $\hat{V}_{e-n}$ is usually regarded as an external potential, $\hat{V}_{\text{ext}}$, imposed on the electrons for a fixed nuclear configuration, so that the electronic

Hamiltonian is usually written as

$$\hat{H}_{el} = \hat{T}_e + \hat{V}_{e-e} + \hat{V}_{\text{ext}} . \tag{2.6}$$

Physically, due to the high mass, the nuclei move much slower than the electrons. If nuclei move away from their equilibrium positions, then the electrons can instantaneously adjust their positions at any given time, but with higher total energy. However, the electron system remains in a ground state corresponding to the nuclei configuration. If the nuclei return to their initial positions, then the energy expended is fully restored without any excitation of the electron system. In this regard, the total energy E_{tot} as a function of nuclei configuration plays the role of a potential for the atomic motion, in the form:

$$E_{tot} = \sum_I \frac{\boldsymbol{P}_I^2}{2M_I} + \frac{1}{2}\sum_{I\neq J} \frac{Z_I Z_J e^2}{\left|\boldsymbol{R}_I - \boldsymbol{R}_J\right|} + E_{el}\left(\{\boldsymbol{R}_I\}\right), \tag{2.7}$$

where the first and second terms are the nuclei kinetic and potential energy, respectively; $E_{el}\left(\{\boldsymbol{R}_I\}\right)$ is the electronic total energy determined by $\hat{H}_{el}$, which depends on the nuclei configuration in a parametric way. This is the Born-Oppenheimer, or adiabatic, approximation [3].

Under this approximation, when we consider the motions of electrons, the motions of nuclei can be ignored. On the other hand, when we consider the motions of nuclei, the electrons is regarded as a distribution, i.e. electron cloud, in which the nuclei are immersed, inducing the effective interactions between

nuclei through the electron cloud. Such effective interactions depend on the electron configurations. Separating the motions of electrons and nuclei, the Born-Oppenheimer approximation necessarily neglects the electron-phonon interactions, which, however, is out of the scope of this thesis.

2.1.3 Exchange integral of electrons

We focus on the electronic total energy in this subsection. We rewrite the electronic Hamiltonian in Eq. (2.5) as

$$\begin{aligned}\hat{H}_{el} &= \hat{T}_e + \hat{V}_{ext} + \hat{V}_{e-e} \\ &= \sum_i \left(-\frac{\hbar^2}{2}\nabla_i^2 + \hat{v}_i \right) + \hat{V}_{e-e}, \\ &\equiv \sum_i \hat{h}_i + \hat{V}_{e-e}\end{aligned} \tag{2.8}$$

where $\hat{h}_i \equiv \hat{T}_e + \hat{V}_{\text{ext}} = -\frac{\hbar^2}{2}\nabla_i^2 + \hat{v}_i$ only depends on the electronic coordinate of $\boldsymbol{r}_i$, with $\hat{v}_i$ being the potential energy of the ith electron provided by nuclei. Otherwise, $\hat{V}_{e-e}$ depends on pairs of electrons, which cannot separate variables in the Schrödinger equation. However, we could assume that the electron does not interact with other electrons one by one, but with the averaged density of electrons based on mean-field theory, which is so-called Hartree Approximation, so that

$$\hat{V}_{e-e} \approx \sum_i \hat{g}_i(\boldsymbol{r}_i), \tag{2.9}$$

where $\hat{g}_i(\boldsymbol{r}_i)$ is the density operator of the ith electron provided by other electrons.

In this regard, the electronic Hamiltonian can be totally expressed as the sum of single-electronic Hamiltonian, i.e.

$$\hat{H}_{el} \approx \sum_i \left(-\frac{\hbar^2}{2}\nabla_i^2 + \hat{v}_i + \hat{g}_i \right) \equiv \sum_i \hat{H}_i , \tag{2.10}$$

and then the many-electron Schrödinger equation can be solved as N independent one electron equations:

$$\hat{H}_i \phi(\boldsymbol{r}_i) = \varepsilon_i \phi(\boldsymbol{r}_i) \tag{2.11}$$

where $\phi(\boldsymbol{r}_i)$ is the electronic wave-function involving the spin-polarization with the energy ε_i. And the total electronic wave-function involving N electrons is thus written as

$$\psi_{el}(\{\boldsymbol{r}_i\}) = \prod_i \phi(\boldsymbol{r}_i) \tag{2.12}$$

In this regard, the total electronic energy under Hartree approximation is given by,

$$\begin{aligned} E_{el} &\approx \left\langle \hat{H}_{el} \right\rangle_{\text{Hartree}} = \left\langle \psi_{el}(\{\boldsymbol{r}_i\}) \right| \left(\sum_i \hat{h}_i + \hat{V}_{e-e} \right) \left| \psi_{el}(\{\boldsymbol{r}_i\}) \right\rangle \\ &= \sum_i \left\langle \phi_i(\boldsymbol{r}) \right| \hat{h}_i \left| \phi_i(\boldsymbol{r}) \right\rangle \\ &\quad + \frac{1}{2} \sum_{i \neq j} \left\langle \phi_i(\boldsymbol{r}) \phi_j(\boldsymbol{r}') \right| \frac{1}{|\boldsymbol{r} - \boldsymbol{r}'|} \left| \phi_i(\boldsymbol{r}) \phi_j(\boldsymbol{r}') \right\rangle \end{aligned} \tag{2.13}$$

where the second term is called Coulomb integral, or Coulomb energy, i.e.

$$\begin{aligned} C_{ij} &= \left\langle \phi_i(\boldsymbol{r})\phi_j(\boldsymbol{r}') \left| \frac{1}{|\boldsymbol{r}-\boldsymbol{r}'|} \right| \phi_i(\boldsymbol{r})\phi_j(\boldsymbol{r}') \right\rangle \\ &= \int\int \phi_i^*(\boldsymbol{r}_1)\phi_j^*(\boldsymbol{r}_2)\frac{1}{|\boldsymbol{r}_1-\boldsymbol{r}_2|}\phi_i(\boldsymbol{r}_1)\phi_j(\boldsymbol{r}_2)\mathrm{d}\boldsymbol{r}_1\mathrm{d}\boldsymbol{r}_2 \end{aligned} . \tag{2.14}$$

However, we recognize that electrons are fermions. Due to the Pauli's exclusion principle, no two particles can be described by the same one particle function. The total wave-function ψ_{el} for the electron system must be an antisymmetric sum of all the products which can be obtained by interchanging electron labels. Therefore, rather than the form in Eq. (2.12), ψ_{el} can be represented as a determinant, namely Slater determinant, as

$$\psi_{el}(\boldsymbol{r}_1,\boldsymbol{r}_2,\cdots,\boldsymbol{r}_N) = \frac{1}{\sqrt{N!}} \begin{vmatrix} \phi_1(\boldsymbol{r}_1) & \phi_2(\boldsymbol{r}_1) & \cdots & \phi_N(\boldsymbol{r}_1) \\ \phi_1(\boldsymbol{r}_2) & \phi_2(\boldsymbol{r}_2) & \cdots & \phi_N(\boldsymbol{r}_2) \\ \vdots & \vdots & \ddots & \vdots \\ \phi_1(\boldsymbol{r}_N) & \phi_2(\boldsymbol{r}_N) & \cdots & \phi_N(\boldsymbol{r}_N) \end{vmatrix}. \tag{2.15}$$

Substitute Eq. (2.15) into the total energy equation (Eq. (2.13)), we have the so-called Hartree-Fock electronic energy in the form as

$$\begin{aligned} E_{el} &\approx \left\langle \hat{H}_{el} \right\rangle_{HF} = \left\langle \psi_{el} \left| \hat{H}_{el} \right| \psi_{el} \right\rangle \\ &= \sum_{i=1}^{N} \varepsilon_i + \frac{1}{2}\sum_{i=1}^{N}\sum_{j=1}^{N}\left(C_{ij} - J_{ij}\right) \end{aligned} \tag{2.16}$$

where

$$\varepsilon_i = \int \phi_i^*(\boldsymbol{r}) \left(-\frac{\hbar^2}{2}\nabla_i^2 + \hat{v}_i \right) \phi_i(\boldsymbol{r})\mathrm{d}\boldsymbol{r} \tag{2.17}$$

and C_{ij} is the Coulomb integral defined above, and J_{ij} is the exchange integral, i.e.

$$J_{ij} = \int\int \phi_i^*(\boldsymbol{r}_1)\phi_j^*(\boldsymbol{r}_2)\frac{1}{|\boldsymbol{r}_1 - \boldsymbol{r}_2|}\phi_i(\boldsymbol{r}_2)\phi_j(\boldsymbol{r}_1)\mathrm{d}\boldsymbol{r}_1\mathrm{d}\boldsymbol{r}_2 . \tag{2.18}$$

Notice that J_{ij} is similar in form to C_{ij}, but with the one-electron wave functions ϕ_i and ϕ_j exchanged. Also, electrons i and j have to be of the same spin-polarization for J_{ij} to be non-zero due to the orthogonality of their spin parts. In addition, C_{ij} is the purely electrostatic interaction of two charge densities for electrons i and j, whereas J_{ij} has no classical analogue and is a direct result of the determinantal form of antisymmetric ψ_{el} which sums all possible products of permutations of electrons among orbitals.

If we substitute Eq. (2.16) into Eq. (2.6), the total energy of nuclei and electrons in the non-magnetic materials is thus written as

$$\begin{aligned} E_{tot} &= \sum_I \frac{\boldsymbol{P}_I^2}{2M_I} + \frac{1}{2}\sum_{I\neq J}\frac{Z_I Z_J e^2}{|\boldsymbol{R}_I - \boldsymbol{R}_J|} + \sum_{i=1}^{N} H_i + \frac{1}{2}\sum_{i=1}^{N}\sum_{j=1}^{N}\left(C_{ij} - J_{ij}\right) \\ &= \sum_I \frac{\boldsymbol{P}_I^2}{2M_I} + U\left(\{\boldsymbol{R}_I\}\right) \end{aligned} \tag{2.19}$$

where $U\left(\{\boldsymbol{R}_I\}\right)$ is the potential of nuclei, involving the electronic properties. Eq. (2.19) shows the atomic nuclei motions are associated with the properties of the electron system. Therefore, the details of the electronic properties are firstly calculated in atomistic simulation, to derive the potential for the atomic nuclei

motions. Properties of the solid associated with the atomic motion can then be deduced. For instance, the developed interatomic potential for metals based on embedded atomic method (EAM) contains the electronic density as a function of atomic nuclei coordinates. Although the exact mathematical formulation of this potential is complicated, to obtain the physical properties associated with the thermal excitations in solids, it just requires a general formalism which enables equations of motion to be formulated and solved for an arbitrary potential.

2.1.4 Heisenberg exchange Hamiltonian

As discussed in the foregoing, the total wave function ψ_{el} of electron system has to be antisymmetrical according to the Pauli's exclusion principle, i.e. the determinant form in Eq. (2.15), which, however, is only applicable to the case of parallel spin. In addition, the symmetry properties of ψ_{el} are profoundly modified by inclusion of the spin. We note that, the electronic wave function φ_i can be expressed as the product of the orbital component ϕ_i and spin component χ_i while neglecting the 'magnetic' coupling between the spin and orbital, i.e. $\varphi_i = \phi_i \chi_i$, where χ_i has only two characteristic values, i.e. $+\frac{1}{2}$ for spin-up and $-\frac{1}{2}$ for spin-down. Take two-electron system for an example. If the electronic spins are parallel, i.e. both are spin-up or spin-down, the orbital wave function must be antisymmetrical, taking the form as Eq. (2.15),

$$\begin{aligned}\phi_{\text{ant}} &= \frac{1}{\sqrt{2!}}\begin{vmatrix}\phi_1(\boldsymbol{r}_1) & \phi_1(\boldsymbol{r}_2)\\ \phi_2(\boldsymbol{r}_1) & \phi_2(\boldsymbol{r}_2)\end{vmatrix}\\ &= \frac{1}{\sqrt{2}}\left\{\phi_1(\boldsymbol{r}_1)\phi_2(\boldsymbol{r}_2)-\phi_1(\boldsymbol{r}_2)\phi_2(\boldsymbol{r}_1)\right\}\end{aligned}. \tag{2.20a}$$

Otherwise, if the spins are antiparallel, i.e. one is spin-up and the other is spin-down, the orbital wave-function must be symmetrical, as

$$\phi_{\text{sym}} = \frac{1}{\sqrt{2}}\left\{\phi_1(\boldsymbol{r}_1)\phi_2(\boldsymbol{r}_2)+\phi_1(\boldsymbol{r}_2)\phi_2(\boldsymbol{r}_1)\right\}. \tag{2.20b}$$

Substitute Eqs. (2.20) into the Schrödinger equation as expressed in Eq. (2.16), the electronic energy of the system involving two interactive spins is given by

$$E_{12} = \varepsilon_1 + \varepsilon_2 + \frac{1}{2}\left(C_{12} \mp J_{12}\right), \tag{2.21}$$

where ε_1 and ε_2 are given as the expression in Eq. (2.17), which are independent of the symmetry; and the remaining term, $E_{\text{int}} = C_{12} \mp J_{12}$ is the characteristic value of the electron-electron interaction, $\hat{V}_{e-e}$. $E_{\text{int}} = C_{12} - J_{12}$ while two electronic spins are parallel, namely the triplet state, otherwise, $E_{\text{int}} = C_{12} + J_{12}$ while two electronic spins are anti-parallel, namely the singlet state.

Let $\hat{\boldsymbol{S}}_1$ and $\hat{\boldsymbol{S}}_2$ be the electronic spin operators, we can obtain the Hamiltonian of exchange interaction between two electrons. According to rule of quantum mechanics,

$$-\frac{1}{2}\left(1+4\hat{\boldsymbol{S}}_1\cdot\hat{\boldsymbol{S}}_2\right)=-\frac{1}{2}-\left(\hat{\boldsymbol{S}}^2-\hat{\boldsymbol{S}}_1^2-\hat{\boldsymbol{S}}_2^2\right)=\mp 1 \tag{2.22a}$$

where $\hat{\boldsymbol{S}}=\hat{\boldsymbol{S}}_1+\hat{\boldsymbol{S}}_2$ is the total spin operator; -1 and $+1$ correspond to the eigenvalue of $\hat{\boldsymbol{S}}$: $S=1$ and $S=0$, respectively. Here, we have used the identities to derive Eq. (2.21),

$$\hat{\boldsymbol{S}}^2=S\left(S+1\right), \tag{2.22b}$$

$$\hat{\boldsymbol{S}}_1^2=\hat{\boldsymbol{S}}_2^2=\frac{1}{2}\left(\frac{1}{2}+1\right)=\frac{3}{4}. \tag{2.22c}$$

In this regard, the Hamiltonian of two electron system having the characteristic value of E_{12} in Eq. (2.21) can be given as

$$\hat{H}_{12}=\hat{h}_1+\hat{h}_2+\hat{C}_{12}-\frac{1}{2}\hat{J}_{12}-2\hat{J}_{12}\hat{\boldsymbol{S}}_1\cdot\hat{\boldsymbol{S}}_2 \tag{2.23}$$

where $\hat{h}_1$ and $\hat{h}_2$ are the Hamiltonian of non-interactive electrons given by Eq. (2.8); $\hat{C}_{12}$ is the operator of Coulombic interaction, having the characteristic value of C_{12} as Eq. (2.14); $\hat{J}_{12}$ is the operator of exchange integral, having the characteristic value of J_{12} as Eq. (2.18). The final term in Eq. (2.23),

$$\hat{H}_{ex}=-2\hat{J}_{12}\hat{\boldsymbol{S}}_1\cdot\hat{\boldsymbol{S}}_2, \tag{2.24}$$

is so-called the Heisenberg exchange Hamiltonian, first proposed by Heisenberg [4]. More rigorous deduction from the many-electron Hamiltonian by quantum mechanics is given by Dirac [5]. Subsequently, Anderson [6] proved that

Heisenberg model can be also available in the cases of $S > 1/2$. It should be noted that $\hat{H}_{ex}$ has an electrostatic origin, with a quantum mechanical nature arising from the exchange interaction term of electron-electron Coulombic potential. It should be distinguished from the direct magnetic dipole-dipole interaction between electronic magnetic moments, although such an angle dependent interaction can be found as one term of the mutual potential energy of two dipoles, $\boldsymbol{\mu}_1$ and $\boldsymbol{\mu}_2$, i.e.

$$E = \frac{\boldsymbol{\mu}_1 \cdot \boldsymbol{\mu}_2}{r^3} - \frac{3(\boldsymbol{\mu}_1 \cdot \boldsymbol{r}_1)(\boldsymbol{\mu}_2 \cdot \boldsymbol{r}_2)}{r^5}. \tag{2.25}$$

However, the strength of $\hat{H}_{ex}$ depends on the exchange integral J_{ij}, the overlapping of two electronic wave functions, which is much stronger than that of Eq. (2.25).

2.1.5 Effective Hamiltonian of ferromagnetic iron

Eq. (2.24) shows the explicit exchange interaction between two electronic spins. Nevertheless, it can be generalized to the entire solid consisting of the so-called magnetic atoms having non-zero spins, such as in transition metals.

For a transition metal, the spin-polarized electronic structure comes from the *d*-electrons in the partially filled *d*-shell [7]. According to Hund's rule, the stable electronic configuration of an isolated atom is adopted to be the one with a maximum magnetic moment (MM) [8]. For instance, there are 6 *d*-electrons in an

isolated iron in 5 *d*-electronic orbitals, involving 10 spin-polarized electronic states. The Hund's rule and Pauli's exclusion principle allow the net MM of an isolated iron atom to be $4\mu_{\mathrm{B}}$ (μ_{B} is the Bohr magneton[‡]), which there are 5 electrons at spin-up states and the remaining one at spin-down state. Yet, due to the hopping of the electrons of the neighboring atoms and hybridization between 3*d* and 4*s* electrons, the MM per atom in the crystalline iron with BCC structure is reduced to $2.2\mu_{\mathrm{B}}$ at the ground state [9]. In this regard, the individual iron atom has non-zero total spins and an associated MM, causing the magnetization observed macroscopically [10].

The exchange interaction between the spins of neighboring atoms in BCC iron is thus described commonly by the Heisenberg Hamiltonian in the form [11],[12]:

$$H_S = -\frac{1}{2}\sum_{I\neq J} J_{IJ}\left(\{\boldsymbol{R}_I\}\right)\boldsymbol{S}_I\cdot\boldsymbol{S}_J \tag{2.26}$$

where $\boldsymbol{S}_I$ is the spin vector of atom I, and $J_{IJ}\equiv J\left(\left|\boldsymbol{R}_I-\boldsymbol{R}_J\right|\right)$ is the exchange integral between atoms I and J determined by the overlapping the electronic wave-functions, depending on the ionic configuration $\{\boldsymbol{R}_{IJ}\}$. The MM of atom I has a magnitude $M_I=g\mu_B S_I$ where $g=2.0023$ is the electronic *g*-factor, and $S_I\left(\approx 1.1\mu_{\mathrm{B}}\right)$ is the magnitude of its spin, whose direction is

[‡]Bohr magneton is a consequent physical constant in Niels Bohr's atom model, representing for the magnitude of an electron's spin magnetic moment.

opposite to the MM by convention. As interpreted by Dirac [5], the vector model in Eq. (2.26), which is formally equivalent to the quantum mechanical exchange effect in Eq. (2.24), enables us to picture and also to follow quantitatively the effects of the exchange interaction, for instance the classical treatment of spin waves, discussed in the following section. The detail of this issue can be seen in the short description given in Ref. [13].

Depending on the sign of the exchange integral J_{IJ}, two types of magnetic interactions can be described by the Heisenberg Hamiltonian in Eq. (2.26). With a positive J_{IJ}, neighboring atomic spins experience forces aligning the spins and stabilizes the ferromagnetic phase, such as BCC iron. In contrast, with a negative J_{IJ}, anti-parallel atomic spins are encouraged, giving rise to an antiferromagnetic ground state, which frequently occurs among transition metal compounds or oxides, for instance, iron manganese alloy (FeMn) and nickel oxide (NiO).

Consequently, the effective Hamiltonian in ferromagnetic iron, which is treated as an ensemble of Heisenberg particles involving the motions of atomic lattices and spins, is thus written as

$$H_H = \sum_i \frac{\boldsymbol{p}^2}{2m_i} + U\left(\{\boldsymbol{R}_i\}\right) - \frac{1}{2}\sum_{i\neq j} J_{ij}\left(\{\boldsymbol{R}_i\}\right)\boldsymbol{S}_i \cdot \boldsymbol{S}_j \,. \tag{2.27}$$

Here and in the rest of this thesis, lowercase denotes the atomic index unless

otherwise stated. We note that Eq. (2.27) is derived based on the Born-Oppenheimer approximation, in which the electronic configuration is adiabatically subsumed into the effective potential $U\left(\{\boldsymbol{R}_I\}\right)$. The spin and lattice are coupled through the exchange integral $J_{ij}\left(\{\boldsymbol{R}_i\}\right)$, which depends on the lattice configuration $\{\boldsymbol{R}_i\}$. In this picture, Eq. (2.19) may be treated as the lattice Hamiltonian,

$$H_L\left(\boldsymbol{R}\right)=\sum_i \frac{\boldsymbol{p}_i^2}{2m_i}+U\left(\boldsymbol{R}\right), \tag{2.28}$$

and the Hamiltonian describing the spin-spin interaction as in Eq. (2.26) can be expressed as

$$H_S\left(\boldsymbol{S}\right)=-\frac{1}{2}\sum_{i\neq j} J_{ij}\left(\boldsymbol{R}\right)\boldsymbol{S}_i\cdot\boldsymbol{S}_j, \tag{2.29}$$

where $\boldsymbol{R}\equiv\{\boldsymbol{R}_i\}$ and $\boldsymbol{S}\equiv\{\boldsymbol{S}_i\}$ stand for the lattice and spin configuration, respectively. $\boldsymbol{R}$ is usually regarded as parameter in the spin Hamiltonian H_S. In the following sections, we will review the thermodynamics related to the lattice and spin dynamics starting from these two Hamiltonians.

2.2 Lattice Dynamics

We review in this section some fundamental aspects of lattice dynamics and the relevant physical properties due to the related thermal excitation, i.e. phonon. More details on this subject can be found in Ref. [14,15,16,17,18].

2.2.1 Harmonic approximation of the crystal potential

In this subsection, we will discuss the lattice vibration under the harmonic approximation, which the ion-core vibration around its equilibrium position is very small.

We consider a crystal containing the infinite number of parallelepipedic unit cells defined by three non-coplanar vectors $\boldsymbol{a}_1$, $\boldsymbol{a}_2$ and $\boldsymbol{a}_3$, where there is only one atom in the unit cell. If we denote $\boldsymbol{R}_l^0$ and $\boldsymbol{u}_l$ as the atomic equilibrium position and its displacement, respectively, in the l th unit cell, where $l=(l_1,l_2,l_3)$, the instantaneous position $\boldsymbol{R}_l(t)$ of atom at time t is given by

$$\boldsymbol{R}_l(t)=\boldsymbol{R}_l^0+\boldsymbol{u}_l(t),\quad \boldsymbol{x}_l=\sum_{i=1}^{3} l_i\boldsymbol{a}_i\ . \tag{2.30}$$

In this regard, the kinetic energy of lattice vibrations is written as

$$T=\frac{1}{2}\sum_{l,\alpha} m\dot{u}_l^{\alpha}\dot{u}_l^{\alpha} \qquad (\alpha=x,y,z) \tag{2.31}$$

where u_l^{α} is the α component of $\boldsymbol{u}_l$ in Cartesian coordinate system.

Since the atomic displacements are very small in the harmonic region of the potential, the total potential U governing the lattice motions (See in Eq. (2.28)) is then expanded in a Taylor series of the atomic displacements up to the second order only, by neglecting terms of third and higher order, i.e.

$$U = U_0 + \sum_{l,\alpha} U_{\alpha}^{(1)}(l) u_l^{\alpha} + \frac{1}{2} \sum_{l,\alpha} \sum_{l',\beta} U_{\alpha\beta}^{(2)}(l,l') u_l^{\alpha} u_{l'}^{\beta} . \tag{2.32}$$

Here, U_0 is a constant, representing the ground-state potential energy of the crystal with all the atoms staying in their equilibrium positions, which is not related to the lattice vibrations due to the thermal fluctuations. The first derivative of the potential in Eq. (2.32),

$$U_{\alpha}^{(1)}(l) = \left(\frac{\partial U}{\partial u_l^{\alpha}} \right)_0 = 0, \tag{2.33}$$

because the total force on any atoms must be zero in the equilibrium configuration labeled by the subscript zero. Here the variable l in $U_{\alpha}^{(1)}(l)$ is the abbreviation of $\boldsymbol{R}_l$. The second derivative,

$$U_{\alpha\beta}^{(2)}(l,l') = \left(\frac{\partial^2 U}{\partial u_l^{\alpha} \partial u_{l'}^{\beta}} \right)_0 \qquad (\alpha, \beta = x, y, z), \tag{2.34}$$

is the force constant tensor. The lattice Hamiltonian in Eq. (2.28) is then given by

$$H_L = T + U = \frac{1}{2m} \sum_{l,\alpha} p_l^{\alpha} p_l^{\alpha} + U_0 + \frac{1}{2} \sum_{l,\alpha} \sum_{l',\beta} U_{\alpha\beta}^{(2)}(l,l') u_l^{\alpha} u_{l'}^{\beta} , \tag{2.35}$$

where $p_l^{\alpha} = m\dot{u}_l^{\alpha}$ is the conjugate mechanical quantity of u_l^{α}. From Eq. (2.35), the equation of motion can be derived in the form,

$$m\ddot{u}_l^{\alpha} = -\sum_{l',\beta} U_{\alpha\beta}^{(2)}(l,l') u_{l'}^{\beta} , \tag{2.36}$$

which are the linear coupled vibration equations involving $3N$ degrees of freedom, N being the number of atoms in the crystal.

Under the periodic boundary condition, the crystal has translational symmetry, and the solution of Eq. (2.36) should have the form of plane waves, according to Bloch's law, as

$$u_l^\alpha(\boldsymbol{q}) = \frac{1}{2\sqrt{Nm}}\left\{A(\boldsymbol{q})\boldsymbol{e}_\alpha(\boldsymbol{q})e^{\mathrm{i}\left(\boldsymbol{q}\cdot\boldsymbol{R}_l^0-\omega_{\boldsymbol{q}}t\right)}+\text{c.c.}\right\}, \tag{2.37}$$

where $\boldsymbol{q}$ is the wave-vector, and $\omega_{\boldsymbol{q}}$ and $\boldsymbol{e}_\alpha$ are corresponding angular frequency and polarization vector, respectively; $A(\boldsymbol{q})$ is the amplitude, and c.c. denotes the complex-conjugate. Substituting Eq. (2.37) into the space Fourier transform of the right-hand side of Eq. (2.36) leads to the *dynamical matrix* $D_{\alpha\beta}(\boldsymbol{q})$,

$$D_{\alpha\beta}(\boldsymbol{q}) \equiv \frac{1}{m}\sum_{l'} U_{\alpha\beta}^{(2)}(0,l')e^{\mathrm{i}\boldsymbol{q}\cdot\left(\boldsymbol{R}_0^0-\boldsymbol{R}_{l'}^0\right)}, \tag{2.38}$$

which is the Fourier transform of the interatomic force constant tensor. Here we set $l=0$ since the summation is over all values of l' and the crystal is infinite, periodic, and the origin cell is arbitrary. In this way, Eq. (2.36) is translated into an eigenvalue problem,

$$\sum_\beta D_{\alpha\beta}(\boldsymbol{q})e_\beta(\boldsymbol{q}) = \omega_{\boldsymbol{q}}^2 e_\alpha(\boldsymbol{q}). \tag{2.39}$$

Since $D_{\alpha\beta}(\boldsymbol{q})$ is Hermitian, the characteristic frequencies of vibration modes $\omega_{\boldsymbol{q}}$ are real.

2.2.2 Normal modes and phonons

We can introduce normal modes $Q(\boldsymbol{q})$ by rewriting the displacements as

$$\boldsymbol{u}_l(\boldsymbol{q}) = \frac{1}{\sqrt{Nm}} \sum_{\boldsymbol{q}} Q(\boldsymbol{q}) e(\boldsymbol{q}) e^{\mathrm{i}\boldsymbol{q}\cdot\boldsymbol{R}_l} \tag{2.40}$$

with

$$Q(\boldsymbol{q}) = \frac{1}{2}\left\{ A(\boldsymbol{q}) e^{-\mathrm{i}\omega_q t} + A^*(-\boldsymbol{q}) e^{\mathrm{i}\omega_q t} \right\} \tag{2.41}$$

The Hamiltonian of lattice vibration H_{vib} can be written as

$$H_{\mathrm{vib}} = H_L - U_0 = \frac{1}{2} \sum_{\boldsymbol{q}} \left\{ P^*(\boldsymbol{q}) P(\boldsymbol{q}) + \omega_q^2 Q^*(\boldsymbol{q}) Q(\boldsymbol{q}) \right\} \tag{2.42}$$

where $P(\boldsymbol{q})$ is the conjugate normal momentum, i.e. $P(\boldsymbol{q}) \equiv \dot{Q}(\boldsymbol{q})$. The equation of motion as Eq. (2.36) is reduced as the one for uncoupled harmonic oscillator, i.e.

$$\ddot{Q}(\boldsymbol{q}) + \omega_q^2 Q(\boldsymbol{q}) = 0 . \tag{2.43}$$

According to quantum mechanics, $P(\boldsymbol{q})$ and $Q(\boldsymbol{q})$ can be regarded as the canonical momentum and position operators, respectively. However, we can simplify the lattice Hamiltonian by introducing the annihilation and creation

operators $\hat{b}_q$ and $\hat{b}_q^+$, i.e.

$$\hat{b}_q = \sqrt{\frac{\omega(\boldsymbol{q})}{2\hbar}}\left\{Q(\boldsymbol{q}) - \frac{P^*(\boldsymbol{q})}{\mathrm{i}\omega(\boldsymbol{q})}\right\}, \tag{2.44a}$$

$$\hat{b}_q^+ = \sqrt{\frac{\omega(\boldsymbol{q})}{2\hbar}}\left\{Q(\boldsymbol{q}) + \frac{P^*(\boldsymbol{q})}{\mathrm{i}\omega(\boldsymbol{q})}\right\}. \tag{2.44b}$$

In the occupation number representation, the annihilate or create a quantum of excitation for the mode $s = \boldsymbol{q}$,

$$\hat{b}_s \left|\cdots, n_s, \cdots\right\rangle = \sqrt{n_s}\left|\cdots, n_s - 1, \cdots\right\rangle, \tag{2.45a}$$

$$\hat{b}_s^+ \left|\cdots, n_s, \cdots\right\rangle = \sqrt{n_s + 1}\left|\cdots, n_s + 1, \cdots\right\rangle. \tag{2.45b}$$

In this regard, the vibrational Hamiltonian is rewritten as the form of a sum of uncoupled quantum harmonic oscillators, i.e.

$$H_{\mathrm{vib}} = \sum_s \hbar\omega_s \left\{\hat{b}_s^+ \hat{b}_s + \frac{1}{2}\right\} \equiv \sum_s \hbar\omega_s \left(\hat{n}_s + \frac{1}{2}\right), \tag{2.46}$$

where $\hat{n}_s \equiv \hat{b}_s^+ \hat{b}_s$ is the number operator, and

$$\hat{n}_s \left|\cdots, n_s, \cdots\right\rangle = n_s \left|\cdots, n_s - 1, \cdots\right\rangle. \tag{2.47}$$

Within the above description, we have introduced the concept of a phonon as a quantized excitation of lattice vibration mode $s = \boldsymbol{q}$, which is a quasi-particle obeying Bose-Einstein statistics at finite temperature T, i.e.

$$\left\langle \hat{n}_s \right\rangle_T = \left(e^{\hbar\omega_s / k_B T} - 1 \right)^{-1}. \tag{2.48}$$

In addition, we can see in Eq. (2.46), even when the phonons are all in their ground state at $T = 0\mathrm{K}$, the vibrational system still possesses $\frac{1}{2}\hbar\omega$ of energy per mode, corresponding to zero-point motion, which is attributed solely to the quantum mechanical nature of lattice vibrations.

2.2.3 Thermodynamics of harmonic phonon system

In order to connect the vibrational properties with the thermodynamics of crystals, we will recall the relations for thermodynamics properties of phonons, but without deriving them, in this subsection. One can find more detail of the standard results in many textbook, e.g. Ref. [19,20,21].

In the foregoing, we present that the small lattice vibrations around their equilibrium positions due to the thermal fluctuation in the crystal involving N atoms can be described by $3N$ normal vibration modes, i.e. Eq. (2.40). Such a vibrational system is equivalent to the set of independent quantum harmonic oscillators with specific vibration frequencies ω_s, i.e. Eq. (2.47). The total vibrational energy E_{vib} is derived from the standard Schrödinger equation,

$$H_{\mathrm{vib}} \left| n_s \right\rangle = E_{\mathrm{vib}} \left| n_s \right\rangle = \sum_s \hbar\omega_s \left(n_s + \frac{1}{2} \right) \left| n_s \right\rangle. \tag{2.49}$$

The energy spectrum ε_s of this vibrational system is thus given by

$$\varepsilon_s = \hbar\omega_s\left(n_s + \frac{1}{2}\right). \tag{2.50}$$

where $E_{\text{vib}} = \sum_s \varepsilon_s$. According to statistical thermodynamics (See the detail description in the following Chapter), all the thermodynamic properties can be determined by the energy spectrum through the partition function Z or free energy F_{vib}, i.e.

$$F_{\text{vib}} = -k_{\text{B}}T\ln Z = -k_{\text{B}}T\ln\left(\sum_s e^{-\varepsilon_s/k_{\text{B}}T}\right). \tag{2.51}$$

Substitute Eq. (2.50) into Eq. (2.51), we have

$$Z = \prod_s \frac{e^{-\hbar\omega_s/2k_{\text{B}}T}}{1-e^{-\hbar\omega_s/k_{\text{B}}T}}, \tag{2.52a}$$

$$F_{\text{vib}} = \frac{1}{2}\sum_s \hbar\omega_s + k_{\text{B}}T\sum_s \ln\left(1-e^{-\hbar\omega_s/k_{\text{B}}T}\right). \tag{2.52b}$$

Therefore, the total free energy involving the ground-state potential is given by

$$\begin{aligned} F &= U_0 + F_{\text{vib}} \\ &= U_0 + \frac{1}{2}\sum_s \hbar\omega_s + k_{\text{B}}T\sum_s \ln\left(1-e^{-\hbar\omega_s/k_{\text{B}}T}\right). \end{aligned} \tag{2.53}$$

It should be noted that U_0 and ω_s would modified by the changes of atomic equilibrium positions due to the deformation of crystal. If we consider the isotropic deformation and denote it by the total volume of crystal V, both U_0 and ω_s in Eq. (2.53) are functions of V. In this regard, the entropy and energy

can be derived from the total free energy, i.e.

$$S = -\left(\frac{\partial F}{\partial T}\right)_V , \tag{2.54a}$$

$$\begin{aligned} E &= F + TS = F - T\left(\frac{\partial F}{\partial T}\right)_V \\ &= U_0 + \frac{1}{2}\sum_s \hbar\omega_s + k_\mathrm{B}T\sum_s \frac{\hbar\omega_s / k_\mathrm{B}T}{e^{\hbar\omega_s/k_\mathrm{B}T} - 1} \end{aligned} . \tag{2.54b}$$

The heat capacity is written as the derivative of energy against temperature, as

$$C_V = \left(\frac{\partial E}{\partial T}\right)_V = k_\mathrm{B}\sum_s \frac{\left(\hbar\omega_s / k_\mathrm{B}T\right)^2 e^{\hbar\omega_s/k_\mathrm{B}T}}{\left(e^{\hbar\omega_s/k_\mathrm{B}T} - 1\right)^2} . \tag{2.55}$$

Apparently, when $T = 0\mathrm{K}$, $E = U_0 + \frac{1}{2}\sum_s \hbar\omega_s$ in Eq. (2.54b), consistent with the foregoing discussion. However, at the high temperature, where $k_\mathrm{B}T \gg \hbar\omega_s$, the total energy can be expanded in a Taylor series of the term $x = \hbar\omega_s / k_\mathrm{B}T$, and we have the approximated expression, i.e.

$$E \cong U_0 + \frac{1}{2}\sum_s \hbar\omega_s + 3Nk_\mathrm{B}T , \tag{2.56}$$

thus $C_V \cong 3Nk_\mathrm{B}$. These relations reflect the classical equipartition law, and the consequent Dulong-Petit law, which is valid at high temperature, where the vibrational modes are excited to high energy level, and where quantum effects are unimportant.

Furthermore, at high temperature of classical limit, the zero-point energy can

be neglected, and the distribution of the occupation number for the normal mode tends to obey the Boltzmann distribution, i.e.

$$\langle n_s \rangle = e^{-\hbar\omega_s / k_B T}, \tag{2.57}$$

and the free energy can be simplified as

$$F \approx U_0 + k_B T \sum_s \ln\left(\frac{\hbar\omega_s}{k_B T}\right), \tag{2.58}$$

Especially when imposing the Einstein mode, in which all the vibration modes frequency are assumed to be equal to the unique one, i.e. $\omega_s = \omega_0$, thus

$$F = U_0 + 3Nk_B T \ln\xi \qquad \left(\xi = \hbar\omega_0 / k_B T\right). \tag{2.59}$$

Consequently, the energy and entropy is approximately given by

$$E = Nk_B T, \tag{2.60a}$$

$$S = 3Nk_B\left(1 - \ln\xi\right) \qquad \left(\xi = \hbar\omega_s / k_B T\right). \tag{2.60b}$$

The above description, i.e. Eq. (2.58), (2.59) & (2.60), are the typical results of an ensemble of classical harmonic oscillators with a uniform natural frequency ω_0, which is independent of the total volume.

2.2.4 Anharmonic effects

In the foregoing description, the lattice potential is truncated at the quadratic

order, from which we translate the coupled lattice dynamics into the uncoupled vibration modes of the crystal, or phonons, that depend only on the force-constants. In the harmonic approximation, the lattice displacements away from their equilibrium position are so small that higher order terms in the Taylor series of expansion of lattice potential are negligible, causing the vibration frequencies of phonons are not related to the vibrational amplitudes. However, at the higher temperature, the vibrational amplitudes are large enough to sample the anharmonic region of the potential, where the high-order terms of the expansion of potential cannot be neglected. Anharmonicity results in the scattering among phonons, and is the cause of finite thermal conductivity and thermal expansion in solids described by the thermal expansion coefficient α, i.e.

$$\alpha = \frac{1}{V}\left(\frac{\mathrm{d}V}{\mathrm{d}T}\right)_P . \tag{2.61}$$

Also force-constant and elastic constants are functions of temperature or pressure. In addition, the *isothermal elastic constants* are not equal to the *adiabatic elastic constants.*

Although the vibrational frequencies of normal modes are no longer good quantum number due to the anharmonicity of the crystal potential, one can still use the description of vibrations in terms of phonons with characteristic frequencies written as [20]

$$\omega(\boldsymbol{q}) = \omega_0(\boldsymbol{q}) + \Delta\omega(\boldsymbol{q}) - \mathrm{i}\Gamma(\boldsymbol{q}), \tag{2.62}$$

where $\omega(\boldsymbol{q})$ is the so-called "renormalized" phonon frequency, $\omega_0(\boldsymbol{q})$ is the harmonic frequency. The term $-\mathrm{i}\Gamma(\boldsymbol{q})$ represents the damping effect due to multi-phonon scattering, and $\Gamma(\boldsymbol{q})$ is the broadening of the phonon spectral density which can be measured by neutron scattering experiment, from which the phonon lifetime τ can be deduced, $\tau = (2\Gamma)^{-1}$. A finite phonon life time is the cause of a finite thermal conductivity due to the phonons. $\Delta\omega(\boldsymbol{q})$ denotes the frequency shift due to the anharmonicity of the crystal potential.

We consider the simple case that a one-dimensional oscillator suffers a potential involving the anharmonicity, which is

$$U(x) = \frac{1}{2}m\omega^2 x^2 + gx^3 + hx^4, \tag{2.63}$$

where higher order term are neglected. In the harmonic case, $g = h = 0$, it results in the energy $E_n = (n + 1/2)\hbar\omega$. If we apply the quantum mechanical perturbation theory to the state $|n\rangle$ at $T = 0\mathrm{K}$, we have the energy shift ΔE_n, which can be written

$$\Delta E_n = \langle n | hx^4 | n \rangle + \sum_{n \neq n'} \frac{\left| \langle n | gx^3 + hx^4 | n' \rangle \right|^2}{E_{n'} - E_n}. \tag{2.64}$$

Here $\langle n | gx^3 | n \rangle = 0$, since the integral in this term is an odd function of x and the integration is over the negative and positive x. The contribution of hx^4 in

the last term of the right hand side in Eq. (2.64) is smaller than that of gx^3, which can be dropped. However, it is necessary to keep both of these non-zero terms associated with gx^3 and hx^4, respectively, denoted by $\Delta\omega_3$ and $\Delta\omega_4$, since gx^3 is in a higher-order perturbation contribution. Therefore, by neglecting damping of the phonons, we have

$$\omega = \omega_0 + \Delta\omega_2 + \Delta\omega_3 + \Delta\omega_4, \tag{2.65}$$

where ω_0 is the harmonic frequency at the reference volume, and $\Delta\omega_3$ and $\Delta\omega_4$ are the frequency shifts due to explicit anharmonic terms in potential, whereas $\Delta\omega_2$ is related to the change in force-constants due to the softening or stiffening of the parabolic potential, respectively, arising from thermal expansion or applied external pressure. The so-called quasi-harmonic approximation is that only $\omega_0 + \Delta\omega_2$ is retained in Eq. (2.65).

In thermodynamics, the Grüneisen parameter is defined to describe the anharmonic effect, i.e., the volume dependence of the change in phonon frequency,

$$\gamma(V,T) = -\frac{\partial \ln \omega(V,T)}{\partial \ln V} = -\frac{V}{\omega}\frac{\partial \omega}{\partial V}, \tag{2.66}$$

where it is assumed all the phonon modes are of equal volume dependence. However, it is burdensome task to calculate the Grüneisen parameter using Eq. (2.66). In this regard, the widely used formula of Grüneisen parameter is derived

from the thermodynamics relations as

$$\gamma\left(V,T\right)=\frac{3\alpha VB_T}{C_V}=\frac{3\alpha VB_S}{C_P}, \tag{2.67}$$

where B_T and B_S are the isothermal and adiabatic bulk moduli, respectively, and C_V and C_P are the heat capacity at constant volume and constant pressure, respectively. Eq. (2.67) is often adopted for convenience. However, the Grüneisen parameter is firstly derived from Mie-Grüneisen's equation of state [22] in the form

$$\gamma=\frac{V}{E_{\text{vib}}}\left(\frac{\mathrm{d}U_0}{\mathrm{d}V}+P\right), \tag{2.68}$$

where U_0 and E_{vib} are the ground state potential energy and vibrational energy, respectively, and P is the pressure. In the first approximation, γ does not depend on the magnitude of the change in V for small compression or expansion around the reference volume, and the temperature dependence comes through the dependence of the reference volume on temperature, i.e. $V=V\left(T,P\right)$. However, while there are other thermal excitations, i.e. spin wave (magnon) that will be discussed in the following Section, the temperature dependence of γ is possibly complicated.

2.2.5 Elastic properties

In this subsection, we will present the basic relations of the elasticity of

crystalline solid, and its thermodynamic description. Detailed derivations can be found from the standard textbooks, such as Ref. [2,20,21].

Within the continuum elastic theory, i.e., neglecting the discrete nature of the crystal lattice, elastic properties can be treated as the long-wavelength limit of lattice vibrations. According to Hook's law, the elastic strain ε_{kl} is related to the stress σ_{ij}, i.e.

$$\sigma_{ij} = \sum_{k,l=1}^{3} c_{ijkl}\varepsilon_{kl} , \tag{2.69}$$

where i, j, k and l are indices running from 1 to 3, representing Cartesian components, i.e. *x*, *y*, and *z*, respectively. $\tilde{c} = \{c_{ijkl}\}$ is a fourth-rank stiffness tensor, containing 81 elements c_{ijkl}, namely the elastic constants. For convention, they are usually arranged in a 6×6 matrix with elements of $c_{\alpha\beta}$, so that Eq. (2.69) can be written as

$$\sigma_{\alpha} = \sum_{\beta=1}^{6} c_{\alpha\beta}\varepsilon_{\beta} , \tag{2.70}$$

where the summation index β running from 1 to 6, defined by

$$1 \equiv xx; \quad 2 \equiv yy; \quad 3 \equiv zz; \quad 4 \equiv yz; \quad 5 \equiv zx; \quad 6 \equiv xy . \tag{2.71}$$

Due to the symmetry of the crystal, not all the elements of $\tilde{c}$ are independent. For instance, there are only three independent elements in a cubic

crystalline solid, i.e. c_{11}, c_{12} and c_{44}, and its stiffness tensor is written as

$$\tilde{c}=\begin{pmatrix} c_{11} & c_{12} & c_{12} & 0 & 0 & 0 \\ c_{12} & c_{11} & c_{12} & 0 & 0 & 0 \\ c_{12} & c_{12} & c_{11} & 0 & 0 & 0 \\ 0 & 0 & 0 & c_{44} & 0 & 0 \\ 0 & 0 & 0 & 0 & c_{44} & 0 \\ 0 & 0 & 0 & 0 & 0 & c_{44} \end{pmatrix}. \tag{2.72}$$

At finite temperature, the deformation process due to the application of an external stress σ_α, is a thermodynamic process, accompanying with the change in energy $\mathrm{d}E$ and heat transfer $T\mathrm{d}S$, which can be described by the relation

$$\mathrm{d}E = T\mathrm{d}S + V\sum_{\alpha=1}^{6}\sigma_\alpha \mathrm{d}\varepsilon_\alpha \,. \tag{2.73}$$

It is obvious that if the strain is applied adiabatically, i.e., with no heat transfer ($\mathrm{d}S = 0$), the stress tensor is given by

$$\sigma_\alpha = \frac{1}{V}\left(\frac{\partial E}{\partial \varepsilon_\alpha}\right)_S, \tag{2.74}$$

where the subscript S means that the derivation is taken at constant entropy. In this regard, the elastic constants $c_{\alpha\beta}$ can be given by

$$\left(c_{\alpha\beta}\right)_S = \left(\frac{\partial \sigma_\alpha}{\partial \varepsilon_\beta}\right)_S = \frac{1}{V}\left(\frac{\partial^2 E}{\partial \varepsilon_\alpha \partial \varepsilon_\beta}\right)_S, \tag{2.75}$$

Therefore, elastic constants $c_{\alpha\beta}$ derived from Eq. (2.75) are called *adiabatic elastic constants*. On the other hand, we can also define the *isothermal elastic*

constants in an isothermal deformation process, starting from the Helmholtz free energy F, i.e.

$$\mathrm{d}F = -S\mathrm{d}T + V\sum_{\alpha=1}^{6}\sigma_\alpha \mathrm{d}\varepsilon_\alpha \ . \tag{2.76}$$

With constant temperature condition ($\mathrm{d}T = 0$), the isothermal elastic constants are given by

$$\left(c_{\alpha\beta}\right)_T = \left(\frac{\partial\sigma_\alpha}{\partial\varepsilon_\beta}\right)_T = \frac{1}{V}\left(\frac{\partial^2 F}{\partial\varepsilon_\alpha\partial\varepsilon_\beta}\right)_T \ . \tag{2.77}$$

In the above description, the deformation is sufficiently small so that Hook's law, i.e. Eq. (2.69), is valid. Otherwise, in the non-elastic region, the elastic constants would be the function of the applied stress or strain. In addition, within the harmonic approximation, these two set of elastic constants are equal to each other, i.e. $\left(c_{\alpha\beta}\right)_S = \left(c_{\alpha\beta}\right)_T$, and both are temperature independent. However, as mentioned in the foregoing, anharmonicity results in $\left(c_{\alpha\beta}\right)_S \neq \left(c_{\alpha\beta}\right)_T$ and the temperature dependence of $c_{\alpha\beta}$ [23].

2.3 Spin Dynamics

In Section 2.1.5, the Heisenberg Hamiltonian for ferromagnetic metals that have a net atomic spin is deduced in Eq. (2.29). In this Section, we will give a brief review of the thermodynamic contributions from the spin degrees of freedom, by introducing the low-lying magnetic excitation, i.e. spin wave

(magnon) [24].

2.3.1 Frozen lattice ground state of the ferromagnetic system

Let's consider the isotropic ferromagnetic system involving N atoms, each with spin S. The atoms are frozen in their equilibrium positions, so that the Hamiltonian is given by the Heisenberg-type exchange interaction, i.e.

$$H_S = -\frac{1}{2}\sum_{i\neq j} J_{ij}\hat{\boldsymbol{S}}_i \cdot \hat{\boldsymbol{S}}_j \,. \tag{2.78}$$

In quantum mechanics, the components of spin operator $\hat{\boldsymbol{S}}_i = \left(\hat{S}_i^x, \hat{S}_i^y, \hat{S}_i^z\right)$ obey the following commutation relation,

$$\left[\hat{S}_i^x, \hat{S}_j^y\right] = \mathrm{i}\hbar\hat{S}_i^z\delta_{ij}, \quad \text{(with } x, y, z \text{ circle)}. \tag{2.79}$$

In addition, we can define the spin operators, $\hat{S}_i^-$ and $\hat{S}_i^+$, respectively, as $\hat{S}_i^- = \hat{S}_i^x - \mathrm{i}\hat{S}_i^y$ and $\hat{S}_i^+ = \hat{S}_i^x + \mathrm{i}\hat{S}_i^y$, with the relations

$$\left[\hat{S}_i^\pm, \hat{S}_j^z\right] = \mp\hbar\hat{S}_i^\pm\delta_{ij}, \tag{2.80a}$$

$$\left[\hat{S}_i^+, \hat{S}_j^-\right] = 2\hbar\hat{S}_i^z\delta_{ij}. \tag{2.80b}$$

If $\hat{S}_i^-$ and $\hat{S}_i^+$ act on the single spin state $|S,m\rangle$, which is the eigen-state of $\left(\hat{\boldsymbol{S}}_i, \hat{S}_i^z\right)$, we have

$$\hat{S}_i^+|S,m\rangle = \sqrt{(S-m)(S+m+1)}\,|S,m+1\rangle, \tag{2.81a}$$

$$\hat{S}_i^- \left| S,m \right\rangle = \sqrt{(S-m)(S-m+1)} \left| S,m-1 \right\rangle . \tag{2.81b}$$

Therefore, the Hamiltonian in Eq. (2.78) can be rewritten as

$$H_S = -\frac{1}{2}\sum_{i\neq j} J_{ij} \left\{ \hat{S}_i^z \hat{S}_j^z + \frac{1}{2}\left(\hat{S}_i^+ \hat{S}_j^- + \hat{S}_i^- \hat{S}_j^+ \right) \right\}, \tag{2.82}$$

It can be rigorously proved that the ground state of ferromagnetic material ($J_{ij} > 0$) can be defined as

$$\left| 0 \right\rangle \equiv \left| S \right\rangle_1 \left| S \right\rangle_2 \cdots \left| S \right\rangle_i \cdots \left| S \right\rangle_N , \qquad \left(\left| S \right\rangle_i \equiv \left| S, m = S \right\rangle_i \right). \tag{2.83}$$

The ground state energy E_0 of the spin system is thus given by

$$H_S \left| 0 \right\rangle = -\frac{1}{2}\sum_{i\neq j} J_{ij} \hat{S}_i^z \hat{S}_j^z \left| 0 \right\rangle = -\frac{1}{2}\sum_{i\neq j} J_{ij} S^2 \left| 0 \right\rangle \equiv E_0 \left| 0 \right\rangle , \tag{2.84}$$

where we have used the relation, $\hat{S}_i^+ \left| 0 \right\rangle = 0$, and S^2 results from the maximum eigenvalue of $\hat{S}_i^z$, i.e. $m = S$, at the ground state $\left| 0 \right\rangle$.

Apparently, for other spin configurations different from the ground state, there is at least one spin with $m < S$, leading to a total energy larger than E_0. In this regard, the state $\left| 0 \right\rangle$ with all the spins parallel along *z*-axis is indeed the ground state of ferromagnetism.

2.3.2 Holstein-Primakoff transformation

Correspondingly, the first excited state is the spin configuration that the

projection along the quantized axis of one arbitrary spin, i.e. m_i, deviates from its maximum value S to $(S-1)$, such as

$$\left|(S-1)_i\right\rangle \equiv \left|S\right\rangle_1 \cdots \left|S-1\right\rangle_i \left|S\right\rangle_j \cdots \left|S\right\rangle_N , \tag{2.85}$$

However, the effect of the term $\hat{S}_i^+ \hat{S}_j^-$ in H_S causes the disappearance of such deviation at spin i, and creates a new deviation at spin j, so that the state $\left|(S-1)_i\right\rangle$ becomes $\left|(S-1)_j\right\rangle$ (See in Fig. 2.1),

$$\left|(S-1)_j\right\rangle \equiv \left|S\right\rangle_1 \cdots \left|S\right\rangle_i \left|S-1\right\rangle_j \cdots \left|S\right\rangle_N . \tag{2.86}$$

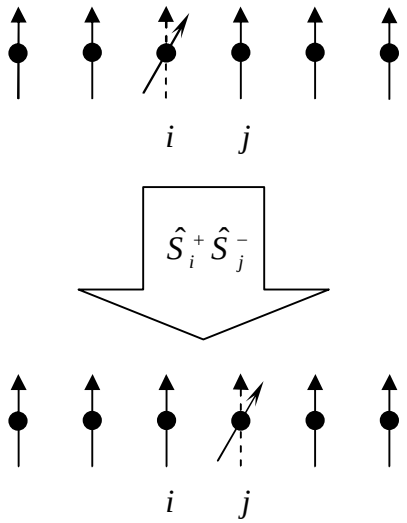

Fig. 2.1: The schematic of the propagation of spin deviation from spin i to j due to the effects of coupling term $\hat{S}_i^+ \hat{S}_j^-$ in the Hamiltonian, Eq. (2.82).

In this regard, the deviation of the spin-state is not concentrated at one spin, but spreads and propagates along the whole magnetic crystal due to the coupling terms in Eq. (2.82), in the form of collective excitations, namely spin waves, which is similar to the case of lattice waves (See in Fig. 2.2).

(a) Stereogram

(b) Top view

Fig. 2.2: The classical picture of spin wave with a specific wave-vector: (a) stereogram and (b) top view. There is an equal phase difference between the adjacent spins, which is determined by the product of their spacing and the wave-vector.

In order to diagonalize the coupled Hamiltonian in Eq. (2.82), we introduce the deviation n to represent a spin state, and the corresponding annihilation and creation operators, $\hat{a}$ and $\hat{a}^+$, in analogy to the case of phonons, as

$$n \equiv S - m \qquad (m = 0, \pm 1, \cdots, \pm S), \tag{2.87}$$

$$\hat{a}|n\rangle = \sqrt{n}\,|n-1\rangle, \quad \hat{a}^+|n\rangle = \sqrt{n+1}\,|n+1\rangle, \tag{2.88}$$

Therefore, the spin operators $\hat{S}^z$, $\hat{S}^-$ and $\hat{S}^+$ can be expressed in terms of $\hat{a}$ and $\hat{a}^+$, respectively, as

$$\hat{S}^+ = \left(\sqrt{2S - \hat{a}^+\hat{a}}\right)\hat{a}, \tag{2.89a}$$

$$\hat{S}^- = \hat{a}^+\left(\sqrt{2S - \hat{a}^+\hat{a}}\right), \tag{2.89b}$$

$$\hat{S}^z = \left(S - \hat{a}^+\hat{a}\right). \tag{2.89c}$$

This is the Holstein-Primakoff (HP) transformation. Accordingly, Eq. (2.81) can be rewritten as,

$$\hat{S}^{+}\left|n\right\rangle=\sqrt{2S-(n-1)}\sqrt{n}\left|n-1\right\rangle, \tag{2.90a}$$

$$\hat{S}^{-}\left|n\right\rangle=\sqrt{2S-n}\sqrt{n+1}\left|n+1\right\rangle. \tag{2.90b}$$

From these relations, we can obtain the second quantized Heisenberg Hamiltonian,

$$\begin{aligned} H_S=-\frac{1}{2}\sum_{i\neq j}J_{ij}\Big\{&\left(S-\hat{a}_i^{+}\hat{a}_i\right)\left(S-\hat{a}_j^{+}\hat{a}_j\right)\\ &+\frac{1}{2}\sqrt{2S-\hat{a}_i^{+}a_i}\left(\hat{a}_i\hat{a}_j^{+}\right)\sqrt{2S-\hat{a}_j^{+}\hat{a}_j}\\ &+\frac{1}{2}\hat{a}_i^{+}\sqrt{2S-\hat{a}_i^{+}\hat{a}_i}\sqrt{2S-\hat{a}_j^{+}\hat{a}_j}\hat{a}_j\Big\}\end{aligned}. \tag{2.91}$$

Eq. (2.91) involves the square root term of $\hat{a}^{+}\hat{a}$, corresponding to the deviation quantum number n, giving rise to the complexity of the Hamiltonian. The excited states ($n>0$) are difficult to solve rigorously as the eigen-state of H_S. Fortunately, approximate solutions can be obtained for low-lying excited states, which are sufficient for low temperature considerations far from the magnetic transition point, where the spin deviation is small, i.e. $\left\langle\hat{a}^{+}\hat{a}\right\rangle=n\ll 2S$.

2.3.3 Low-lying excited state: spin wave

At low temperatures, the square root terms in Eq. (2.91) can be replaced by $\sqrt{2S}$ approximately, and the zero-order Hamiltonian H_0 can be written as

$$H_0 = E_0 + \sum_j \sum_{i,i\neq j} J_{ij} S \hat{a}_i^+ \hat{a}_i - \frac{1}{2} \sum_{i\neq j} J_{ij} S \left(\hat{a}_i \hat{a}_j^+ + \hat{a}_i^+ \hat{a}_j \right), \tag{2.92}$$

where, the first term in the right hand side is the ground state energy, and the second term represents the energy arising from the deviation of the ith spin, whereas the third term is the coupling between different spins, which is similar to the harmonic Hamiltonian of lattice dynamics, shown in Eq. (2.35). Therefore, by introducing the Fourier transform of $\hat{a}_i$ and $\hat{a}_i^+$, as

$$\hat{b}_q = N^{-\frac{1}{2}} \sum_i e^{-i\boldsymbol{q}\cdot\boldsymbol{R}_i^0} \hat{a}_i , \tag{2.93a}$$

$$\hat{b}_q^+ = N^{-\frac{1}{2}} \sum_i e^{-i\boldsymbol{q}\cdot\boldsymbol{R}_i^0} \hat{a}_i^+ , \tag{2.93b}$$

we can diagonalize H_0,

$$\begin{aligned} H_0 &= E_0 + \sum_{\boldsymbol{q}} J(0) S \hat{b}_{\boldsymbol{q}}^+ \hat{b}_{\boldsymbol{q}} - \frac{1}{2} \sum_{\boldsymbol{q}} J(\boldsymbol{q}) S \left(\hat{b}_{\boldsymbol{q}} \hat{b}_{\boldsymbol{q}}^+ + \hat{b}_{\boldsymbol{q}}^+ \hat{b}_{\boldsymbol{q}} \right) \\ &= E_0 + \sum_{\boldsymbol{q}} J(0) S \hat{b}_{\boldsymbol{q}}^+ \hat{b}_{\boldsymbol{q}} - \frac{1}{2} \sum_{\boldsymbol{q}} J(\boldsymbol{q}) S \left(\hat{b}_{\boldsymbol{q}} \hat{b}_{\boldsymbol{q}}^+ + \hat{b}_{\boldsymbol{q}} \hat{b}_{\boldsymbol{q}}^+ + 1 \right) \\ &= E_0 + \sum_{\boldsymbol{q}} \left(J(0) - J(\boldsymbol{q}) \right) S \hat{b}_{\boldsymbol{q}}^+ \hat{b}_{\boldsymbol{q}} - \frac{1}{2} \sum_{\boldsymbol{q}} J(\boldsymbol{q}) S \\ &= E_0 + \sum_{\boldsymbol{q}} \hbar \omega_{\boldsymbol{q}} \hat{b}_{\boldsymbol{q}}^+ \hat{b}_{\boldsymbol{q}} \end{aligned} , \tag{2.94}$$

where $\omega_{\boldsymbol{q}}$ is the frequency of spin wave, thus $\hbar\omega_{\boldsymbol{q}}$ is a quantum of the spin wave, or magnon,

$$\hbar\omega_q = \left\{ J(0) - J(q) \right\} S , \tag{2.95}$$

with $J(q)=\sum_j J_{ij}\exp\left\{-\mathrm{i}\boldsymbol{q}\cdot\left(\boldsymbol{R}_i^0-\boldsymbol{R}_j^0\right)\right\}$. Here in Eq. (2.94), $\sum_{\boldsymbol{q}} J(\boldsymbol{q})S\equiv 0$, there is thus no zero-point energy in ferromagnetic magnon. If only the first-nearest-neighbor (1st-NN) spin-spin interaction is considered in a cubic crystal, Eq. (2.95) can be simplified as

$$\hbar\omega_q = ZJ_{ij}^{1\mathrm{NN}}S\left(1-\gamma_q\right), \tag{2.96}$$

with the structure factor of spin wave γ_q,

$$\gamma_q = Z^{-1}\sum_{\boldsymbol{\delta}} e^{-\mathrm{i}\mathbf{q}\cdot\boldsymbol{\delta}} \qquad \left(\boldsymbol{\delta}\equiv\boldsymbol{R}_i^0-\boldsymbol{R}_j^0\right), \tag{2.97}$$

where Z is the coordinate number of 1st NN.

2.3.4 Spin dispersion relation at long-wavelength limit

The dispersion relation of the magnons, i.e., the relation between the frequency ω_q and its wave-vector q, can be derived from Eq. (2.96). Therefore, at low temperature and for long wave-length, i.e. $|\boldsymbol{q}\cdot\boldsymbol{\delta}|\ll 1$, we have

$$\begin{aligned}\hbar\omega_q &= ZJ_{ij}^{1\mathrm{NN}}S\left(1-\gamma_q\right)\\ &\approx J_{ij}^{1\mathrm{NN}}S\left\{Z-\sum_{\boldsymbol{\delta}}\left[1-\frac{1}{2}\left(\boldsymbol{q}\cdot\boldsymbol{\delta}\right)^2\right]\right\}\\ &= J_{ij}^{1\mathrm{NN}}S\sum_{\boldsymbol{\delta}}\left(\boldsymbol{q}\cdot\boldsymbol{\delta}\right)^2\\ &= J_{ij}^{1\mathrm{NN}}SZ^{-1}q^2\sum_{\boldsymbol{\delta}} Z\delta^2\cos^2\theta\left(\widehat{\boldsymbol{q},\boldsymbol{\delta}}\right)\end{aligned}. \tag{2.98}$$

In cubic crystal, i.e. simple cubic (SC), body-centered cubic (BCC) and face-centered cubic (FCC), we have

$$\hbar\omega_q = J_{ij}^{1\mathrm{NN}} S a^2 q^2 , \tag{2.99}$$

where $\cos^2\theta\left(\widehat{\boldsymbol{q},\boldsymbol{\delta}}\right) = 1/3$ and $Z\delta^2 = 6a^2$, a being the lattice parameter. Obviously, BCC iron involving both 1st- and 2nd-NN spin-spin interactions can be regarded as the sum of a BCC sub-crystal containing 1st-NN with exchange strength being $J_{ij}^{1\mathrm{NN}}$ and an SC sub-crystal containing 1st-NN with exchange strength being $J_{ij}^{2\mathrm{NN}}$, which both sub-crystals have the same lattice constant a. Therefore the dispersion relation can be written as

$$\hbar\omega_q = \left(J_{ij}^{1\mathrm{NN}} + J_{ij}^{2\mathrm{NN}}\right) S a^2 q^2 , \tag{2.100}$$

from which the so-called spin stiffness D is given by

$$D = \left(J_{ij}^{1\mathrm{NN}} + J_{ij}^{2\mathrm{NN}}\right) S a^2 , \tag{2.101}$$

Thus, $\hbar\omega_q = Dq^2$ at the long-wavelength limit. Here we have assumed the frequency of spin wave ω_q is not related to the direction of $\boldsymbol{q}$ due to the isotropic nature of J_{ij}.

2.3.5 Anharmonic effects in ferromagnetic system

As shown in Eq. (2.94), H_0 is called the Hamiltonian under spin-wave approximation, where $\hat{b}_q^+ \hat{b}_q \equiv \hat{n}_q$ represents the occupation operator of magnon, whose eigen-value is the occupation number of magnon of $\boldsymbol{q}$. Since magnons are bosons, the occupation number $\hat{n}_q$ obeys the Bose-Einstein distribution at

finite temperature T,

$$\left\langle \hat{n}_q \right\rangle_T = \left(e^{\hbar\omega_q / k_B T} - 1 \right)^{-1}. \tag{2.102}$$

On the other side, if we expand the square root terms in Eq. (2.91) in the form

$$\sqrt{1 - \frac{\hat{a}^+ \hat{a}}{2S}} = 1 - \frac{1}{2}\left(\frac{\hat{a}^+ \hat{a}}{2S} \right) + \frac{1}{8}\left(\frac{\hat{a}^+ \hat{a}}{2S} \right)^2 + \cdots, \tag{2.103}$$

and take account the high order terms of operators, then

$$H_S = H_0 + H_1 + \cdots, \tag{2.104}$$

where the term H_1 is written as

$$H_1 = \frac{ZJ}{4N} \sum_{q,q',k} \left(\gamma_{q-k} + \gamma_{q'} - 2\gamma_{q-k-q'} \right) \hat{b}^+_{q-k} \hat{b}^+_{q'+k} \hat{b}_{q'} \hat{b}_q, \tag{2.105}$$

which stands for the magnon-magnon interactions, and which produces anharmonic effects in the system of spin waves. From Eq. (2.94), the spin-wave is just the linear solution of the time dependent Schrödinger equation,

$$\mathrm{i}\hbar \frac{\partial \hat{b}_q}{\partial t} = \left[\hat{b}_q, H_0 \right] = \hbar\omega_q \hat{b}_q. \tag{2.106}$$

Therefore, in considering the perturbation incurred by H_1, the Schrödinger equation is corrected by introducing the temperature dependent magnon energy

$\hbar\omega_q(T)$, as

$$\mathrm{i}\hbar\frac{\partial\hat{b}_q}{\partial t}=\hbar\omega_q(T)\hat{b}_q, \tag{2.107}$$

where

$$\hbar\omega_q(T)=ZJ_{ij}^{1\mathrm{NN}}S\left(1-\gamma_q\right)f(T), \tag{2.108}$$

$$f(T)\equiv\frac{1-e(T)}{S}, \text{ with } e(T)\equiv N^{-1}\sum_{q'}\left(1-\gamma_{q'}\right)\left\langle\hat{n}_{q'}\right\rangle_T. \tag{2.109}$$

From Eq. (2.108), it can be seen that the correction factor $f(T)$, due to the magnon-magnon interactions incurred by H_1, decreases with increasing temperature, resulting in the softening of magnon modes, which finally may become unstable at higher temperatures near magnetic transition boundary, i.e. Curie temperature.

In addition, there are other higher order terms neglected in Eq. (2.104), representing the multi-magnon interactions. Similar to the case of phonons, with the temperature increases, those multi-magnon interactions become important, which, accompanying with H_1, can produce a shift of the characteristic magnon frequencies, and a reduction of the magnon lifetime, as expressed in Eq. (2.62).

2.3.6 Classical treatment of spin dynamics

In this subsection, we will present an alternate treatment of spin dynamics,

starting also from the general translationally invariant exchange Hamiltonian,

$$H_S = -\frac{1}{2}\sum_{i\neq j} J_{ij}\boldsymbol{S}_i \cdot \boldsymbol{S}_j \,, \tag{2.110}$$

by treating the spins as *c*-numbers of fixed length $|\boldsymbol{S}_i| = S$. Therefore the equation of motion of spin $\boldsymbol{S}_k$ can be derived as

$$\begin{aligned}\frac{\mathrm{d}\boldsymbol{S}_k}{\mathrm{d}t} &= \frac{\mathrm{i}}{\hbar}\left[H_S, \boldsymbol{S}_k\right] \\ &= -\frac{1}{\hbar}\left(\sum_{i\neq k}^{N} J_{ik}\boldsymbol{S}_i\right)\times \boldsymbol{S}_k \,, \\ &\equiv -\frac{1}{\hbar} g\mu_{\mathrm{B}}\boldsymbol{H}_k \times \boldsymbol{S}_k\end{aligned} \tag{2.111}$$

where $\boldsymbol{H}_k$ represents the effective magnetic field acting on spin $\boldsymbol{S}_k$, determined by the strength of exchange integral J_{ik} and the surrounding spins $\boldsymbol{S}_i$, which is defined as

$$\boldsymbol{H}_k \equiv \frac{1}{g\mu_{\mathrm{B}}}\sum_{i\neq k}^{N} J_{ik}\boldsymbol{S}_i \,. \tag{2.112}$$

Eq. (2.111) shows the classical dynamics picture in which the atomic spin is regarded as a classical vector, and precesses around an effective magnetic field due to its neighbors. The magnetization observed macroscopically is given by the ensemble average of the spin vector. Thermal fluctuations of the precession angle increase with increasing temperature, reducing collinearity from the saturation value at 0K. At the Curie temperature, collinearity is lost altogether and the

system crosses over from the FM into the PM phase. Collectively, the dynamics of all the spins are correlated, the motion of neighboring spins being coupled by the exchange interaction. Low-lying collective excitations below Curie temperature are in the form of spin waves, which the detailed classical derivation can be seen in Ref. [25]. The classical solution of spin wave of q is written as

$$S_q^\alpha(t) = \sum_i S_i^\alpha(t) e^{-i\boldsymbol{q}\cdot\boldsymbol{R}_i^0} \qquad (\alpha = x, y), \tag{2.113}$$

which is the classical expression for Eq. (2.93). In this regard, the spins can be pictured as the classical vectors rotating in the Oxy-plane, with equal phase difference between the adjacent spins, determined by $\boldsymbol{q}\cdot\boldsymbol{R}_i^0$, which is the origin of the classical picture of spin wave, as shown in Fig. 2.2.

2.3.7 Thermal properties

Analogous to phonons, the thermodynamic functions, e.g. free energy, entropy, etc., of the magnon system can be derived from the magnon partition function, constructed from thermal energy spectrum of the magnons, i.e.

$$E_{\text{th}}(T) = \sum_q \hbar\omega_q \langle n_q \rangle_T, \tag{2.114}$$

which is similar to the phonons, but without the zero point energy. Therefore, the thermodynamic functions have the similar forms as those for phonons, which we will not go into the details here.

At low temperatures, the density of magnons is low, and the spin-wave approximation gives a good description of magnetic properties in general. For instance, the magnetization obeys the so-called Bloch's $T^{3/2}$ law at low temperatures. However, since the magnon density increases with temperature, multi-magnon interactions cannot be neglected. In this regard, it is difficult to apply the spin-wave approximation at high temperatures, especially near the magnetic phase transition boundary. Within the classical picture of spin motion in the foregoing, the thermal behavior at high temperatures can be described based on the mean-field theory [26,27].

Eq. (2.112) defines the effectively field governing the spin motions. Within the mean field approximation, we may write

$$g\mu_{\mathrm{B}}\boldsymbol{H}_k = \sum_{i\neq k}^{N} J_{ik}\boldsymbol{S}_i \approx ZJS^z, \tag{2.115}$$

by replacing the instantaneous spin vector $\boldsymbol{S}_i$ by its mean value $\langle \boldsymbol{S} \rangle = S^z$, with $J \equiv J_{ik}$. Since the magnetization is given by $\boldsymbol{M} = g\mu_{\mathrm{B}} \langle \boldsymbol{S} \rangle$, the effective field is proportional to the magnetization, i.e. $\boldsymbol{H}_k \propto \boldsymbol{M}$, which is the Weiss molecule field. In this approximation, the effective field is assumed homogeneous and all the spins are aligned. The energy of a single spin ε_k is given by

$$\begin{aligned}\varepsilon_k &= -\frac{1}{2}\sum_i J_{ik}\left\langle \boldsymbol{S}_i\right\rangle\cdot\boldsymbol{S}_k - \frac{1}{2}\sum_i J_{ik}\boldsymbol{S}_k\cdot\left\langle \boldsymbol{S}_i\right\rangle \\ &= -\frac{1}{2}\sum_i J_{ik}S^z\boldsymbol{S}_k - \frac{1}{2}\sum_i J_{ik}\boldsymbol{S}_k S^z \\ &= -g\mu_{\mathrm{B}}\boldsymbol{H}_k\cdot\boldsymbol{S}_k\end{aligned} \quad . \qquad (2.116)$$

In this description, we translate the interactive spin system into an ensemble of uncoupled paramagnets in an external field, i.e. $\boldsymbol{H}_k = \sum_i J_{ik}S^z\mathbf{e}^z$, $\mathbf{e}^z$ being the unit vector along the z-axis, the quantized axis of spins. Apparently, the magnitude of such an external field varies with the temperature dependence of magnetization, i.e. $H_k \propto S^z = M(T)/g\mu_{\mathrm{B}}$. The partition function is then given by

$$\begin{aligned}Z_k &= \int_{-\pi}^{\pi}\exp\left(-\frac{g\mu_{\mathrm{B}}H_kS_k\cos\theta}{k_{\mathrm{B}}T}\right)\mathrm{d}\theta \\ &= 4\pi\frac{\sinh(x)}{x}\end{aligned}, \qquad \left(x = g\mu_{\mathrm{B}}H_kS_k/k_{\mathrm{B}}T\right) \qquad (2.117)$$

from which the corresponding free energy per spin is given by

$$\begin{aligned}F_S &= -k_{\mathrm{B}}T\ln Z_k \\ &= -Nk_{\mathrm{B}}T\ln\left\{4\pi\frac{\sinh(x)}{x}\right\},\end{aligned} \qquad \left(x = g\mu_{\mathrm{B}}H_kS_k/k_{\mathrm{B}}T\right). \qquad (2.118)$$

Other thermodynamic functions can be thus derived from F_S. In particular, when $T\to\infty$ ($x\to 0$), the spins are totally random, i.e. $\left\langle \boldsymbol{S}_k\right\rangle\to 0$, and the energy of the spin system tend to be zero. In addition, the entropy of such totally random spin system is given by [25]

$$\begin{aligned}\lim_{T\to\infty}\frac{S_S}{k_{\mathrm{B}}} &= -\lim_{T\to\infty}\frac{\mathrm{d}F_S}{\mathrm{d}T}\\ &= \lim_{x\to 0}\ln\left(4\pi\frac{\sinh(x)}{x}\right)\\ &\quad +\lim_{x\to 0}T\frac{\mathrm{d}}{\mathrm{d}T}\ln\left(4\pi\frac{\sinh(x)}{x}\right),\\ &= \ln(4\pi)+\lim_{x\to 0}TL(x)\\ &= \ln(4\pi)\end{aligned} \tag{2.119}$$

where $\lim_{x\to 0}\left(\sinh(x)/x\right)=1$, and $\lim_{x\to 0}L(x)=1/x+x/3$, with

$$L(x)=\coth(x)-1/x, \tag{2.120}$$

being the so-called Langevin function. The significance of Eq. (2.119) is apparent, since the phase-volume of the totally random spin system with fixed spin magnitude is equal to the spatial angle, i.e. $\Omega=4\pi$, so that the entropy is given by $S=k_{\mathrm{B}}\ln\Omega=k_{\mathrm{B}}\ln(4\pi)$, according to the Boltzmann's definition.

It should be noted that the mean-field theory reviewed above is a one-particle model, and only consider the effects arising from single spin motion in the average field of the neighboring spins. This means it cannot describe the effects of collective excitations at low temperatures. As a result, the magnetization decays exponentially with temperatures at low temperatures, instead of obeying the experimental $T^{3/2}$ law. However, the mean-field theory does provide a good description of the thermal properties of spin dynamics at high temperatures.

2.4 Phonon-Magnon Interaction

In the foregoing Sections, we have presented the thermodynamic natures of lattice and spin dynamics separately, in terms of phonons and magnons. However, as reviewed in Section 2.1.5, in a ferromagnetic system, the degrees of freedom of spin and lattice interacts. In this Section, we will discuss the contributions from spin-lattice coupling to the free energy of the whole system.

2.4.1 Spin-lattice coupling

From the equation of motion of a single spin in Eq. (2.111), the dynamics of spin system is determined by the exchange integrals, J_{ij}. It is well known that J_{ij}, being related to the overlap of the atomic orbits, is sensitive to the separation between atoms i and j. In the framework of density function theory (DFT), Sabiryanov *et al.* [28] calculated the dependence of exchange integral on intra-atomic distance of BCC-iron by using the linear-muffin-tin-orbital (LMTO) method, in which the 1st- and 2nd-NN exchange integrals are almost the linear function of the intra-atomic distance. However, the more detailed calculations of Wang *et al.* [29], show different atomic distance dependence between 1st-NN and 2nd-NN exchange integrals. In their calculation results, 1st-NN exchange integral includes the contributions from electron exchanges involving overlaps of both the t_{2g} and e_g electronic states, whereas the 2nd exchange integral involves the contribution from the overlap of e_g states only. Moreover, the

overlapping of the t_{2g} states decreases much faster with the atomic distance increasing than that of e_g states. In this regard, the complexity of the exchange integral as a function of intra-atomic distance is a many-body effect, due to the angular dependence of the electron charge distributions in the crystal structure.

At the same time, the MM calculated by WIEN2K and LMTO Green function vanishes as the lattice constant is compressed to around 2.3 angstrom, due to the limitation of available space for the onsite electrons to stay away from each other to minimize the effects of Pauli's exclusion and remain aligned. As the local atomic volume increases, the onsite electrons can avoid each other to minimize the coulomb repulsion and stay aligned to, increasing the MM. In this way, the local atomic volume determines the magnitude of the atomic MMs via the spin polarization of the on-site electrons. For example, a shift in the Curie temperature from 350K to 750K is observed experimentally in iron-rich compounds undergoing a volume expansion of ~6% [30]. At the same time, the dynamics of the atomic lattice is coupled to that of the atomic spins via the exchange interaction, giving rise to the phonon-magnon interaction [31]. In this regard, for a ferromagnetic material, i.e. BCC iron the phonon-magnon interaction affects the thermodynamics of both lattice (phonon) and spin (magnon) subsystem.

2.4.2 Hamiltonians and free energies

To separate the dynamics related to the spin and lattice degrees of freedom in the system of Heisenberg particles, the Hamiltonian H_H in Eq. (2.27) is rewritten as

$$H_H \equiv H_L(\boldsymbol{p},\boldsymbol{R}) + H_S(\boldsymbol{S}) + H_\Delta(\boldsymbol{R},\boldsymbol{S}), \tag{2.121}$$

where H_L and H_S are the Hamiltonians only containing the lattice and spin degree of freedom, respectively, whereas H_Δ represents their interaction. Assuming H_Δ is small compared with H_L and H_S, H_H is nearly separable, and then the corresponding partition function Z_H of the system in a canonical ensemble is thus derived as

$$\begin{aligned} Z_H &= \int e^{-\left\{H_L(\boldsymbol{p},\boldsymbol{R})+H_S(\boldsymbol{S})+H_\Delta(\boldsymbol{R},\boldsymbol{S})\right\}/k_B T}\mathrm{d}\boldsymbol{p}\mathrm{d}\boldsymbol{R}\mathrm{d}\boldsymbol{S} \\ &\approx \left\langle e^{-H_\Delta/k_B T}\right\rangle_{L+S} \int e^{-(H_L+H_S)/k_B T}\mathrm{d}\boldsymbol{p}\mathrm{d}\boldsymbol{R}\mathrm{d}\boldsymbol{S} \end{aligned} \tag{2.122}$$

where $\langle\cdots\rangle_{L+S}$ is the ensemble average over the phase space Ω governed by the Hamiltonian $H_{L+S} \equiv H_L + H_S$. Here, mid-point theorem of integration is used in the deduction of Eq. (2.122), in which $e^{-H_\Delta/k_B T}$ varies more slowly than $e^{-H_{L+S}/k_B T}$ by assuming $\langle H_\Delta\rangle \ll k_B T$. In this regard, Z_H is decomposed into three parts,

$$Z_H = \alpha_\Delta Z_L Z_S, \tag{2.123}$$

with

$$\alpha_\Delta = \left\langle e^{-H_\Delta/k_B T}\right\rangle_{L+S} \tag{2.124a}$$

$$Z_L = \int e^{-H_L(\boldsymbol{p},\boldsymbol{R})/k_{\mathrm{B}}T}\,\mathrm{d}\boldsymbol{p}\mathrm{d}\boldsymbol{R} \tag{2.124b}$$

$$Z_S = \int e^{-H_S(\boldsymbol{S})/k_{\mathrm{B}}T}\,\mathrm{d}\boldsymbol{S} \tag{2.124c}$$

Therefore, the free energy F_H derived from the partition function, Z_H, can be expressed as the summation of the corresponding free energies,

$$F_H \equiv F_L + F_S + F_\Delta, \tag{2.125}$$

where

$$F_L = -k_{\mathrm{B}}T\ln Z_L = -k_{\mathrm{B}}T\ln\left\{\int e^{-H_L/k_{\mathrm{B}}T}\,\mathrm{d}\boldsymbol{p}\mathrm{d}\boldsymbol{R}\right\} \tag{2.126a}$$

$$F_S = -k_{\mathrm{B}}T\ln Z_S = -k_{\mathrm{B}}T\ln\left\{\int e^{-H_S/k_{\mathrm{B}}T}\,\mathrm{d}\boldsymbol{S}\right\} \tag{2.126b}$$

$$F_\Delta = -k_{\mathrm{B}}T\ln\alpha_\Delta = -k_{\mathrm{B}}T\ln\left\langle e^{-H_\Delta/k_{\mathrm{B}}T}\right\rangle_{L+S} \tag{2.126c}$$

Therefore, we can define the Hamiltonians H_L, H_S and H_Δ in the forms,

$$H_L\left(\boldsymbol{R}\right) = \sum_{i=1}^{N}\frac{\boldsymbol{p}_i^2}{2m_i} + U\left(\boldsymbol{R}\right) \tag{2.127a}$$

$$H_S(\boldsymbol{S}) = -\frac{1}{2}\sum_{i\neq j}^{N} J_{ij}\left(\bar{\boldsymbol{R}}\right)\boldsymbol{S}_i\cdot\boldsymbol{S}_j \tag{2.127b}$$

$$H_\Delta(\boldsymbol{R},\boldsymbol{S}) = -\frac{1}{2}\sum_{i\neq j}^{N}\delta J_{ij}\boldsymbol{S}_i\cdot\boldsymbol{S}_j \tag{2.127c}$$

where $\delta J_{ij} = J_{ij}\left(\boldsymbol{R}\right) - J_{ij}\left(\bar{\boldsymbol{R}}\right)$ is the fluctuation of $J_{ij}\left(\boldsymbol{R}\right)$ around $J_{ij}\left(\bar{\boldsymbol{R}}\right)$, the one at the mean (time-averaged) lattice configuration $\bar{\boldsymbol{R}}$.

In this regard, the coupling of the spin and lattice degrees of freedom is separated in an ensemble of Heisenberg particles, and the free energy are thermodynamically decomposed into F_L, F_S and F_Δ, based on which the contribution of lattice waves (phonons), spin waves (magnons), and their mutual coupling, can be studied respectively with H_L, H_S and H_Δ.

Reference

[1] R. Martins, *Electronic Structure: Basic Theory and Practical Methods*, (Cambridge Univ. Press, Cambridge, 2004).

[2] M. Born and K. Huang, *Dynamical Theory of Crystal Lattices*, (Oxford University Press, London, 1954), pp. 166-173.

[3] M. Born, and R. Oppenheimer, Ann. D. Phys. **84**, 457 (1927).

[4] W. Heisenberg, Phys. Z **49**, 619 (1928).

[5] P. A. M. Dirac, Proc. Roy. Soc. **A123**, 714 (1929).

[6] P. W. Anderson, Solid State Phys. **14**, 99 (1963).

[7] J. Hubbard, Proc. Roy. Soc. London Ser. A **276**, 238 (1963).

[8] P. M. Derlet, S. L. Dudarev, Prog. Mater. Sci. **52**, 299 (2007).

[9] E. P. Wohlfarth, *Ferromagnetic Materials: A handbook on the properties of magnetically ordered substances*, *Vol. 1* (Elservier North-Holland, INC., 1980), Chapter 1.

[10] M. Pajda, J. Kudrnovsky, I. Turek, V. Drchal, and P. Bruno, Phys. Rev. B **64**, 174402 (2001).

[11] L. A. Turiski, Phys. Rev. B, **30**, 2779 (1984).

[12] I. P. Omelyan, I. M. Mryglod, and R. Folk, Phys. Rev. Lett. **86**, 898 (2001).

[13] J. H. van Vleck, *The Theory of Electric and Magnetic Susceptibilities*, (Oxford University Press, New York, 1932), Ch. XII, where the Dirac vector model and the standard Heisenberg theory are reviewed.

[14] M. Born and K. Huang, *Dynamical Theory of Crystal Lattices*, (Oxford University Press, London, 1954).

[15] H. Ibach and H. Lüth, *Solid-State Physics: An Introduction to Principles of Materials Science*, 4th ed., (Springer, 2009).

[16] A. Maradudin, E. Montroll, G. Weiss and I. Ipatova, *Theory of Lattice Dynamics in the Harmonic approximation*, 2nd ed., (Academic Press, New York, 1971).

[17] G. Venkataraman, L. Feldkamp and V. Sahni, *Dynamics of Perfect Crystals*, (MIT Press, Cambridge MA, 1975).

[18] P. Bruesch, Phonons: *Theory and Experiments. I, Lattice Dynamics and Models of Interatomic Forces*, (Springer-Verlag, Berlin, 1982).

[19] N. Ashcroft and N. Mermin, *Solid State Physics*, (Saunders College, Philadelphia, 1976).

[20] G. Grimvall, *Thermophysical Properties of Materials*, (enlarged and revised edition), (North Holland, Amsterdam, 1999).

[21] D. C. Wallace. *Thermodynamics of Crystals*, (Dover, Mineola, New York, 1999).

[22] M. Born, *Atomtheories des festen Zustandes* (2nd, ed., Teubner, 1923), pp. 652; E. Grüneisen, *Handb. der Phys.*, **10**, 22 (Springer, 1926).

[23] A. G. Every, and A. K. McCurdy, in: *Landolt-Börnstein tables*, New Series III/29, D. F. Nelson, ed., (Springer-Verlag, Berlin), pp. 1.

[24] C. Kittle, *Quantum Theory of Solids*, (John Wiley & Sons, New York, 1963).

[25] C. Kittle, *Introduction to Solid State Physics*, 6th Ed., (John Wiley & Sons, New York, 1986).

[26] J. H. van Vleck, Rev. Mod. Phys. **17**, 27 (1945).

[27] J. Hubbard, Phys. Rev. B **11**, 4584 (1979); Phys. Rev. B **19**, 2626 (1979).

[28] R. F. Sabiryanov and S. S. Jaswal, Phys. Rev. Lett. **83**, 2062 (1999).

[29] H. Wang, P.-W. Ma, and C. H. Woo, Phys. Rev. B **82**, 144304 (2010).

[30] H. Sun, J. M. D. Coey, Y. Otani, and D. P. R. Hurley, J. Phys. Condens. Matter **2**, 6465 (1990).

[31] J. van Kranendonk, and J. H. van Vleck, Rev. Mod. Phys. **30**, 1 (1958).

CHAPTER III

METHODOLOGY

Finite-temperature solid-state physical properties of ferromagnetic materials are intimately related to spin waves (magnons) and their interaction with lattice waves (phonons). Their manifestations are most clearly seen in the thermodynamics that can be expressed in terms of the free energy and other thermodynamic quantities. Statistical thermodynamics provides the tool for accessing such information via the phase space trajectories of the degrees of freedom of the ensemble of magnetic atoms. A brief introduction will be presented in Section 3.1. Spin-lattice dynamics scheme is presented in Section 3.2, for generating the phase-space trajectories of the system involving the dynamic coupled of spin and lattice degrees of freedom, as well as the temperature and stress controlling algorithms for the realization of various ensembles. Based on the phase-trajectories, the thermodynamic integration method for the free energy calculations is presented in Section 3.3. Taken together, the methodology introduced in this Chapter forms the foundation of the calculations in this thesis.

3.1 Statistical Thermodynamics

Thermodynamics (in this thesis, we consider only equilibrium or quasi-equilibrium thermodynamics) is the phenomenological theory expressing general laws governing the spontaneous transformation of one kind of energy into others, in the forms of heat and work done, the usage of which describes how the states of systems respond to changes in their environment. Statistical mechanics, on the other hand, applies the probability theory, which includes mathematical tools for dealing with large populations, to the field of mechanics, which is concerned with the motion of particles or objects when subjected to a force. It provides an interpretation of thermodynamic quantities, such as work, heat, linking the thermodynamic properties of materials with the spectroscopic data of individual molecules. The goal of statistical thermodynamics is to understand and interpret the measureable macroscopic properties of materials in terms of the properties of their constituent particles and the interactions between them.

3.1.1 Thermodynamics

Of the four laws in thermodynamics, the first- and second-law are widely used in classical thermodynamics. For an infinitesimal process, these two laws are respectively written as:

$$\mathrm{d}E = \mathrm{d}Q + \text{đ}W \tag{3.1a}$$

$$\mathrm{d}Q = T\mathrm{d}S \tag{3.1b}$$

where $\mathrm{d}E$ is the changes in internal energy of the system of interest; $\mathrm{d}Q$ is the heat absorbed by the system; $đW$ is the work done on the system; T is the absolute temperature, and $\mathrm{d}S$ is the change in entropy. Here, $đW$ is not an exact differential [1], but can be expressed in terms of generalized coordinates X and force Y in a reversible process,

$$đW = Y\mathrm{d}X \tag{3.1c}$$

If we consider a PVT system, i.e. ideal gas, the work done of the system on the surrounding is usually written as

$$đW = -P\mathrm{d}V \tag{3.1d}$$

where P is the pressure, and $\mathrm{d}V$ is the change in volume. Combining Eqs. (3.1a)-(3.1d), the first- and second-law can be written together in the form:

$$\mathrm{d}E = T\mathrm{d}S - P\mathrm{d}V \tag{3.2}$$

Eq. (3.2) is by far the most important relation in classical thermodynamics, which simply expresses a relationship among the state variables of a system and the difference between the values of these variables for two neighboring equilibrium states. Consequently, the thermodynamics state functions are derived from Eq. (3.2) to analyze the thermodynamics relationship on certain processes.

For example, the defined Helmholtz free energy F,

$$F = E - TS \tag{3.3}$$

is minimized at a equilibrium state for a system in thermal contact with a reservoir kept at constant volume. The Gibbs free energy G, on the other hand, is defined for an isothermal-isobaric process,

$$G = E - TS + PV, \tag{3.4}$$

whose decrease is equal to the maximum energy that can be used for work done.

In principle, all the thermodynamics of the system can be derived from the relation in Eq. (3.2) and its deduced relations, as long as the equation of state of the system is known. However, classical thermodynamics provides little insight into the systems. For example, the isochoric heat capacity C_V, representing the capability of heat absorbed by the system, can be derived as

$$C_V = \left(\frac{\mathrm{d}E}{\mathrm{d}T} \right)_V, \tag{3.5}$$

if the temperature dependence of internal energy at the constant volume is known, which is beyond the scope of thermodynamics.

3.1.2 Statistical thermodynamics

In statistical thermodynamics, each given macrostate can be the result of a

larger number of microstates. Under a given constraint, the equilibrium macrostate has the maximum thermodynamics probability. In this regard, all the microstates corresponding to the equilibrium macrostate are combined as a statistical ensemble, covering the whole phase-space, Ω, which is a multi-dimensional space, constructed by all degrees of freedom in a given system, $\Omega=\left(\{\boldsymbol{R}_i\},\{\boldsymbol{p}_i\},\{\boldsymbol{S}_i\}\right)$, with each particle i described by its position $\boldsymbol{R}_i$, momentum $\boldsymbol{p}_i$ and spin momentum $\boldsymbol{S}_i$. The basic idea of statistical thermodynamics is that the macroscopic quantities are the statistical ensemble averages of the corresponding microscopic quantities, as

$$\begin{aligned}\langle A\rangle &= \frac{\int_\Omega A\mathrm{d}\Omega}{\int_\Omega \mathrm{d}\Omega} \\ &= \frac{\int A(\boldsymbol{R},\boldsymbol{p},\boldsymbol{S})\rho(\boldsymbol{R},\boldsymbol{p},\boldsymbol{S})\mathrm{d}\boldsymbol{R}\mathrm{d}\boldsymbol{p}\mathrm{d}\boldsymbol{S}}{\int \rho(\boldsymbol{R},\boldsymbol{p},\boldsymbol{S})\mathrm{d}\boldsymbol{R}\mathrm{d}\boldsymbol{p}\mathrm{d}\boldsymbol{S}}\end{aligned} \tag{3.6}$$

where $\rho(\boldsymbol{R},\boldsymbol{p},\boldsymbol{S})$ is the probability of the microstates. Here, $\boldsymbol{R}\equiv\{\boldsymbol{R}_i\}$, $\boldsymbol{p}\equiv\{\boldsymbol{p}_i\}$, and $\boldsymbol{S}\equiv\{\boldsymbol{S}_i\}$. The probability ρ depends on the ensemble selected in dynamic simulations, corresponding to the thermodynamic constraints applied on the system.

In micro-canonical ensemble, where the total energy E, volume V, and the number of particles N are fixed, the probability of each microstate are identical, as $\rho(E)=1/\Omega(E)$ at an equilibrium state, where the entropy of the system is maximized,

$$S = k_{\mathrm{B}} \ln \Omega(E). \tag{3.7}$$

Since each microstate is equally probable in microcanonical ensemble, it is not easy to gain all accessible microstates for atomistic simulations. In this regard, the canonical ensemble is preferred in atomistic simulations.

In canonical ensemble, keeping the number of particles N, volume V and temperature T constant, the probability of each microstate, usually denoted by the energy level E_s instead, follows the Boltzmann distribution,

$$\rho(E_s) = \frac{e^{-\beta E_s}}{\sum_s e^{-\beta E_s}} = \frac{e^{-\beta E_s}}{Z} \tag{3.8}$$

where $\beta = 1/k_{\mathrm{B}}T$, and $Z \equiv \sum_s e^{-\beta E_s}$ is the partition function, the Laplace transformation of the total number of available microstates. Arising from the fact that the system keeps thermal contact with the heat bath, the temperature T is theoretically treated as a parameter denoting the Boltzmann distribution for a canonical ensemble. The entropy of the system can be written in terms of the probability,

$$S = -k_{\mathrm{B}} \sum_s \rho_s \ln \rho_s . \tag{3.9}$$

It should be realized that the total energy fluctuates, accompanying with the heat transportation between the system and the heat bath. In this regard, the mean energy E is treated as the internal energy in thermodynamics, which can be

derived from the partition function,

$$E = \langle E_s \rangle = \sum_s \rho_s E_s = -\frac{\partial \ln Z}{\partial \beta}, \tag{3.10}$$

and the Helmholtz free energy F,

$$F = -k_{\mathrm{B}} \ln Z . \tag{3.11}$$

Furthermore, the thermodynamic force, for instance the pressure P in the PVT system, can also be derived from the partition function,

$$P = -\sum_s \rho_s \frac{\mathrm{d}E_s}{\mathrm{d}V} = k_{\mathrm{B}} \left(\frac{\partial \ln Z}{\partial V} \right)_{T,N} \tag{3.12}$$

From the deductions above, it can be seen that the key quantity in canonical ensemble is the partition function, from which the state variables of a thermodynamic system can be derived. However, it is too difficult to obtain the exact value of partition function, since it is associated with the phase-space volume. However, based on the ergodic hypothesis that the time average is equal to the statistical ensemble average, thermodynamic quantities are calculated from the phase-space trajectories obtained by SLD simulations, the implementation of which is presented in the following section,

$$\begin{aligned}\langle A\rangle &= \frac{\int A(\boldsymbol{R},\boldsymbol{p},\boldsymbol{S})\,\rho(\boldsymbol{R},\boldsymbol{p},\boldsymbol{S})\,\mathrm{d}\boldsymbol{R}\mathrm{d}\boldsymbol{p}\mathrm{d}\boldsymbol{S}}{\int \rho(\boldsymbol{R},\boldsymbol{p},\boldsymbol{S})\,\mathrm{d}\boldsymbol{R}\mathrm{d}\boldsymbol{p}\mathrm{d}\boldsymbol{S}} \\ &= \lim_{t\to\infty}\frac{1}{t}\int_{t_0}^{t_0+t} A(\tau)\,\mathrm{d}\tau\end{aligned}. \tag{3.13}$$

It should be noted that Eq. (3.13) is available only when the system is at equilibrium state, and the probability ρ for this ensemble is stationary.

3.2 Spin-Lattice Dynamics

3.2.1 Conventional molecular dynamics

Developed in 1950s, molecular dynamics (MD) [2] is a computer simulation of physical movements of atoms and molecules, whose trajectories are determined by numerically solving the Newton's equations of motion for those interactive particles in a given ensemble [3],

$$m_i\frac{\mathrm{d}^2\boldsymbol{R}_i}{\mathrm{d}t^2} = -\frac{\mathrm{d}U}{\mathrm{d}\boldsymbol{R}_i}, \tag{3.14}$$

where the forces between the particles and potential energy are defined by molecular mechanics force field U [4].

In the early version [5,6] of MD, pair-wise interatomic potentials, e.g., Lennard-Jones potential [7], have been widely used, which is, however, used exclusively in modeling the rare gas, and is inappropriate for metals involving the many-body interaction. Consequently, embedded atom methods [8] (EAM)

were used to describe the complex atomic environment in metals, by introducing an atomic embedded potential as the function of electron density and its relevant form based on Jellium model approximation [9],

$$U_{\mathrm{EAM}} = \sum_{i=1}^{N} F\left[\rho_i\right] + \frac{1}{2}\sum_{i\neq j}^{N} V\left(\boldsymbol{R}_{ij}\right) \tag{3.15}$$

where $F\left[\rho_i\right] = -A\sqrt{\rho_i}$ is the embedded potential in terms of the electron density, $\rho_i = \sum_{j,j\neq i}^{N} f\left(\boldsymbol{R}_{ij}\right)$, as the function of interatomic distance $\boldsymbol{R}_{ij}$. For example, the EAM-type Finnis-Sinclair potential [10,11] were successfully applied to the studies of transition metals [12].

Unfortunately, the semi-empirical potentials of EAM formalism are not always useful for the study of magnetic properties in the case of ferromagnetic iron [13], since it is very difficult to separate from the total energy of interaction between atoms [14], the magnetic component due to the strong exchange interactions between the magnetic moments of neighboring atoms. Based on Stoner's model, Dudarev and Derlet (DD) constructed a many-body 'magnetic' interatomic potential [15,16] for BCC-iron, where the ferromagnetism is involved in the embedded part $F\left[\rho\right]$, expressed in terms of electron density, to describe the local magnetic structure of the environment of a given atom,

$$F\left[\rho\right] = -A\sqrt{\rho} - \frac{B}{\ln 2}\left(1-\sqrt{\frac{\rho}{\rho_C}}\right)\Theta\left(\rho_C-\rho\right), \tag{3.16}$$

where A and B are constants; $\Theta(x)$ is the Heaviside step function, with ρ_C being the critical electron density where magnetism disappears.

3.2.2. Spin-lattice dynamics scheme

In order to account for the spin dynamics and their interactions with lattice dynamics in the magnetic materials, Ma, Woo and Dudarev (MWD) developed the SLD scheme [17], where the dynamics of spin and lattice degrees of freedom are solved on the equal footing. In this regard, SLD scheme is essentially a reformulation of conventional MD to incorporate the spin degrees of freedom.

Starting from the Hamiltonian of the ferromagnetic system involving interactive spins and lattices, which have been described in detail in Chapter II, i.e.,

$$H_H = \sum_{i=1}^{N} \frac{\boldsymbol{p}_i^2}{2m_i} + U\left(\{\boldsymbol{R}_i\}\right) - \frac{1}{2}\sum_{i\neq j}^{N} J_{ij}\left(\{\boldsymbol{R}_i\}\right)\boldsymbol{S}_i \cdot \boldsymbol{S}_j , \tag{3.17}$$

Here, $\boldsymbol{p}_i$, $\boldsymbol{R}_i$, and $\boldsymbol{S}_i$ are respectively the momentum, instantaneous positions and intrinsic spin of the so-called *Heisenberg particles*, which dynamically interact via a many-body potential $U\left(\boldsymbol{R}_1,\cdots,\boldsymbol{R}_N\right) \equiv U\left(\{\boldsymbol{R}_i\}\right)$. The corresponding equations of motion for the spin and lattice degrees of freedom are derived as [17], i.e.,

$$\begin{cases} \dfrac{\mathrm{d}\boldsymbol{R}_k}{\mathrm{d}t} = \dfrac{\partial H_H}{\partial \boldsymbol{p}_k} = \dfrac{\boldsymbol{p}_k}{m_k} \\ \dfrac{\mathrm{d}\boldsymbol{p}_k}{\mathrm{d}t} = -\dfrac{\partial H_H}{\partial \boldsymbol{R}_k} = -\dfrac{\partial U}{\partial \boldsymbol{R}_k} + \dfrac{1}{2}\dfrac{\partial}{\partial \boldsymbol{R}_k}\left(\sum_{i\neq j}^{N} J_{ij}\boldsymbol{S}_i \cdot \boldsymbol{S}_j\right). \\ \hbar\dfrac{\mathrm{d}\boldsymbol{S}_k}{\mathrm{d}t} = -\left(\sum_{i\neq j}^{N} J_{ik}\boldsymbol{S}_i\right)\times \boldsymbol{S}_k = -g\mu_{\mathrm{B}}\boldsymbol{H}_k \times \boldsymbol{S}_k \end{cases} \tag{3.18}$$

The trajectories of the Heisenberg particles are numerically solved from Eq. (3.18), by simultaneously integrating the position, momentum and spin vectors over a certain discrete time-step, following Suzuki-Trotter decomposition [18] (STD) integration algorithm [19]. In general, the time-step in SLD simulation is set as 10^{-15} second, which are two orders of magnitude smaller than the typical atomic vibration cycle of 0.1 pico-second (10^{-13} s) and spin precession cycle around 0.01 pico-second (10^{-14} s), to avoid the significant discretization error [17]. In practice, the system attains thermodynamic equilibrium with the environment and maintains constant temperature and/or pressure. To realize such thermodynamic constraints, it is necessary to import the temperature and stress controlling algorithms into SLD scheme.

3.2.3 Temperature controlling algorithm

To control the temperature of the lattice and spin subsystems, the SLD adopts the Langevin thermostat based on the fluctuation-dissipation theorem, in which the Langevin equations replaces the deterministic equation (Eq. (3.18)) to account for the stochastic nature of atomic motions,

$$\frac{\mathrm{d}\boldsymbol{p}_k}{\mathrm{d}t}=m_k\frac{\mathrm{d}^2\boldsymbol{R}_k}{\mathrm{d}t^2}=-\frac{\mathrm{d}\tilde{U}}{\mathrm{d}\boldsymbol{R}_k}-\gamma\frac{\mathrm{d}\boldsymbol{R}_k}{\mathrm{d}t}+\boldsymbol{f}_k\left(t\right), \tag{3.19a}$$

$$\hbar\frac{\mathrm{d}\boldsymbol{S}_k}{\mathrm{d}t}=-g\mu_{\mathrm{B}}\left[\left(\boldsymbol{H}_k+\boldsymbol{h}_k\right)\times\boldsymbol{S}_k-\eta\left(\boldsymbol{S}_k\times\boldsymbol{H}_k\right)\times\boldsymbol{S}_k\right], \tag{3.19b}$$

where $\tilde{U}$ represents the intra-atomic potential plus the exchange interaction term; $-\gamma\frac{\mathrm{d}\boldsymbol{R}_k}{\mathrm{d}t}$ and $-\eta\left(\boldsymbol{S}_k\times\boldsymbol{H}_k\right)$ are respectively frictional forces for the lattice and damping field for spin, acting as dissipative forces due to electrons in the vicinity of the atom k. γ and η are respectively the viscosity and damping coefficient; $\boldsymbol{f}_k\left(t\right)$ and $\boldsymbol{h}_k$ are the Langevin forces for the lattice and magnetic field for spin precession, respectively, with delta-correlated relations given by,

$$\left\langle\boldsymbol{f}_k\left(t\right)\boldsymbol{f}_{k'}\left(t'\right)\right\rangle=\mu^2\delta_{kk'}\delta\left(t-t'\right), \tag{3.20a}$$

$$\left\langle\boldsymbol{h}_k\left(t\right)\boldsymbol{h}_{k'}\left(t'\right)\right\rangle=\kappa^2\delta_{kk'}\delta\left(t-t'\right), \tag{3.20b}$$

where μ and κ are the strengths of $\boldsymbol{f}_k$ and $\boldsymbol{h}_k$, respectively. According to fluctuation dissipation theorem, the $\left(\mu,\gamma\right)$ ordered pair in lattice subsystem and $\left(\kappa,\eta\right)$ ordered pair in spin subsystem should satisfy the following relationships, respectively,

$$\mu^2=6\gamma k_{\mathrm{B}}T\ , \tag{3.21a}$$

$$\left(g\mu_{\mathrm{B}}\kappa\right)^2=2\hbar S_k k_{\mathrm{B}}T\eta\ , \tag{3.21b}$$

when the system reaches the thermodynamic equilibrium state at the desired temperature T. In this regard, the dissipative and random natures of electron scattering result in the energy transformation between the system and heat reservoir, driving the whole system to Gibbs distribution labeled by the desired temperature.

3.2.4 Stress controlling algorithm

For the stress control, Berendsen barostat [20] is adopted in our SLD simulations, where the volume is scaled to modify the stress of the whole system to be the desired one. The $\alpha\beta$ component of atomic stress tensor $\sigma^i_{\alpha\beta}$ is defined following the Virial theorem [21] in SLD simulation,

$$\sigma^i_{\alpha\beta} = \frac{1}{V_i}\left(m_i v_\alpha v_\beta + \frac{1}{2}\sum_{i\neq j} f_{ij\alpha} r_{ij\beta} \right) \tag{3.22}$$

where V_i is the atomic volume; v is the velocity; $f_{ij\alpha}$ and $R_{ij\beta}$ are respectively the atomic force and separation between atoms i and j along α and β Cartesian directions. For a cubic crystal, the stress tensor is diagonal in rectangular coordinate system formed by the surface normals, which is identical to the principal coordinate system. In this case, Berendsen barostat uses a scale factor χ_α, which is a function of the normal stress $S_{\alpha\alpha} = \left\langle \sigma^i_{\alpha\alpha} \right\rangle$, to scale the lengths along α direction in the system:

$$\begin{cases} L'_\alpha = \chi_\alpha L_\alpha \\ x'_i = \chi_x x_i \\ y'_i = \chi_x y_i \\ z'_i = \chi_x z_i \end{cases}, \tag{3.23}$$

with

$$\chi_\alpha = 1 - \frac{\beta_C}{3}\frac{\Delta t}{\tau_s}\left(S^0_{\alpha\alpha} - S_{\alpha\alpha}\right) \tag{3.24}$$

where Δt is the integrator time-step; τ_s is the 'rise time' of the barostat; β_C isothermal compressibility of the system; and $S^0_{\alpha\alpha}$ is the desired value of stress. After a sufficiently long running time, the average atomic stress in the system would balance the external applied stress, gradually adjusting to the dimensions following Eq. (3.23).

3.3 Thermodynamic Integration Method

As the most fundamental of all thermodynamic functions, the free energy determines relative phase stability and derives other thermodynamic quantities, serving as a generating function. Unlike simple thermodynamic quantities such as internal energy, pressure, etc., which can be obtained from the statistical average of the corresponding micro-quantities as a function of phase trajectories generated from SLD simulations (see Eq. (3.13)), the free energy is associated with the phase-space volume itself, and cannot directly be calculated in this way. Instead, several indirect methods have been proposed to calculate the free energy,

(see review in Ref. [22]), among which thermodynamic integration (TI) method [23] is a robust approach used in atomistic simulations, and essentially the Kirkwood's [24] coupling parameter method for calculating the free energy difference, rather than the absolute free energy.

In TI method, to calculate the free energy of a system of interest H^1, one can first construct a thermodynamic path H^λ, connecting H^1 and a reference system H^0 of known free energy, i.e.

$$H^\lambda = \lambda H^1 + (1-\lambda) H^0, \tag{3.25}$$

where $\lambda \in [0,1]$ is a tunable parameter, so that $H^\lambda = H^0$ with $\lambda = 0$, and $H^\lambda = H^1$ with $\lambda = 1$. Subsequently, the free energy difference between H^1 and H^0 is calculated from an integral over the path from $\lambda = 0$ to $\lambda = 1$,

$$\Delta F = F^1 - F^0 = \int_0^1 \left\langle \frac{\partial H^\lambda}{\partial \lambda} \right\rangle_\lambda \mathrm{d}\lambda, \tag{3.26}$$

where F^1 and F^0 are the free energies of H^1 and H^0, respectively, and $\langle A \rangle_\lambda$ represents the ensemble average of operator A performed over the phase-space trajectories governed by H^λ. Since F^0 is known already, the free energy F^1 of system H^1 can be obtained finally.

In practice, a series of MD-type simulations with H^λ for each λ and the evaluation of the ensemble average are required to obtain the integrand in Eq.

(3.26). Here, the ensemble average ensures the system governed by each H^{λ} being in equilibrium. However, a dense series of points of λ is necessary to keep the accuracy for integration, and a sufficiently long simulation run is required to reduce the statistical error in ensemble average, which requires a correspondingly high computational burden.

Watanabe and Reinhardt [25] suggested an intrinsically dynamic scheme, namely the adiabatic switching approach, in which λ varies with the elapsed time t in dynamic simulation, and the integration in Eq. (3.26) is replaced by

$$\Delta F = F^1 - F^0 = \int_0^{t_s} \frac{\mathrm{d}\lambda}{\mathrm{d}t} \left(\frac{\partial H^{\lambda}}{\partial \lambda} \right)_{\lambda(t)} \mathrm{d}t \tag{3.27}$$

where t_s is the 'switching' time. If the Hamiltonian, H^{λ}, is changed slow enough compared to the natural time scale of the system, i.e. $\sim 10^{-13}$s in a typical lattice vibration, the switching process can be regarded as under quasi-equilibrium. Accordingly, the functional form of $\lambda(t)$ determines the numerical stability of this scheme. A more detailed discussion of the approach, including analysis of errors, can be found in the authoritative book by Frenkel and Smit [26]. In this thesis, $\lambda(t)$ is set as the form as in Ref. [27],

$$\lambda(\tau) = \tau^5 \left(70\tau^4 - 315\tau^3 + 540\tau^2 - 420\tau + 126 \right) \tag{3.28}$$

where τ is the scaled time as $\tau = t / t_s$, so that $\lambda = 0$ at $t = 0$, and $\lambda = 1$ at $t = t_s$.

It should be noted that the thermodynamic path is not limited to be a physical path that can be followed in experiments. In addition, all the parameters in the Hamiltonian can be used as thermodynamic variables to construct a thermodynamic path for particular purposes. For instance, the Hamiltonian itself is treated as the thermodynamic variable in Eq. (3.25). In the thermodynamics points of view, the free energy is equal to the work done for an isothermal reversible process, i.e. λ and $\left\langle \frac{\partial H^{\lambda}}{\partial \lambda} \right\rangle_{\lambda}$ in Eq. (3.26) respectively correspond to the generalized coordinate X and force Y in the definition of work done in Eq. (3.1c), which shows the subtle relation between the thermodynamics and mechanics.

Reference

[1] A. H. Carter, *Classical and Statistical Thermodynamics*, (Prentice-Hall, Inc., New Jersey, 2001), pp. 37-40.

[2] B. J. Alder, and T. E. Wainwright, J. Chem. Phys. **27**, 1208 (1957).

[3] M. P. Allen and D. J. Tildesley, *Computer Simulation of Liquids*, (Oxford University Press, 1987).

[4] J. M. Haile, *Molecular Dynamics Simulation: Elementary Methods*, (John Wiley & Sons, Inc. New York, 1992).

[5] B. J. Alder, and T. E. Wainwright, J. Chem. Phys. **27**, 1208 (1957).

[6] A. Rahman, Phys. Rev. **136**, A405 (1964).

[7] J. E. Lennard-Jones, Proc. Roy. Soc. London, **106A**, 441 (1924); Proc. Roy. Soc. London, **106A**, 463 (1924).

[8] M. S. Daw, and M. I. Baskes, Phys. Rev. Lett. **50**, 1285 (1983); Phys. Rev. B 29, 6443 (1984).

[9] J. P. Perdew, E. R. McMullen, A. Zunger, Phys. Rev. A **23**, 2785 (1981).

[10] M. W. Finnis, J. E. Sinclair, Philos. Mag. A **50**, 45 (1984).

[11] M. W. Finnis, *Interatomic Forces in Condensed Matter,* (Oxford University Press, New York, 2003).

[12] P. M. Derlet, D. Nguyen-Manh, and S. L. Dudarev, Phys. Rev. B **76**, 054107 (2007).

[13] G. J. Ackland, D. J. Bacon, A. F. Calder, and T. Harry, Philos. Mag. A **75**, 713 (1997).

[14] M. I. Mendelev, S. Han, D. J. Srolovitz, G. J. Ackland, D. Y. Sun, and M. Asta, Philos. Mag. **83**, 3977 (2003).

[15] S. L. Dudarev, and P. M. Derlet, J. Phys.: Condens. Matter **17**, 7097 (2005).

[16] P. M. Derlet, and S. L. Dudarev, Prog. Mater. Sci. **52**, 299 (2007).

[17] P.-W. Ma, C. H. Woo, and S. L. Dudarev, Phys. Rev. B **78**, 024434 (2008).

[18] N. Hatano, and M. Suzuki, Lect. Notes Phys. **679**, 37 (2005).

[19] P.-W. Ma, and C. H. Woo, Phys. Rev. E **79**, 046703 (2009).

[20] H. J. C. Berendsen, J. P. M. Postma, W. F. Van Gunsteren, A. Di Nola and J. R. Haak, J. Chem. Phys. **81**, 3684 (1984).

[21] H. Goldstein, *Classical Mechanics*, 2nd ed., (Addison-Wesley, Reading, MA, 1980), pp. 82-84.

[22] D. Frenkel, In *Computer Simulation in Materials Science*, ed. By M. Meyer, V. Pontikis, (Dordrecht: Kluwer, 1991), pp. 85.

[23] D. Frenkel, and A. J. C. Ladd, J. Chem. Phys. **81**, 3188 (1984).

[24] J. G. Kirkwood, J. Chem. Phys. **3**, 300 (1935).

[25] M. Watanabe, and W. P. Reinhardt, Phys. Rev. Lett. **65**, 3301 (1990).

[26] D. Frenkel and B. Smit, *Understanding Molecular Dynamics: From Algorithms to Applications*, (Academic, London, 2002), Part III, pp. 165-288.

[27] M. de Koning, and A. Antonelli, Phys. Rev. E **53**, 465 (1996).

CHAPTER IV

PHONON AND MAGNON SPECTRA

In this Chapter, the phonon and magnon dispersion spectra, the spectral line broadening and the corresponding lifetimes of BCC iron are calculated over a wide temperature range. Anharmonic effects and phonon-magnon interaction are fully accounted for. Both spectra are found to soften with increasing temperature, especially near the Brillouin zone boundary. Line broadening for both spectra is also found to increases with increasing temperature, which can be traced to anharmonicity of the lattice and spin vibrations, as well as the phonon-magnon interaction. Interaction with magnons does not affect the phonon frequencies very much, but line broadening is significantly enhanced, resulting in substantial reduction in the phonon lifetime. Significant magnon softening and line broadening (lifetime reduction) due to interaction with phonons is seen. Softening leads to the lowering of the Curie temperature, from ~1100K to ~1000K. At the same time, the spin stiffness is also substantially reduced near the Curie temperature.

4.1 Chapter Introduction

Phonons and magnons are respectively elementary excitations of a ferromagnetic crystal in the form of vibrations of the lattice and the spins. They are the origins of temperature dependence of materials properties involving the crystal lattice or the spin, which include all thermal, magnetic, mechanical and properties arising from their coupling [1], such as phase transformation, electrical resistance, magnetostriction, etc. Typical examples are the complex temperature dependencies of such fundamental material properties as electric and thermal conductance, expansivity, heat capacity, elastic moduli, particularly near the FM/PM phase transition point [2,3]. In this regard, a clear understanding of the vibrational thermodynamics [4] associated with the lattice and spin waves (phonons and magnons) is of paramount importance in the materials properties of ferromagnetic materials.

Current knowledge of vibrational thermodynamics is mostly derived from the statistical mechanics of a harmonic lattice [5], which, strictly speaking, is restricted only to non-magnetic materials and at low temperatures. Within the harmonic approximation, phonons and magnons in magnetic materials are non-interacting, and the contributions of lattice and spin vibrations to thermodynamics of the ferromagnetic crystal can be added linearly. However, at high temperatures, particularly near the magnetic transition points, anharmonicity

is so important that the effects of phonons and magnons are not simply additive, which presents a much bigger challenge.

To further elaborate, we begin with the simplest case of non-magnetic metals at low temperatures, where there are no magnons and the phonon density is so low that phonons are practically free (non-interacting). Their spectral frequencies are well-defined and the corresponding lifetimes practically infinite, as measured by the reciprocal of the power spectral density broadening. As temperature increases, so does the phonon density and the probability of their mutual interaction. This interaction has its origin in the anharmonicity of the restoring forces that the vibrating atoms experience at these temperatures due to the increasing amplitude. Multi-phonon scattering shifts the characteristic phonon frequencies, which at the same time becomes less well-defined (broadened) due to the admixture of nearby phonon states resulting from the anharmonic perturbation [6]. In the quasi-harmonic temperature range, most of the phonon frequency shift (but not the line broadening) is caused by the change in the equilibrium mean atomic volume arising from the multi-phonon scattering. At higher temperatures, the influence of other contributions becomes important [5]. This is particularly true near phase transition points where serious phonon softening occurs. The change of phonon states with temperature is the fundamental reason for the temperature dependence of thermodynamic state functions involving the crystal lattice and hence all physical properties associated

with it. Indeed, using a damped harmonic oscillator model, the characteristic frequency shift can be shown to be given by [5],

$$\omega(\boldsymbol{q}) = \omega_0(\boldsymbol{q}) + \Delta\omega(\boldsymbol{q}) - \mathrm{i}\Gamma(\boldsymbol{q}) \tag{4.1}$$

where $\omega(\boldsymbol{q})$ is the characteristic frequency of phonon involving anharmonic effect, whereas $\omega_0(\boldsymbol{q})$ is the harmonic frequency, and $\Delta\omega(\boldsymbol{q})$ is the corresponding frequency shift, and $\Gamma(\boldsymbol{q})$ is the broadening.

In ferromagnetic materials, the thermal energy is shared between phonons (lattice waves) and magnons (spin waves). The thermodynamics of these materials must take into account contributions from the phonons, magnons and their coupling. The coupling introduces into the phonon and magnon thermodynamics additional anharmonic effects, resulting in a host of so-called magnetic anomalous phenomena [7,8], such as magnetostriction, invar effects, large temperature sensitivity near the FM/PM transition in the heat capacity, thermal conductivity, and elastic moduli, etc.

We note that although the dynamics of the lattice and the spins are coupled via the same exchange field in the Heisenberg Hamiltonian, effects of the coupling on the phonons and magnons could be different, such as in their strength and temperature dependence. Thus, the softening of magnons and the decrease of their lifetimes in BCC iron due to the FM/PM transition, which have

been observed in numerous neutron scattering experiments, does not necessarily happen with the phonons.

Due to the difficulty in treating the dynamically coupled lattice and spin vibrations, various approximations have been adopted to calculate its effects on the lattice and magnetic properties. Typically, effects of the coupling on lattice properties are studied at temperatures far away from the magnetic transition point, where effects on the atomic force constants due to the deviation from perfect alignment of the spins can be treated within the frozen magnon scheme [9]. Effects of the coupling have been studied by Akhiezer [10] by introducing into the exchange integral small dipolar terms in the power series expansion of the ionic displacement. Based on this interaction Hamiltonian, Yakovlev [11] calculated the damping of spin waves due to the phonons. Later on, Elliott and Stern [12] studied various interactions that contribute to the line widths of the spin wave and phonon spectra. It should be noted that these calculations are also restricted to the low temperature regime. In this temperature regime, atomistic simulations based on *ab initio* density functional theory (DFT) are also widely used to obtain information of the spin system, such as the spin configuration at ground state [13,14], and magnon spectra [15,16], etc., by adiabatically separating the magnetic interaction from the coupled spin and lattice systems. By using the LMTO method, Halilov *et al.* [17] and Savrasov [18] calculated the magnon spectrum of iron based on the frozen-magnon approximation. However,

the dynamic influence of lattice vibrations on the magnon excitations is neglected. In this regard, Sabiryanov *et al.* [19] suggested the frozen-magnon frozen-phonon scheme, where lattice vibrations are treated under harmonic approximation. In addition, Bergman *et al.* [20] combined first-principle calculations with atomistic spin dynamics simulations and concluded that the change in exchange interaction strength was responsible for the softening of magnon. Yet these calculations are based on the assumption that the dynamics of the spin and lattice vibrations can be treated independently and simply added, which is questionable at high temperatures near the FM/PM phase boundary, where non-linear effects becomes apparent.

In this Chapter, large scale spin-lattice dynamics (SLD) [21] simulations are performed to obtain the dispersion curves of both phonons and magnons, and their lifetimes over a wide temperature regime including the FM/PM transition point. Comparison with separate spin dynamics (SD) and molecular dynamics (MD) calculations are also performed to evaluate the effects of phonon-magnon coupling on the phonon and magnon excitations.

4.2 Simulation Scheme

The Dudarev-Derlet (DD) potential [22] $U_{\mathrm{DD}}\left(\boldsymbol{R}\right)$ is used to describe the ground-state intra-atomic interactions, in which the atomic spins are collinear. In terms of U_{DD}, $U\left(\boldsymbol{R}\right)$ in Eq. (2.17) is given by

$$U(\boldsymbol{R}) = U_{\mathrm{DD}}(\boldsymbol{R}) - \left\{ -\frac{1}{2}\sum_{i\neq j}^{N} j_{ij}(\boldsymbol{R}) \right\} \tag{4.2}$$

where $j_{ij}(\boldsymbol{R}) \equiv J_{ij}(\boldsymbol{R}) S_i S_j$, in which $J_{ij}(\boldsymbol{R})$ is the exchange field. Substituting Eq. (4.2) into the Hamiltonians H_H and H_L for the SLD scheme in Eqs. (2.27) & (2.28), we may write

$$H_H = \sum_{i=1}^{N} \frac{\boldsymbol{p}_i^2}{2m_i} + U_{DD}(\boldsymbol{R}) + \frac{1}{2}\sum_{i\neq j}^{N} j_{ij}(\boldsymbol{R})\left(1 - \boldsymbol{e}_i \cdot \boldsymbol{e}_j\right) \tag{4.3a}$$

$$H_L = \sum_{i=1}^{N} \frac{\boldsymbol{p}_i^2}{2m_i} + U_{DD}(\boldsymbol{R}) + \frac{1}{2}\sum_{i\neq j}^{N} j_{ij}(\boldsymbol{R}) \tag{4.3b}$$

where $\boldsymbol{e}_i$ is the unit vector representing the spin-direction of atom i. It is obvious that the potential in Eq. (4.3a) reduces to the DD potential, because the spin system is collinear at 0K. Here, the exchange integral $j_{ij}(\boldsymbol{R})$ has the form given in Ref [21], obtained by best fitting of the data from *ab initio* calculations:

$$j_{ij}(\boldsymbol{R}) = j_0\left(1 - \boldsymbol{R}_{ij} / \boldsymbol{R}_c\right)^3 \Theta\left(\boldsymbol{R}_c - \boldsymbol{R}_{ij}\right) \tag{4.4}$$

where j_0 is the fitting parameter, and $\boldsymbol{R}_c = 3.75\text{Å}$ is the cut-off radius, located between the second and the third nearest neighbor distance in BCC iron, $\Theta(x)$ is the Heaviside step function. H_L is the lattice Hamiltonian that describes the lattice dynamics in the absence of spins. The corresponding Heisenberg Hamiltonian used for the spin dynamics in the absence of lattice vibrations is given by

$$H_S = -\frac{1}{2}\sum_{i\neq j}^{N} j_{ij}\boldsymbol{e}_i \cdot \boldsymbol{e}_j \,. \tag{4.5}$$

The simulation cell contains 20 BCC unit cells along each dimension in Cartesian coordinate system with 16000 atoms. Periodic boundary conditions are applied to avoid surface effects. Simulation of the canonical ensemble is carried out with Langevin thermostat [21,23] to keep the system at a prescribed temperature. The atomic volume is taken as the temperature dependent equilibrium one in SLD simulations, whereas in SD simulations the lattice parameter is fixed as the one at ground state, i.e. $a = 2.8665\text{Å}$ [22] in DD potential at 0K. The computation is performed using the Suzuki-Trotter decomposition [24] with a time step of 1 femto-second (fs, 10^{-15} s). At least 2 nano-seconds (ns, 10^{-9} s) of equilibrium are maintained to allow for the critical slowing down [25] of the spin subsystem near Curie temperature. After sufficient equilibration, the spin and lattice phase-space trajectories are obtained for H_H, H_L and H_S, from which the corresponding dispersion curves of phonon and magnon excitations are calculated for various temperatures.

According to the Nyquist-Shannon theorem [26], the length of sampling time t determines the resolution of the spectra of waves, whereas the sample time-interval Δt determines the maximum frequency. Accordingly, $t = 65\text{ps}$ ($1\text{ps}=10^{-12}\text{s}$) and $\Delta t = 1\text{fs}$ are set in the current calculations, thus $\Delta\omega = 2\pi / t \approx 0.10\text{THz}$ and $\omega_{\max} = 2\pi / \Delta t \approx 3140\text{THz}$.

4.3 Calculations of Power Spectra Density

In this chapter, the superscript *p* denotes phonons, and superscript *m* denotes magnons. In an isotropic periodic crystal, the instantaneous atomic velocities can be represented by superposition of all the available phonon modes $\omega^p(\boldsymbol{q},s)$, denoted by wave vector $\boldsymbol{q}$ and polarization s in real space [27],

$$\boldsymbol{v}_{j,s}(t)=\sum_{\boldsymbol{q}}\left\{\boldsymbol{v}_{\boldsymbol{q},s}(t)\cos\left(\boldsymbol{q}\cdot\boldsymbol{R}_j\right)+\boldsymbol{v}_{-\boldsymbol{q},s}(t)\sin\left(-\boldsymbol{q}\cdot\boldsymbol{R}_j\right)\right\} \tag{4.6}$$

where $\boldsymbol{v}_{j,s}$ is the projection of the velocity of atom j on the direction of the corresponding polarization vector, and $\boldsymbol{R}_j$ is its position; $\boldsymbol{v}_{\boldsymbol{q},s}(t)$ and $\boldsymbol{v}_{-\boldsymbol{q},s}(t)$ represent the lattice waves propagating in the positive and negative direction, respectively. If we apply an inverse rotational Fourier transform over the space domain onto both sides of Eq. (4.6), the wave-form of $\boldsymbol{v}_{\boldsymbol{q},s}(t)$ and $\boldsymbol{v}_{-\boldsymbol{q},s}(t)$ in the reciprocal space can be obtained,

$$\boldsymbol{v}_{\boldsymbol{q},s}(t)=\frac{1}{N}\sum_{j=1}^{N}\boldsymbol{v}_{j,s}(t)\left\{\cos\left(\boldsymbol{q}\cdot\boldsymbol{R}_j\right)+\sin\left(\boldsymbol{q}\cdot\boldsymbol{R}_j\right)\right\} \tag{4.7a}$$

$$\boldsymbol{v}_{-\boldsymbol{q},s}(t)=\frac{1}{N}\sum_{j=1}^{N}\boldsymbol{v}_{j,s}(t)\left\{\cos\left(\boldsymbol{q}\cdot\boldsymbol{R}_j\right)-\sin\left(\boldsymbol{q}\cdot\boldsymbol{R}_j\right)\right\} \tag{4.7b}$$

Following the Wiener-Khintchin theorem [28], the power spectra density $\Phi^p(\boldsymbol{q}_s,\omega)$ of phonon with specific wave-vector can be obtained from the Fourier transformation of the time-correlation function $C^p(\boldsymbol{q}_s,t)$ of $\boldsymbol{v}_{\pm\boldsymbol{q},s}(t)$ [29,30],

$$C^p\left(\boldsymbol{q}_s,t\right)=\frac{\left\langle v_{q,s}\left(t\right)v_{q,s}\left(0\right)\right\rangle}{\sum_s\left\langle v_{q,s}\left(0\right)v_{q,s}\left(0\right)\right\rangle}, \tag{4.8}$$

according to

$$\begin{aligned}\Phi^p\left(\boldsymbol{q}_s,\omega\right)&=\int C^p\left(\boldsymbol{q}_s,t\right)e^{-\mathrm{i}\omega t}\mathrm{d}t\\&=\int\left|v_{q,s}\right|^2e^{-\mathrm{i}\omega_{q,s}^p\cdot t}e^{-\mathrm{i}\omega t}\mathrm{d}t\,.\\&=\left|v_{q,s}\right|^2\delta\left(\omega-\omega_{q,s}^p\right)\end{aligned} \tag{4.9}$$

From Eq. (4.9), the phonon mode frequency $\omega_{\pm\boldsymbol{q},s}^p$ with a specific wave vector and polarization direction can be found from the location of peaks in $\Phi^p\left(\boldsymbol{q}_s,\omega\right)$, which gives the phonon dispersion relation. Here, for an isotropic crystal, the frequency of phonon mode is the scalar function of wave-vector, and is independent of the direction, that is $\omega_{+\boldsymbol{q},s}^p=\omega_{-\boldsymbol{q},s}^p$. The atomic velocity is preferred for calculating the phonon modes, since the time-series of $\boldsymbol{v}_{j,s}\left(t\right)$ is a wide-sense stationary random process [31] under equilibrium.

Similar to phonons, the magnon power spectra density $\Phi^m\left(\boldsymbol{q},\omega\right)$ of a specific wave-vector $\boldsymbol{q}$ in the reciprocal space can also be obtained from the corresponding Fourier transform of the time-correlation function $C^\alpha\left(\boldsymbol{q},t\right)$ of the spin wave $S_q^\alpha\left(t\right)$ (α = x or y) [32],

$$\begin{aligned}\Phi^m\left(\boldsymbol{q},\omega\right)&=\int C^\alpha\left(\boldsymbol{q},t\right)e^{\mathrm{i}\omega t}\mathrm{d}t\\&=\int\left|S_q^\alpha\right|^2e^{-\mathrm{i}\omega_q^m\cdot t}e^{\mathrm{i}\omega t}\mathrm{d}t\,,\\&=\left|S_q^\alpha\right|^2\delta\left(\omega-\omega_q^m\right)\end{aligned} \tag{4.10}$$

with

$$S_q^\alpha(t) = \sum_{j=1}^{N} S_j^\alpha(t) e^{-i\mathbf{q}\cdot\mathbf{R}_j(t)}, \tag{4.11}$$

and

$$C^\alpha(\boldsymbol{q},t) = \left\langle S_q^\alpha(t) S_q^\alpha(0)\right\rangle - \left\langle S_q^\alpha(t)\right\rangle\left\langle S_q^\alpha(0)\right\rangle. \tag{4.12}$$

Therefore, the magnon dispersion relation $\omega = \omega^m(\boldsymbol{q})$ is obtained by locating the peaks of $\Phi^m(\boldsymbol{q},\omega)$, like in Eq. (4.9). Since the longitudinal fluctuations of the spin moments are neglected in the conventional Heisenberg model [33] (See Eq. (2.29)), only two degenerate branches of transverse spin waves are left, without the longitudinal branch, corresponding to two degrees of freedom of the spin subsystem.

Figs. 4.1 show examples of $\boldsymbol{v}_{\boldsymbol{q}}(t)$ of longitudinal lattice wave and $\boldsymbol{S}_{\boldsymbol{q}}^\alpha(t)$ of spin wave for a given wave vector $\boldsymbol{q}$ along the $[100]$ direction with value $q = 0.1q_{\max}$, where $q_{\max} = 2\pi/a$ and a is the equilibrium lattice parameter at a given temperature under stress-free condition. The vibration frequencies of the spin waves, i.e. the corresponding magnon energy, can be seen to be much higher than those of the lattice waves, i.e. the corresponding phonon energies, at temperatures far from T_C, e.g. 300K. The frequencies of the spin waves decrease with increasing temperature. The general wave form is not purely sinusoidal. At temperatures below the FM/PM transition, it has beats indicating superposition

of a spread of frequencies. Above the FM/PM phase boundary, e.g., 1100K the corresponding correlation function shown in Fig. 4.2(e) reveals that the wave pattern of $\boldsymbol{S}_{\boldsymbol{q}}^{\alpha}(t)$ at 1100K is like a damped wave.

Plotted in Figs. 4.3 are the Fourier transforms of the autocorrelation functions of Figs. 4.2 (Eqs. (4.7) & (4.11)). They are the corresponding power spectral densities, shown in Eqs. (4.8) & (4.9), where the peaks indicate the characteristic frequencies of phonons or magnons of wave-vector $\boldsymbol{q}$. The broadening of the power spectra, indicated by the so-called *full width at half maximum* (FWHM), translates into the width of the corresponding spectral line, which is related to the phonon or magnon life times. In general, shown in Figs. 4.3, the power spectra density of both phonon and magnon can be fitted by Lorentzian function [34],

$$\Phi(q,\omega)=\frac{I_{\boldsymbol{q}}}{1+\dfrac{\left(\omega-\omega_{\boldsymbol{q}}\right)^2}{\Gamma_{\boldsymbol{q}}^2}}, \tag{4.13}$$

where $\omega_{\boldsymbol{q}}$ is the characteristic frequency of phonon or magnon, and $\Gamma_{\boldsymbol{q}}$ is the broadening, with $I_{\boldsymbol{q}}$ being the intensity of the power spectra density. The lifetime of the thermal excitations τ can be obtained as the reciprocal of the corresponding broadening of its power spectra density, i.e. $\tau=(2\Gamma)^{-1}$.

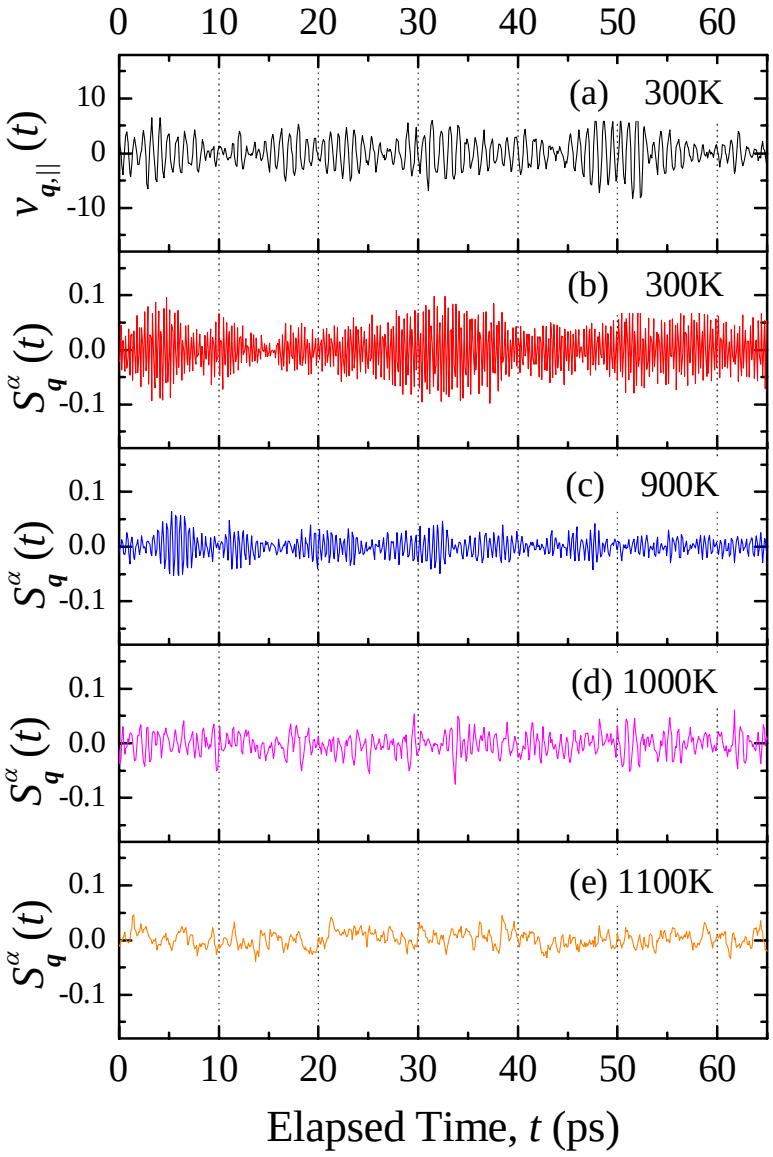

Fig. 4.1: Amplitudes of (a) longitudinal lattice wave at 300K (black) and spin waves at (b) 300K (red), (c) 900K (blue), (d) 1000K (magenta) and (e) 1100K (orange) with $q = 0.1q_{max}$ along [100] direction, where $q_{max} = 2\pi/a$ and a is the equilibrium lattice parameter at the given temperature under stress-free condition, obtained from SLD simulations. The vibrational frequencies of spin waves are much higher than that of lattice wave at the temperature far from the FM/PM transition point, e.g. 300K.

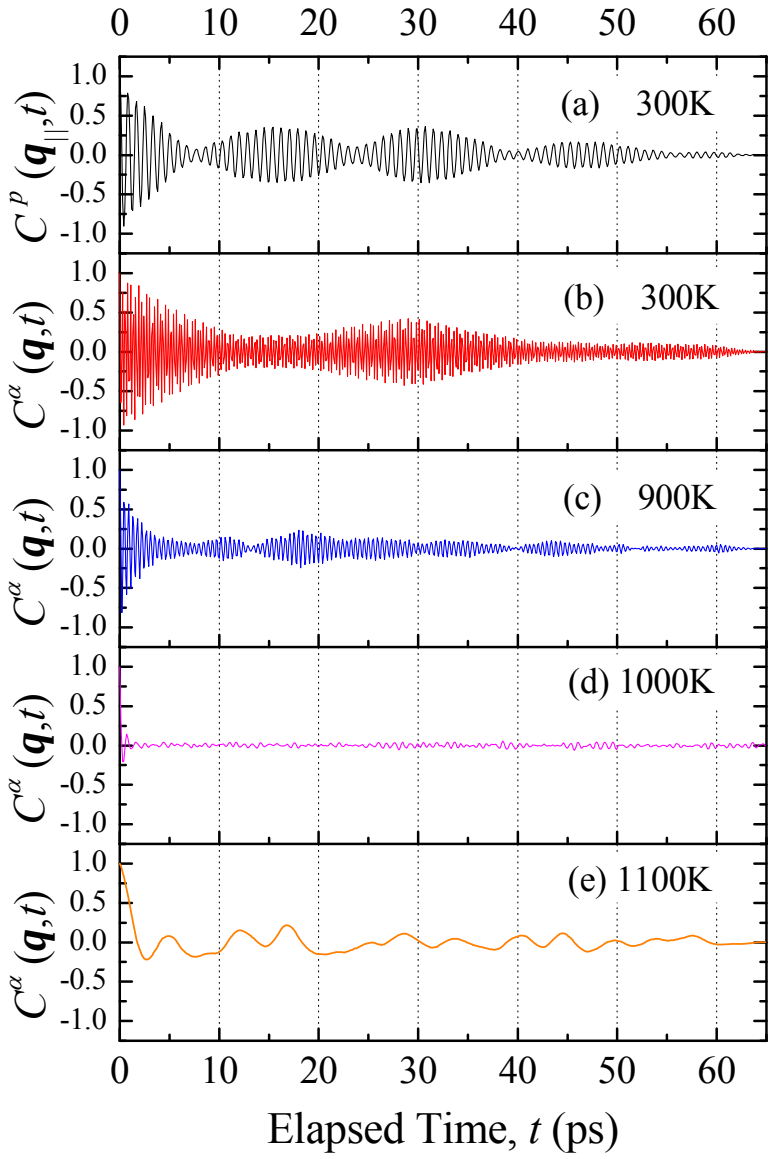

Fig. 4.2: The autocorrelation functions of the corresponding waves plotted in Fig. 4.1, obtained from SLD simulations, (a) longitudinal lattice wave at 300K (black) and the spin waves at (b) 300K (red), (c) 900K (blue), (d) 1000K (magenta), and (e) 1100K (orange). The general wave forms are not purely sinusoidal, indicating superposition of a spread of frequencies. Whereas, the autocorrelation function of 1100K reveals the wave pattern is like a damped wave.

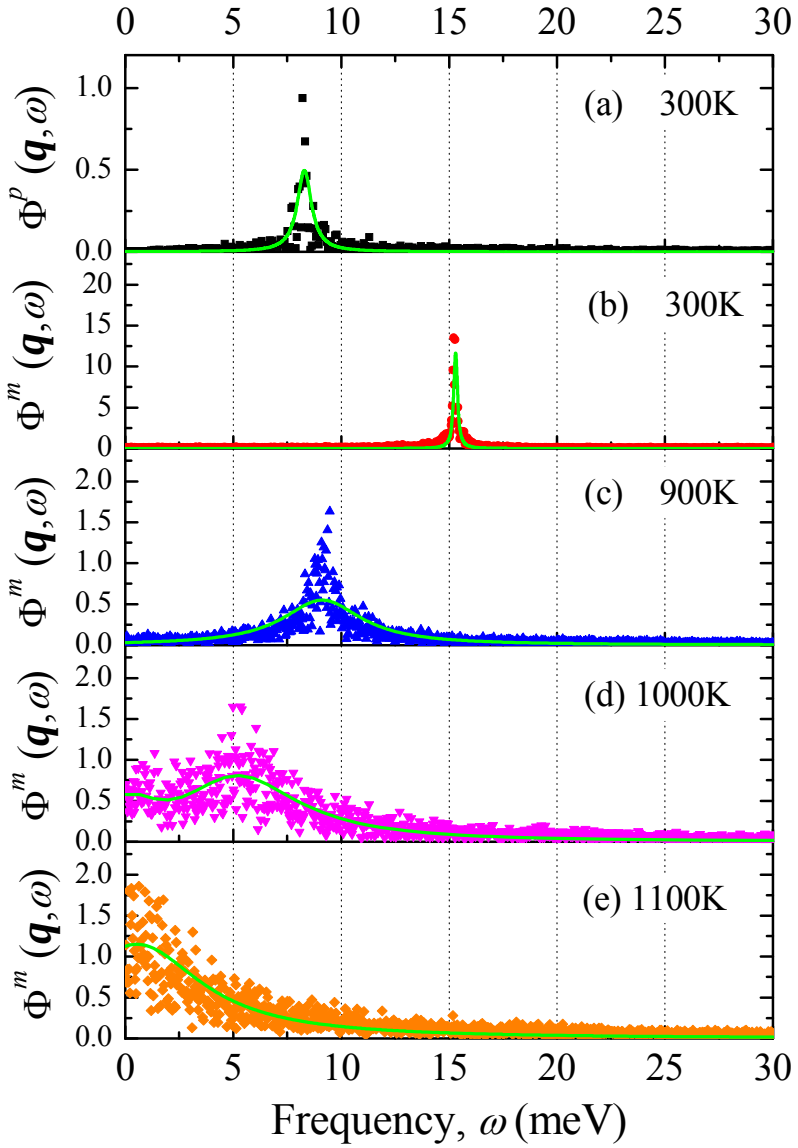

Fig. 4.3: The power spectra of the corresponding waves shown in Fig. 4.1: (a) longitudinal lattice wave at 300K (black square), spin waves at (b) 300K (red circle), (c) 900K (blue upward triangle), (d) 1000K (magenta downward triangle), and (e) 1100K (orange diamond), obtained from SLD simulations. Green solid lines are the corresponding Lorentzian fitting. The location of peaks corresponds to the characteristic frequencies of the specific waves, whereas the full-width at half maximum (FWHM) are related to the lifetimes.

In Figs. 4.3, the characteristic frequencies of spin waves can be seen to decrease with increasing temperature, indicating the softening of the magnons. Line broadening, on the other hand, increases with temperature, due to anharmonic effects caused by the increasing amplitudes of the thermal fluctuations. However, near the Curie temperature at 1100K, the spin wave stops to show a clear peak, due to vanishing long-range magnetic order.

It should be noted that, in Fig. 4.3(d), Φ^m at 1000K shows a peak centered at 0meV, which has also been observed in neutron scattering experiments [35], and other calculations [36]. Such a central peak is associated with the zero energy transfer among magnons with short wave-length or at high temperatures, which can be fitted by Gaussian-type curve as suggested in Ref. [34] as

$$G = I_c \exp\left(-\omega^2 / \Gamma_c^2\right), \tag{4.14}$$

where I_c and Γ_c are the intensity and broadening. Therefore, Φ^m of 1000K, as shown in Fig. 4.4, can be fitted as

$$\Phi = G + L = I_c \exp\left(-\omega^2 / \Gamma_c^2\right) + \frac{I_0}{1 + \frac{\left(\omega - \omega_0\right)^2}{\Gamma^2}}. \tag{4.15}$$

Since the central peak is not related to the dispersion relation of magnons, we will not show such a fitting in the following, for example, the magnon power spectra density at 1100K in Fig. 4.3(e).

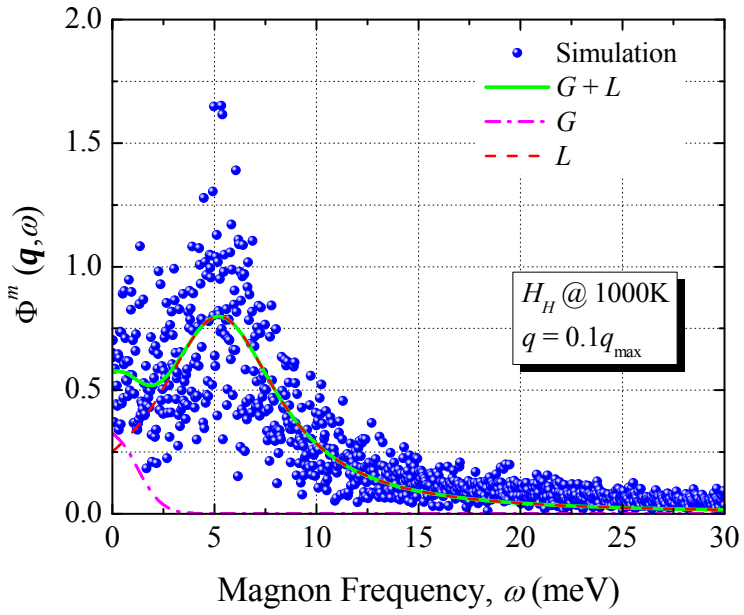

Fig. 4.4: The illustration of zero energy transfer central peak at high temperature, i.e. 1000K, of the magnon spectral density. Green solid line represents the fitting curves, which consists of Gaussian fitting (magenta dashed dot) and Lorentzian fitting (red dashed).

Repeating the forgoing procedures for each $\boldsymbol{q}$, the dispersion curves and spectral line broadening, as well as the lifetime, of both phonons and magnons can be obtained. It will be further discussed in the following.

4.4 Power Spectra Density of Phonons

Figs. 4.5 shows the spectra densities of longitudinal phonons along [100] direction at various temperatures for $q/q_{\max}$=0.1, 0.5 and 0.9 for H_H and H_L, i.e., with and without phonon-magnon interaction. The characteristic frequencies ω^p and broadening Γ^p are obtained by fitting to the Lorentzian function (Eq.

(4.12)). The results are listed in Table 4.1. It can be seen that both ω^p and Γ^p are increasing functions of wave-vector $\boldsymbol{q}$. In addition, the phonon frequency ω^p shifts lower as temperature increases, for example, from 8.45meV at 300K to 7.22meV at 900K for the phonons of $q/q_{\max}=0.1$ for H_L, from which the anharmonic nature of the crystal potential is apparent. However, the frequency shift becomes less significant at high temperatures. This is likely due to the inaccuracy of the DD potential used in the current calculations, which does not produce the BCC to FCC structural phase transition of iron at 1183K [22]. Meanwhile, the anharmonicity causes the broadening of power spectra density, as shown in Eq. (4.1). In Figs. 4.5, Γ^p increases with temperature, i.e. from 0.31meV at 300K to 1.05meV at 1100K for the phonons with $q/q_{\max}=0.1$, showing the increasing importance of the multi-phonon interaction due to the increasing density of phonons at higher temperatures.

The same behavior discussed in the foregoing can also be seen in the results for H_H, i.e. with phonon-magnon coupling. As shown in Figs. 4.6, the coupling produces extra phonon scattering, which results in a larger broadening of power spectra density of phonons with large wave-vectors at high temperatures. For instance, the broadening increases from 0.31meV to 0.39meV for the phonons with $q/q_{\max}=0.1$ at 300K, and from 3.74meV to 5.72meV for the phonon with $q/q_{\max}=0.9$ at 1100K, with almost 50% increase. Consequently, the phonon lifetime (at $q/q_{\max}=0.1$) of ~1ps at 300K is reduced an order of magnitude to

100fs at 1100K. In addition, the larger the wave-vector, the shorter is the lifetime of phonons. Despite the strong influence on the phonon-life time, phonon-magnon interaction does not seem to have a strong effect on the phonon frequency shift, as shown by comparing the values of ω^p in Table 4.1. This may be the result of cancelation between the quasi-harmonic effects with other anharmonic effects.

TABLE 4.1: Longitudinal phonon frequency, broadening and lifetime along [100] direction in BCC iron, without (H_L) and with (H_H) the phonon-magnon interaction.

$q/q_{\max}$		$T=300$K		900K		1000K		1100K	
		H_L	H_H	H_L	H_H	H_L	H_H	H_L	H_H
ω^p (meV)	**0.1**	8.45	8.10	7.22	7.23	7.20	7.20	7.20	7.02
	0.5	31.6	30.6	28.0	28.0	27.7	27.6	27.7	27.5
	0.9	32.9	32.8	30.6	30.6	30.5	30.4	30.5	30.4
Γ^p (meV)	**0.1**	0.31	0.39	0.66	0.95	1.05	1.18	1.05	1.19
	0.5	0.54	1.01	2.26	3.55	2.91	4.22	4.18	5.87
	0.9	1.36	1.56	3.24	4.56	3.43	5.14	3.74	5.72
τ^p (fs)	**0.1**	1062	843.9	498.6	346.4	313.4	278.9	313.4	276.6
	0.5	609.5	325.8	145.6	92.71	113.1	77.99	78.73	56.07
	0.9	242.0	211.0	101.6	72.17	95.95	64.03	88.00	57.54

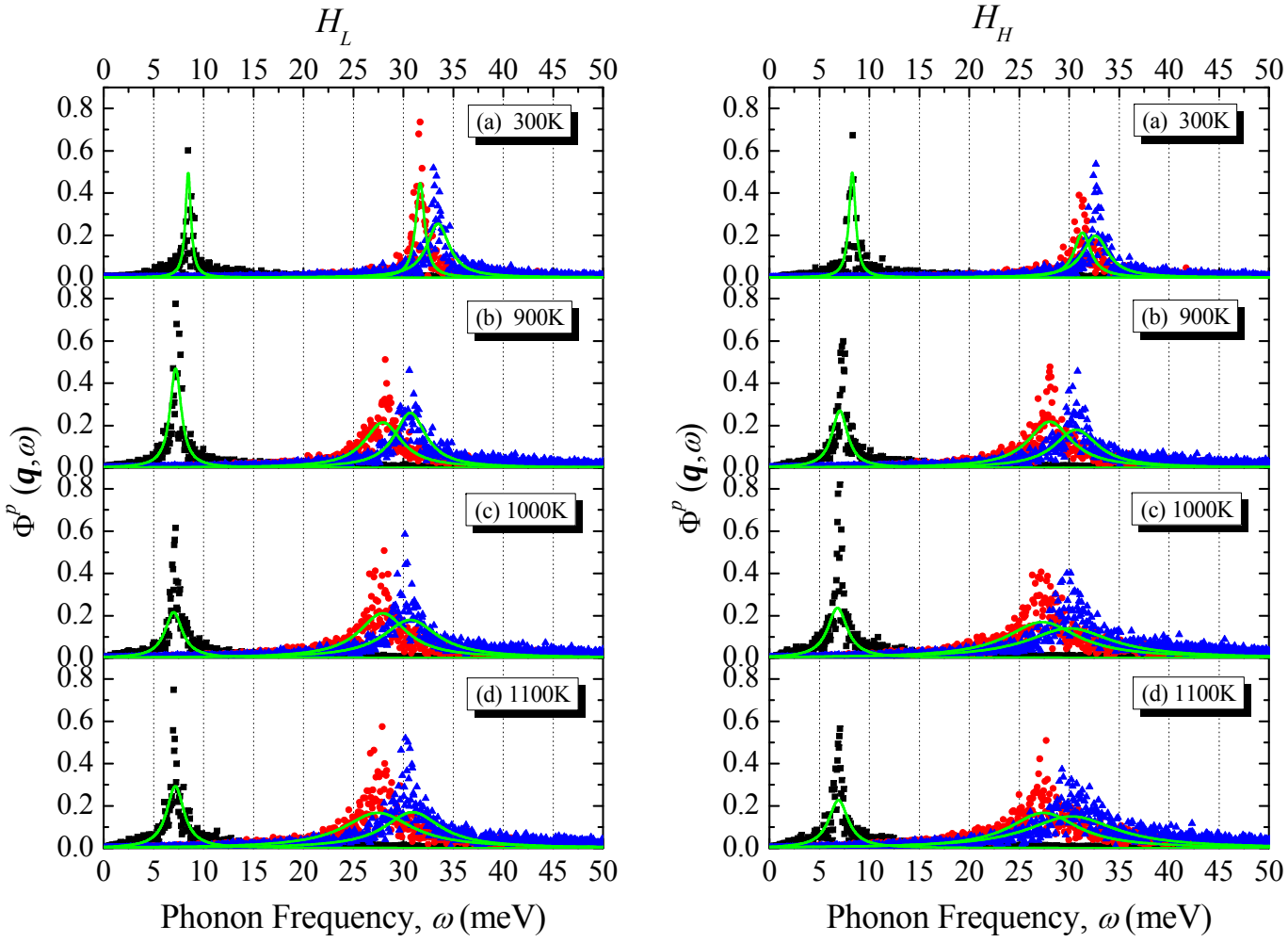

Fig. 4.5: The power spectral density of longitudinal phonons with q/q_{max} = 0.1 (black square), 0.5 (red circle), 0.9 (blue triangle) along [100] direction at (a) 300K, (b) 900K, (c) 1000K and (d) 1100K, without (H_L, left) and with (H_H, right) the impacts of magnon. Green solid lines are the corresponding Lorentzian fitting.

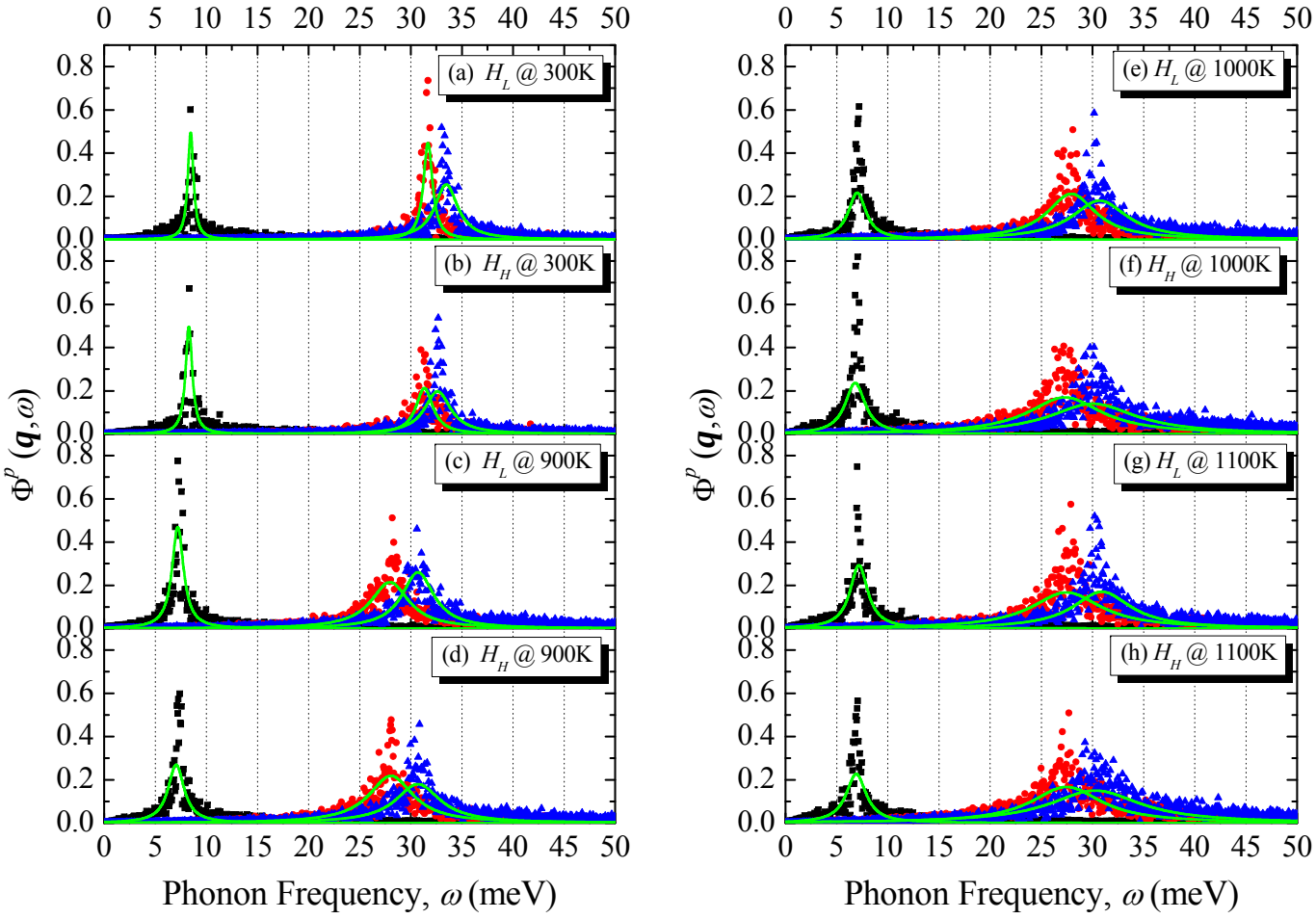

Fig. 4.6: The power spectral density of phonons with q/q_{max} = 0.1 (black square), 0.5 (red circle), 0.9 (blue triangle) along [100] direction at (a) 300K, (b) 900K, (c) 1000K and (d) 1100K, without (left) and with (right) the impacts of magnon. Green solid lines are the corresponding Lorentzian fitting.

Figs. 4.7 show the phonon dispersion curves at various temperatures obtained for H_H and H_L, i.e. with and without the impacts of magnons. Noting the general phonon softening with temperature increase, the 300K results in Fig. 4.7(a) indicates good agreement with *ab initio* results [37]. Comparison between Figs. 4.7(a) & (b) again shows obvious phonon softening as temperature increases, consistent with Figs 4.5 & 4.6.

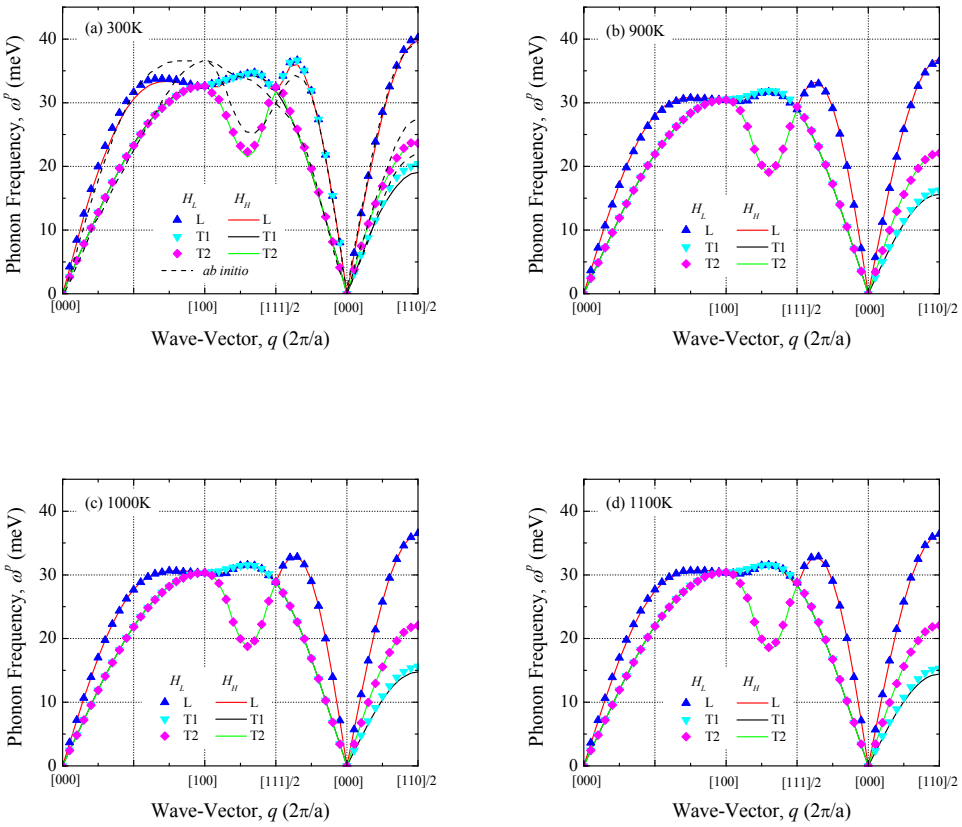

Fig. 4.7: The phonon dispersion curves without (data points, H_L) and with (solid lines, H_H) magnons at various temperatures: (a) 300K, (b) 900K, (c) 1000K, and (d) 1100K. A*b initio* calculation results [37] (Dashed lines) corresponding to 0K are presented in (a) for comparison.

On the other hand, phonon dispersion shows little obvious change when temperature increases. This could be due to the excessive "hardness" of the DD potential used in the current calculations, giving rise to strong harmonicity as discussed in the foregoing. Comparison of the phonon dispersion curves between H_L and H_H reveals the relatively small effects of magnon excitations on the phonon spectrum, even at the temperature near T_C, i.e. 1100K. Nevertheless, a small amount of softening of the transverse phonon branch along [110] direction, i.e. “T1” branches, can be seen in Figs. 4.7.

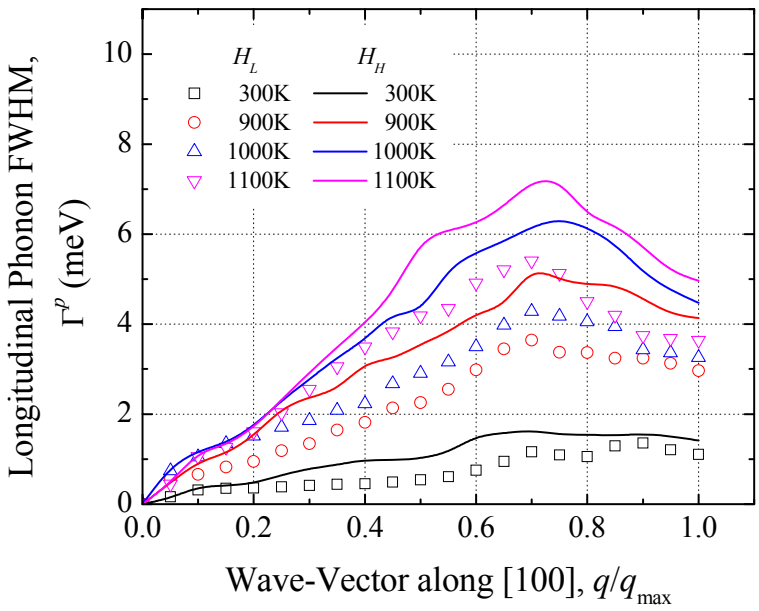

Fig. 4.8: The full-width at half maximum (FWHM) of the longitudinal phonons along [100] direction at various temperatures, without (data points, H_L) and with (solid lines, H_H) the impacts of phonon, respectively.

Fig. 4.8 shows the line widths Γ^p of phonons along [100] direction in terms of the FWHM. At a low temperature like 300K, the vibrations of atom are small and can be treated as harmonic. Multi-phonon interaction is unimportant, so that the line widths are relatively small. As temperature increases, the increased amplitude of the lattice vibrations begins to experience the anharmonicity of the crystal potential. Interaction among phonons broadens the line width Γ^p (~3-6 meV) due to admixture (scattering), especially for the phonons with large wave-vectors. Likewise, interaction with magnons further increases the phonon line width significantly by ~50% (~3-6 meV). The increase of line width is temperature dependent increasing from ~0.3meV at 300K to ~2meV at 1100K.

4.5 Power Spectra Density of Magnons

The power spectral density of magnons with wave-vectors $q/q_{\max}$=0.1, 0.5 and 0.9 along [100] direction at various temperatures are plotted in Figs. 4.9, with and without interacting with the phonons. Magnon softening with increasing temperature is clear, leading to the FM/PM phase transition. For example, ω^m for magnons of $q/q_{\max}$=0.1 decreases from ~15meV at 300K to ~1meV at 1100K. At the same time, the magnon line width Γ^m increases due to enhanced magnon scattering. Meanwhile, interaction with phonons in H_H, plotted in Figs. 4.9, causes more magnon scattering, giving rise to a larger Γ^m and a smaller

ω^m, i.e. more softening. These phonon-effects on magnons softening are significant at high temperatures near the magnetic phase transition, i.e. from 900 to 1100K (See in Table 4.2). The range of magnon lifetime is much wider than that of the phonons, namely, from ~3ps to ~2fs, revealing the stronger anharmonicity of the spin vibrations. The results are in good general agreement with the experimental data [35,40,41].

TABLE 4.2: Magnon frequency, broadening and lifetime along [100] direction in BCC iron, without (H_S) and with (H_H) the impacts of phonons.

q/q_{max}		$T = 300$K		900K		1000K		1100K	
		H_S	H_H	H_S	H_H	H_S	H_H	H_S	H_H
ω^m (meV)	**0.1**	15.5	15.3	10.15	9.12	7.84	5.61	3.63	0.54
	0.5	273.1	272.7	197.2	187.3	174.9	150.3	120.0	46.8
	0.9	459.3	458.5	370.6	352.4	335.6	300.9	230.7	171.4
Γ^m (meV)	**0.1**	0.10	0.10	1.03	2.24	1.66	3.50	2.36	3.62
	0.5	2.88	3.62	47.6	67.4	59.8	75.5	80.0	89.7
	0.9	4.61	5.38	58.1	77.9	96.2	122.3	128.8	164.6
τ^m (fs)	**0.1**	3291	3291	319.5	146.9	198.3	94.03	139.5	90.91
	0.5	114.3	90.91	6.914	4.883	5.503	4.359	4.114	3.669
	0.9	71.39	61.17	5.664	4.225	3.421	2.691	2.555	1.999

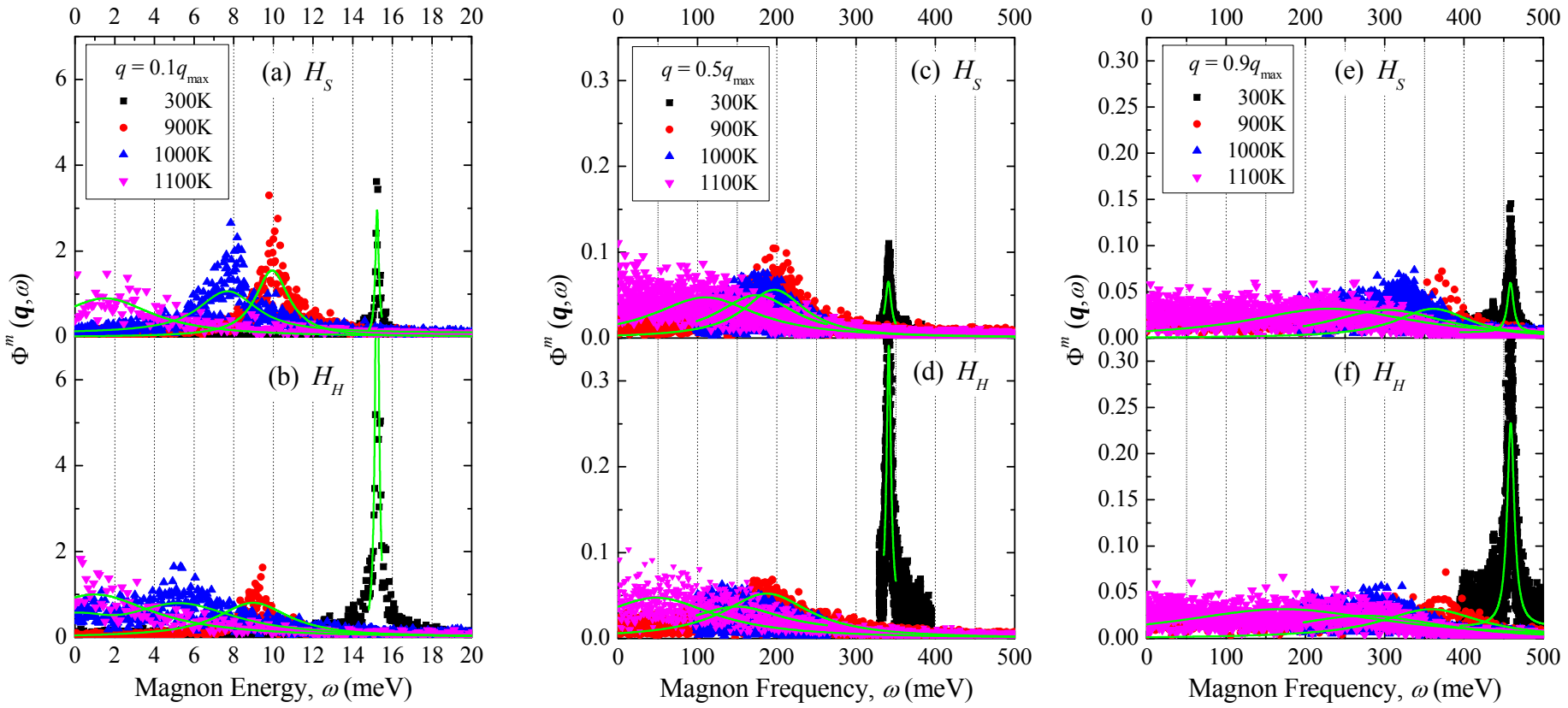

Fig. 4.9: The magnon power spectra density of q/q_{max} = 0.1, 0.5 and 0.9 along [100] direction, without (H_S) and with (H_H) the impacts of phonon, at various temperatures: 300K (black square), 900K (red circle), 1000K (blue upward triangle) and 1100K (pink downward triangle). Green solid lines are the corresponding Lorentzian fitting.

Fig. 4.10 shows the magnon dispersion curves along [100] direction for various temperatures, with and without phonon-magnon interaction. We note that the energies of magnons are much larger than those of the phonons due to the much higher magnon frequencies.

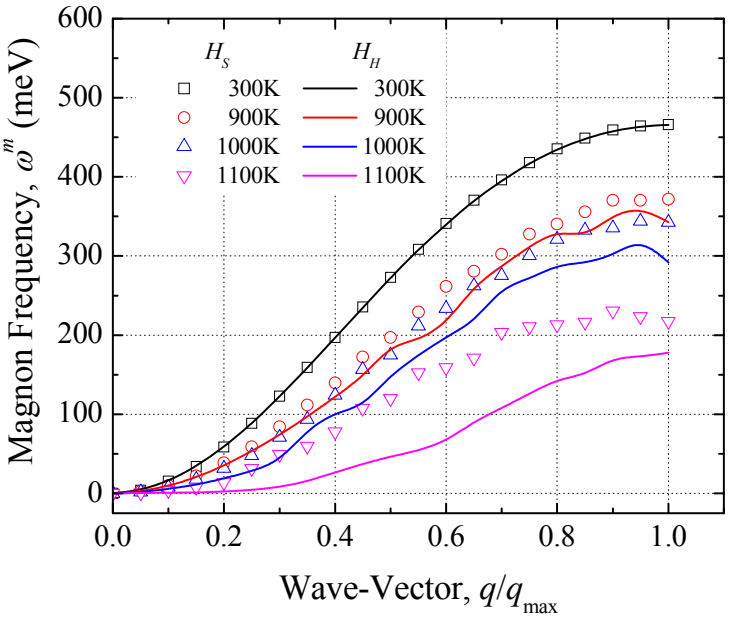

Fig. 4.10: The magnon dispersion curves along [100] directions with (solid lines, H_H) and without (data points, H_S) the impacts of phonons at various temperatures.

Magnon softening with increasing temperature is clear in Fig. 4.10, occurring at a much faster rate than the phonon counterpart, especially near the Brillouin zone boundary. This reflects the stronger anharmonicity of the spin vibrations. It is obvious that interaction with phonons also softens the magnon spectrum. The amount of softening obtained in the current calculations is

consistent with other theoretical predictions, such as the classical spin dynamics-study of magnon near T_C of Landau and co-workers [38,39].

It should be noted that only short-range magnetic ordering exists in the PM phase, confirmed by neutron scattering experiments of Lynn [35]. This is also apparent from the magnon dispersion curves at 1100K in Fig. 4.10, where the magnon energy is nearly zero for magnons with small wave-vectors, indicating the instability of magnetic order of long-wave length, leading to the magnetic phase transition from FM to PM. Compared to the results of H_S, phonon scattering in H_H enhances the magnon softening significantly. For example, due to the scattering with phonons, the energy of a magnon near FM/PM phase boundary decreases from ~370meV to ~350meV at 900K, and from 280meV to ~170meV at 1100K (Fig. 4.10). Of course, at low temperatures, such as 300K, due to the small number of both phonons and magnons, phonon scattering of the magnons is relatively rare, so that the magnon dispersion curves of H_H and H_S are practically the same. In this regard, in BCC iron, the effects of phonons on magnon dispersion are significant only at high temperatures, where the phonon-magnon interaction is strong enough to affect the spin wave stiffness significantly.

Fig. 4.11 shows the line width of magnons along [100] direction at various temperatures, with and without the influence of phonon, respectively, obtained from H_H and H_S.

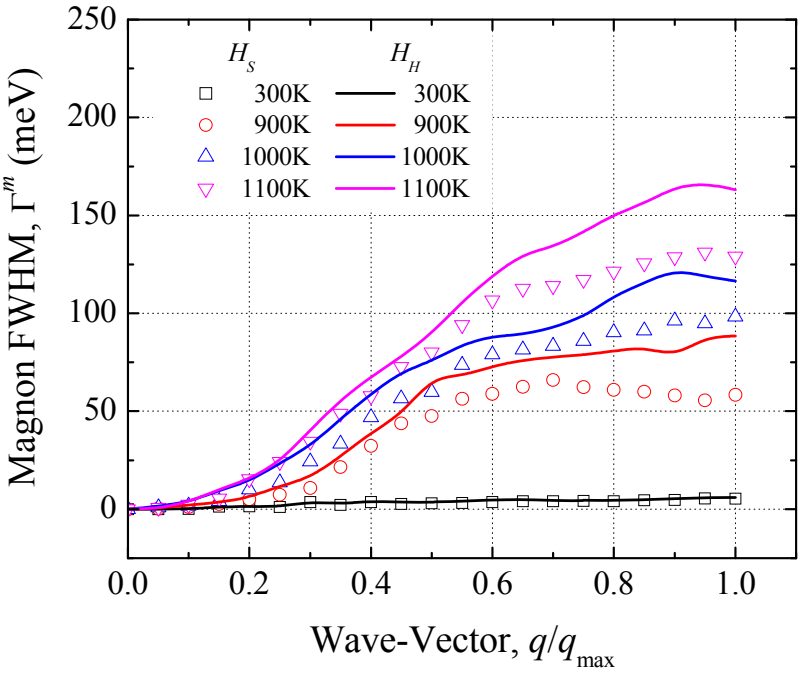

Fig. 4.11: The full-width at half maximum (FWHM) of magnons along [100] direction at various temperatures, without (data points, H_S) and with (solid lines, H_H) the impacts of phonon, respectively.

It can be seen from Fig. 4.11, that the phonon scattering generally results in the broadening of the magnons' line width, which increases with increasing temperature. The broadening is particularly significant for the magnons near FM/PM phase boundary. For example, the increase is only ~5meV at 900K, but

becomes ten-fold to~50meV at 1100K (Fig. 4.11). In addition, such an effect of phonon-magnon interaction is larger for the magnons with larger momentum.

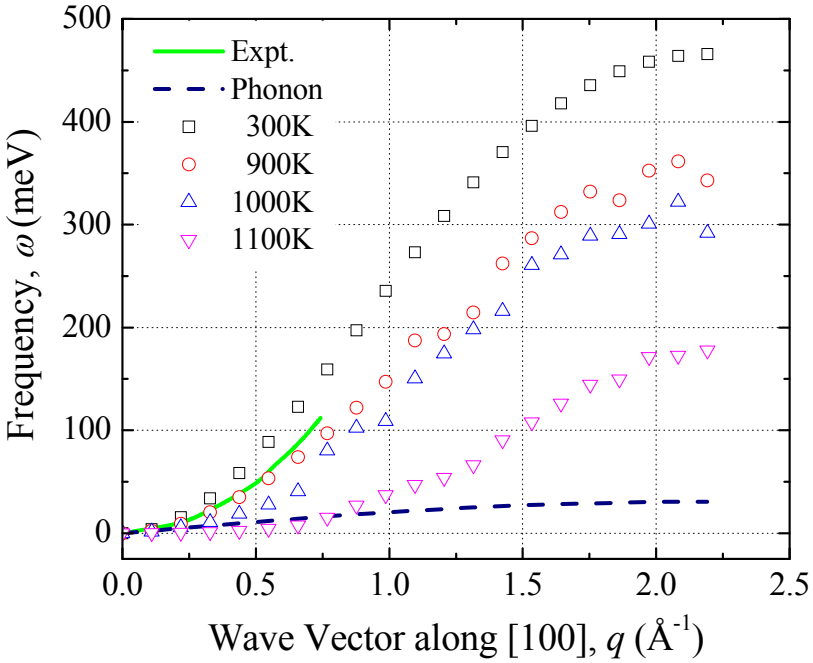

Fig. 4.12: The magnon dispersion curves at various temperatures with the impacts of phonon-magnon interaction, obtained from SLD simulations, compared to the longitudinal phonon at 300K (dashed line) obtained by the same routine, and the experimental measurements (297K) done by Collins *et al.* [40] and Mook *et al.* [41] (Green solid line). (Note that the unit of wave-vector is different between the previous figures)

Fig. 4.12 plots the magnon dispersion curves at various temperatures, calculated using H_H, compared with neutron scattering measurements done by Collins *et al.* [40] and Mook *et al.* [41]. The longitudinal phonon dispersion curve at 300K is also shown for comparison. It can be seen that the calculated

results are in good general agreement with the experimental measurements. In addition, the phonon frequency is much smaller than that of the magnons, and there is apparent overlapping only at the temperatures near T_C as expected.

4.6 Spin Stiffness

In Section 2.3, the spin wave stiffness D is an important quantity describing the dynamics of spin system, which can be obtained from the magnon dispersion curves.

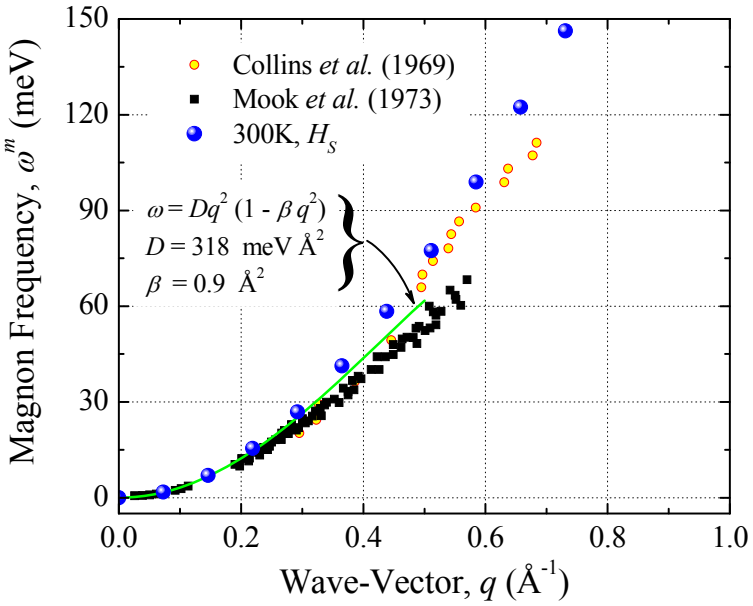

Fig. 4.13: The spin stiffness obtained from fitting the magnon dispersion curve from H_S is compared with the experimental data measured by Collins *et al.* [40] and Mook *et al.* [41].

Here, due to the isotropic nature of the BCC structure and the exchange integral governing the spin dynamics, as shown in the Hamiltonian H_S (Eq.

(4.5)), the magnon frequency only depends on the magnitude of wave-vector, but independent of its direction. Approximating the dispersion relation in the small wave-vector region ($qa \ll 1$, with a being the lattice parameter) by

$$\hbar\omega_q^m = Dq^2\left(1-\beta q^2\right) \tag{4.16}$$

where β is a fitting parameter, one can obtain a spin stiffness $D = 318\text{meV}\cdot\text{Å}^2$ and $\beta = 0.9\,\text{Å}^2$ by fitting to the data points of magnon dispersion curves of H_S at 300K (See in Fig. 4.13). The results are in good agreement with the experimental data [40,41].

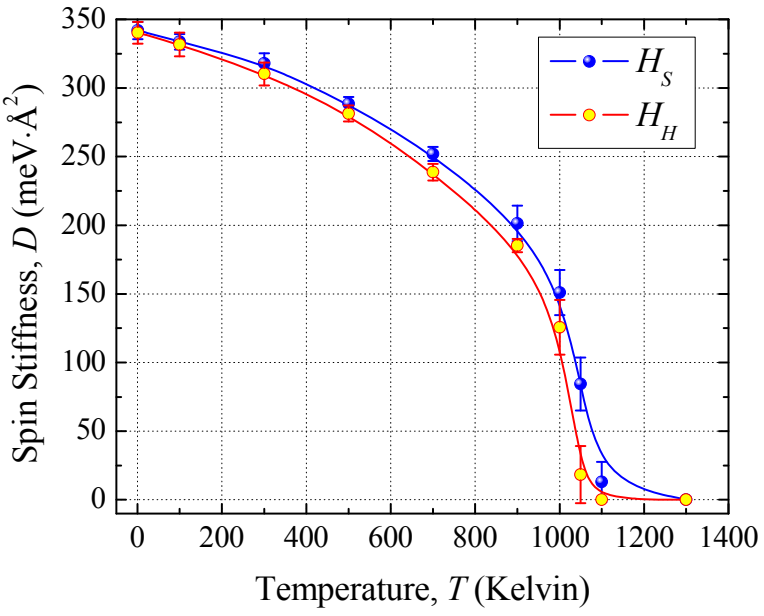

Fig. 4.14: The temperature dependence of spin stiffness, without (H_S) and with (H_H) the impact of phonons over the temperature regime across the FM/PM phase boundary. Here, the values of spin stiffness at 1300K in both cases are set as zero for the purpose of obtaining a complete curve to guide the eye.

The spin stiffness as a function of temperature is plotted in Fig. 4.14, with (H_H) and without (H_S) the phonon-magnon interaction over a wide temperature range from 1K to 1300K. Here, the values of spin-stiffness in both cases are set as zero artificially at 1300K, just to guide the eye. This is valid since there is no long range magnetic order maintained in the PM phase [35]. It can be seen from Fig. 4.14, that the value of D for both H_S and H_H gradually decreases from ~350meV·Å^2 at 1K to ~200meV·Å^2 at 900K, then decreases sharply to nearly zero at the temperature region between 1000K to 1100K, near the FM/PM phase boundary. The difference in the values of D between H_S and H_H is relatively small, i.e. ~10meV·Å^2, except for the temperatures near T_C, i.e. ~50meV·Å^2 at 1050K.

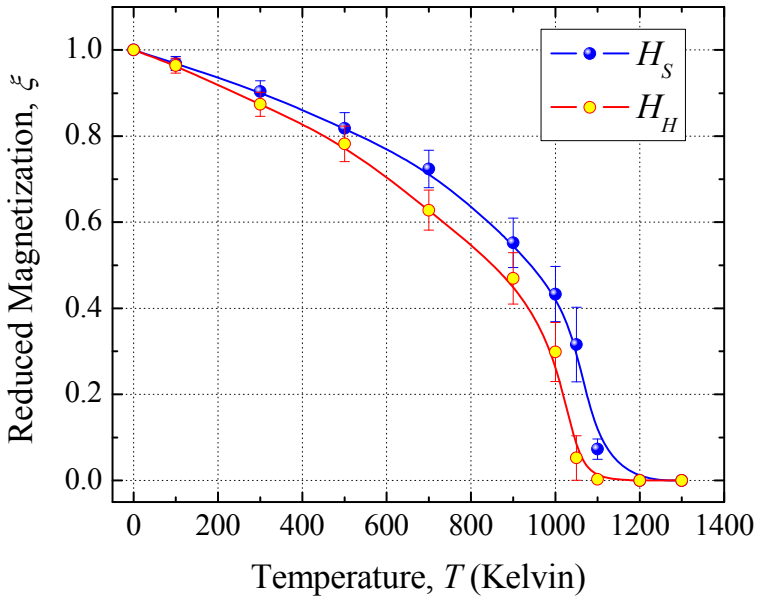

Fig. 4.15: The temperature dependence of reduced magnetization, without (H_S) and with (H_H) the impacts of phonon in a wide temperature region across the FM/PM phase boundary.

It is obvious that the phonon-scattering of magnons does produce a shift of T_C with a value ~50K, from ~1100K in H_S to ~1050K in H_H, which is also revealed in the reduced magnetization $\xi(T)$, i.e. $\xi(T) = M(T)/M(0)$, plotted in Fig. 4.15. In the coupled system involving interactive spin and lattice described by H_H, anharmonicity caused by the phonon-magnon interaction changes the thermal expansion and causes the temperature dependence of the atomic environment of the interactive spins. In addition, the dependence of exchange integral in Eq. (4.4) on atomic distance decreases with increasing temperature, so that the spin-stiffness is smaller than that in H_S, where the lattice parameter is kept constant in the whole temperature region. Here, the thermal expansion due to phonon-magnon scattering shows anomalous temperature dependence near T_C, which will be discussed in the following Chapter.

As shown in Figs. 4.14 & 4.15, the temperature dependence of spin stiffness is similar to that of reduced magnetization. In fact, for the case of small spin vibration amplitude [42], the magnon dispersion relation in a BCC crystal containing the first- and second-nearest-neighbor (1st- and 2nd-NN) spin-spin interactions, is expressed as in Eq. (2.100), i.e.

$$\hbar\omega_q = \left(J_{ij}^{1\mathrm{NN}} + J_{ij}^{2\mathrm{NN}}\right) Sa^2 q^2 \equiv Dq^2 . \tag{4.17}$$

Therefore, the spin stiffness D is given by

$$D = \left(J_{ij}^{1\mathrm{NN}} + J_{ij}^{2\mathrm{NN}} \right) S a^2 , \tag{4.18}$$

with $J_{ij}^{1\mathrm{NN}}$ and $J_{ij}^{2\mathrm{NN}}$ being respectively the 1st- and 2nd-NN exchange integral, determined by the functional form of Eq. (4.4). Here, it should be noted that, in classical model, S in Eq. (4.18) is the projection of atomic spins along the quantized axis, i.e. z-axis in our calculations. In this regard, the spin stiffness at finite temperature is expressed as

$$\begin{aligned} D(T) &= \left(J_{ij}^{1\mathrm{NN}} + J_{ij}^{2\mathrm{NN}} \right) a^2 S^z \\ &= \left(j_{ij}^{1\mathrm{NN}} + j_{ij}^{2\mathrm{NN}} \right) a^2 \xi(T) / S \end{aligned} , \tag{4.19}$$

where $S^z = S\xi(T)$ and $j_{ij} = J_{ij} S^2$.

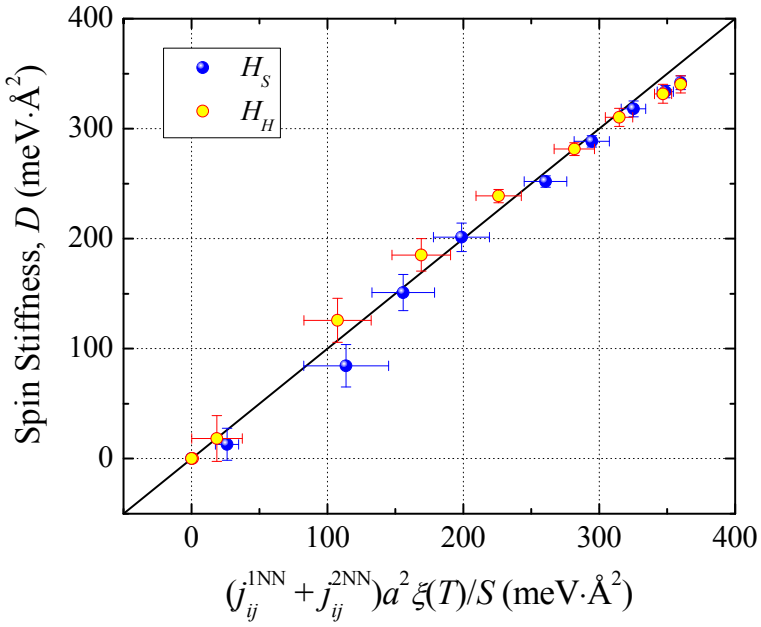

Fig. 4.16: The calculated spin stiffness (see in Fig. 4.14) compares to the theoretical prediction following Eq. (4.19), without (H_S) and with (H_H) the impacts of phonons. The solid line is the expected asymptote.

Fig. 4.16 shows the relation between the spin stiffness $D(T)$ predicted by Eq. (4.19) and that obtained from the magnon dispersion curves. The good agreement shows good consistency of our calculation with theoretical predictions, despite the impacts of phonons. On the other hand, the general expression of the magnon dispersion relation can be safely promoted to the case involving 2nd-NN spin-spin interactions.

4.7 Chapter Conclusion

In this Chapter, the power spectra density of phonons and magnons, and the resulting dispersion curves and the full-width at half maximum (FWHM) are calculated, and the influence of phonon-magnon coupling at various temperatures is investigated. For phonons, interaction with magnons produces little effects on the dispersion curves, but results in significant increase of the FWHM at the temperature region near T_C, thus decreasing the lifetimes of phonons. On the other hand, interaction with phonons causes the magnons softened as temperature increases, with simultaneous line broadening. In addition, the phonon-magnon interaction gives rising to the shift of T_C, due to the change in atomic environment and the exchange integral governing the spin dynamics, so that the temperature dependence of the spin-stiffness reveals apparent change near the FM/PM phase boundary. The calculation results mentioned above are in good

general agreement with the available experimental measurements and other calculations.

Reference

[1] N. W. Ashcroft and N. D. Mermin, *Solid State Physics* (Saunders College, Philadelphia, 1976).

[2] M. Born and K. Huang, *Dynamical Theory of Crystal Lattices*, (Oxford University Press, London, 1954), pp. 38-60.

[3] C. Kittel, *Introduction to Solid State Physics*, 8th ed. (John Wiley & Sons, New York, 2005), pp. 120.

[4] D. C. Wallace, *Thermodynamics of Crystals* (Dover, New York, 1998).

[5] B. Fultz, Prog. Mater. Sci. 55, 247 (2010).

[6] A.A. Maradudin, A. E. Fein, Phys Rev **128**, 2589 (1962).

[7] E. R. Callen, and H. B. Callen, Phys. Rev. **129**, 578 (1963); **139**, A455 (1965).

[8] E. R. Callen, J. Appl. Phys. **39**, 519 (1968), and the reference therein.

[9] F. Körmann A. Dick, B. Grabowski, B. Hallstedt, T. Hickel, and J. Neugebauer, Phys. Rev. B **78**, 033102 (2008).

[10] A. I. Akhiezer, J. Phys. (U.S.S.R.) **10**, 217 (1946).

[11] Y. M. Yakovley, Y. N. Brudin, Y. R. Shilnikov, T. N. Bushveva, Sov. Phys. Solid State, **12** 2475 (1971).

[12] R. Elliott, and H. Stern, Proc. Vienna Symposium on Neutron Scattering, I.A.E.A. (1960).

[13] Ph. Kurz, F. Förster, L. Nordström, G. Bihlmayer, and Blügel, Phys. Rev. B **69**, 024415 (2004).

[14] O. Grotheer, C. Ederer, and M. Fähnle, Phys. Rev. B **62**, 5601 (2000).

[15] O. Grotheer, C. Ederer, and M. Fähnle, Phys. Rev. B **63**, 100401 (2001).

[16] S. Moran, C. Edere, and M. Fähnle, Phys. Rev. B **67**, 012407 (2003).

[17] S. V. Halilov, A. Y. Perlov, P. M. Openeer, and H. Eschrig, Europhys. Lett. **39**, 91 (1997).

[18] S. Y. Savrasov, Phys. Rev. Lett. **81**, 2570 (1998).

[19] R. F. Sabiryanov and S. S. Jaswal, Phys. Rev. Lett. **83**, 2062 (1999).

[20] A. Bergman, A. Taroni, L. Bergqvist, Johan Hellsvik, B. Hjörvarsson, and O. Eriksson, Phys. Rev. B **81**, 144416 (2010).

[21] P.-W. Ma, C. H. Woo, and S. L. Dudarev, Phys. Rev. B **78**, 024434 (2008).

[22] S. L. Dudarev, and P. M. Derlet, J. Phys.: Condens. Mat. **17**, 7097 (2005).

[23] W. F. Brown, Jr., Phys. Rev. **130**, 1677 (1963).

[24] N. Hatano, and M. Suzuki, Lect. Notes Phys. **679**, 37 (2005).

[25] B. I. Halperin, and P. C. Hohenberg, Phys. Rev. **177**, 952 (1969).

[26] C. E. Shannon, Proc. Institute of Radio Engineers **37**, 10 (1949).

[27] M. T. Dove, *Introduction to Lattice Dynamics* (Cambridge, London, England, 1993).

[28] Leon W. Couch II, *Digital and Analog Communications Systems*, 6th ed., (Prentice Hall, New Jersey, 2001), pp. 406-409.

[29] N. I. Papanicolaou, I. E. Lagaris, and G. A. Evangelakis, Surf. Sci. **337**, L819 (1995).

[30] P. Heino, Eur. Phys. J. B **60**, 171 (2007).

[31] M. B. Priestley, *Spectral analysis and Time Series*, (Academic Press, 1981).

[32] M. F. Collins, V. J. Minkiewicz, R. Nathans, L. Passell, and G. Shirane, Phys. Rev. **179**, 417 (1969).

[33] A. V. Ruban, S. Khmelevskyi, P. Mohn, and B. Johansson, Phys. Rev. B **75**, 054402 (2007).

[34] K. Chen, and D. P. Landau, Phys. Rev. B **49**, 3266 (1994).

[35] J. W. Lynn, Phys. Rev. B **11**, 2624 (1975).

[36] X. Tao, D. P. Landau, T. C. Schulthess, and G. M. Stocks, Phys. Rev. Lett. **95**, 087207 (2005).

[37] F. Körmann, A. Dick, B. Grabowski, B. Hallstedt, T. Hickel, and J. Neugebauer, Phys. Rev. B **78**, 033102 (2008).

[38] K. Chen, and D. P. Landau, Phys. Rev. B **49**, 3266 (1994).

[39] X. Tao, D. P. Landau, T. C. Schulthess, and G. M. Stocks, Phys. Rev. Lett. **95**, 087207 (2005).

[40] M. F. Collins, V. J. Minkiewicz, R. Nathans, L. Passell, and G. Shirane, Phys. Rev. **179**, 417 (1969).

[41] H. A. Mook, and R. M. Nicklow, Phys. Rev. B **7**, 336 (1973).

[42] C. Kittel, *Introduction to Solid State Physics*, 7th ed. (John-Wiley & Sons, New York, 1995), Chapter **12**.

CHAPTER V

THERMAL AND MECHANICAL PROPERTIES NEAR MAGNETIC-PHASE TRANSITION

We have shown in Chapter VI that our calculated phonon and magnon dispersion relations show strong evidence of phonon-magnon interaction arising from the spin-lattice coupling due to the exchange field. As a result, thermal, mechanical and magnetic properties of BCC iron are simultaneously affected by magnon excitations and are thus coupled. The effects are particularly significant near the FM/PM transition point. This is the subject of study of the present Chapter. The free-energy change of the associated atomic processes will be calculated from the corresponding phase-space trajectory obtained from large-scale spin-lattice dynamics (SLD) simulations, using the modified thermodynamic integration (TI) method.

5.1 Chapter Introduction

In a spin-polarized solid, the excitation of spin vibrations brings both energetic and entropic contributions to its free energy, adding to those coming from the lattice vibrations. The added contributions also include the interaction between lattice and spin degrees of freedom via the exchange field. The coupling between the two types of excitations in atomic processes results in correlations among thermal, mechanical and magnetic properties of the solid. A convenient entry point of such investigations is the free energy of a canonical ensemble, which allows the use as a common parameter the temperature T to label the degrees of excitations of both the lattice and the spins.

Conventionally, the free energy of an ensemble of interacting particles is calculated based on the adiabatic approximation [1,2] assuming that the phonon and magnon excitations reside on different time scales and the lattice and spin degrees of freedom are separable. Two approaches are commonly adopted. In one, the magnetic entropy S_m is derived from the heat capacity C_m by integrating the thermodynamic relation $\mathrm{d}S_m / \mathrm{d}T = C_m / T$. The temperature-dependent heat capacity is obtained either from experiments [3,4], or from empirical relations, such as in Inden [5,6], Hillert and Jarl [7] and Chuang *et al.* [8]. Within this approach, Lavrentiev *et al.* [9] developed an *ab initio* parameterized magnetic cluster expansion model from which the magnetic free energy is evaluated from

the calculated specific heat. In these calculations, the coupling between spin and lattice is not explicitly taken into account. In the other approach, entropies are calculated as the logarithm of the density of states of magnons and phonons, which can be obtained from *ab initio* calculations within the harmonic approximation [10,11,12]. Application of both approaches is restricted to the low-temperature regime, in which the phonon and magnon densities are both low, and anharmonic effects, including those due to their mutual interactions are negligible. Calculated this way, the resulting heat capacity cannot be expected to be accurate near the FM/PM transition temperature [13], missing the sharp peak across the FM/PM phase boundary, for example, found in experiments [3,4].

In this regard, evaluating the free energy of ferromagnetic metals at higher temperatures, particularly near the magnetic transition point, requires the treatment of the full anharmonicity of the coupled spin and lattice vibrations. Such an implementation is now achievable via the recent development of the spin-lattice dynamics (SLD) [14] scheme. More accurate and better-based free energy changes for atomic processes can be calculated from the phase trajectories obtained from large-scale SLD simulations, via the modified thermodynamic integration (TI) method [16]. Our study in the following sections is performed following this approach, in which the free energy changes associated with the atomic processes related to the thermal, magnetic and mechanical properties in BCC iron are calculated.

5.2. Formulation and Methodology

5.2.1. Hamiltonians

In Chapter II, the total Hamiltonian H_H of the ensemble of Heisenberg particles are divided into H_L, H_S, and H_Δ (See Eq. (2.127)), with

$$H_H = \sum_{i=1}^{N} \frac{\boldsymbol{p}_i^2}{2m} + U(\boldsymbol{R}) - \frac{1}{2}\sum_{i\neq j}^{N} J_{ij}(\boldsymbol{R})\boldsymbol{S}_i \cdot \boldsymbol{S}_j , \tag{5.1a}$$

$$H_L(\boldsymbol{R}) = \sum_{i=1}^{N} \frac{\boldsymbol{p}_i^2}{2m_i} + U(\boldsymbol{R}), \tag{5.1b}$$

$$H_S(\boldsymbol{S}) = -\frac{1}{2}\sum_{i\neq j}^{N} J_{ij}(\bar{\boldsymbol{R}})\boldsymbol{S}_i \cdot \boldsymbol{S}_j , \tag{5.1c}$$

$$H_\Delta(\boldsymbol{R},\boldsymbol{S}) = -\frac{1}{2}\sum_{i\neq j}^{N} \delta J_{ij}\boldsymbol{S}_i \cdot \boldsymbol{S}_j , \tag{5.1d}$$

where $U(\boldsymbol{R})$ is the interatomic potential, which can be derived from the Dudarev-Derlet (DD) potential [17] in the form of Eq. (4.2). The details have already been discussed in Chapter IV, and will not be repeated here.

5.2.2. Thermal energy

The energy change of a canonical ensemble arising from a temperature change can be calculated from the change of the statistical mean of the micro internal energy in a large-scale dynamical simulation. However, the contribution

due to thermal vibration, i.e., the vibrational energy E_{vib}, must exclude the mechanical work due to the re-establishment of the new equilibrium lattice configuration caused by the temperature change. In this regard, equilibrium lattice positions within the quasi-harmonic approximation [18] are assumed to be temperature-dependent to reflect the ensuing thermal expansion/contraction. The total energy $E(T)\big|_{V(T,P=0)}$ of the canonical ensemble at *T* can then be written as a sum of the static energy $E_0(T)$ and the vibrational energy $E_{\text{vib}}(T)$, i.e.,

$$E(T) \equiv E_0(T) + E_{\text{vib}}(T), \tag{5.2}$$

where the static energy $E_0(T)$ is the "ground-state" energy at *T*, with static spins and atoms at the time-averaged (quasi-harmonic equilibrium) spin-lattice configuration at temperature T. $E_{\text{vib}}(T)$ is the vibrational energy gained by the crystal when it is brought under zero pressure from the "ground state" to the thermal excited state at T. We note that $E_0(T)$ contains the work done due to the change of the static lattice as a function of temperature, which is unrelated to the excitation of the vibrational states due to heat transfer to and from the ensemble [18]. Energies of the thermal excitations, such as phonons for the lattice subsystem and magnons for spin subsystem, are not contained in $E_0(T)$, but in $E_{\text{vib}}(T)$, which may be identified as the thermal energy $E_{\text{th}}(T)$.

Thermal properties, such as the constant-pressure specific heat $C_P(T)$ and heat transfer coefficient, are derived from the temperature dependence of E_{th} according to [18]

$$C_P(T) = \frac{\partial}{\partial T} E_{\text{th}}(T), \tag{5.3}$$

rather than from the total energy that also contains the static energy $E_0(T)$, the temperature dependence of which is derived from that of the atomic volume. It is obvious that the thermal properties are directly related to the interacting magnon and phonon subsystems, and through them, to mechanical stresses and strains, and magnetization. The underlying cause of the correlation among the thermal, mechanical and magnetic properties in ferromagnetic materials is then clear.

5.2.3 Grüneisen parameter and thermal expansion coefficient

Many fundamental thermal properties of materials [19], such as thermal conductivity, expansivity, and in general heat dissipation in atomic processes, originate from the associated anharmonicity. In a harmonic lattice, for example, phonons do not interact and has an infinite lifetime, as discussed in Chapter IV. There is zero thermal expansion and infinite thermal conductivity. Anharmonicity in this regard can be measured in terms of E_0 and E_{vib} of the phonon subsystem, by the Grüneisen parameter γ, according to Mie-Grüneisen's equation of state [20],

$$\gamma = \frac{V}{E_{\text{vib}}}\left(\frac{\mathrm{d}E_0}{\mathrm{d}T} + P\right) \tag{5.4}$$

where the hydrostatic pressure P is zero in the current calculations.

The thermal expansion coefficient α is also an indicator of anharmonicity, derived from the temperature dependence of the equilibrium atomic volume V of the system under a constant hydrostatic pressure P (usually set $P = 0$),

$$\alpha = \frac{1}{V}\left(\frac{\mathrm{d}V}{\mathrm{d}T}\right)_P \tag{5.5}$$

The constant hydrostatic pressure condition in our simulations is realized by using the Berendsen barostat [21] algorithm described in Chapter III.

5.2.4 Free energy and entropy

Thermodynamically, material properties are derived from free energy changes of the atomic process involved. The TI method [15,16] uses the fact that the free energy change between two equilibrium states is given by the work done in bringing the system, via any reversible path, from one state to the other [22]. Thus, given a reference state govern by a Hamiltonian H^0 with free energy F^0, the free energy F^1 of a nearby state govern by Hamiltonian H^1 can be calculated according to,

$$F^1 = F^0 + \Delta F = F^0 + \int_0^1 \left\langle \frac{\partial H^\lambda}{\partial \lambda} \right\rangle \mathrm{d}\lambda\,, \tag{5.6}$$

where $H^{\lambda} = \lambda H^{1} + (1-\lambda) H^{0}$ is the transit Hamiltonian responsible for the resistance along the integration path (see Chapter III for details). We follow the usual practice and use the Einstein solid [15] as the reference lattice subsystem. The paramagnetic ensemble [23] is used as the reference spin subsystem. Accordingly, the reference Hamiltonian H^{0} is a sum of H_L^0 for the lattice subsystem and H_S^0 for the spin subsystem, where [15,23]

$$H_L^0 = \sum_{i=1}^{N} \frac{\boldsymbol{p}_i^2}{2m} + E_0 + \frac{1}{2}\sum_{i=1}^{N} m\omega^2 \left(\boldsymbol{R}_i - \boldsymbol{R}_i^0\right)^2 \tag{5.7a}$$

$$H_S^0 = g\mu_{\mathrm{B}} \sum_{i=1}^{N} \boldsymbol{H}_{\mathrm{ext}} \cdot \boldsymbol{S}_i \tag{5.7b}$$

Here, E_0 is the static energy defined in Eq. (5.2), $\omega = 4\times10^{13}\mathrm{Hz}$ (near the Debye frequency of iron [24]) is taken as the uniform vibration frequency of the Einstein solid. $\boldsymbol{R}_i$ and $\boldsymbol{R}_i^0$ represent the instantaneous position and lattice site of atom i, and $\boldsymbol{H}_{\mathrm{ext}} = 300\mathrm{T}$ is a specified external magnetic field. It has been verified that the results are not sensitive to the specific values of $\boldsymbol{H}_{\mathrm{ext}}$ chosen, up to 3000T. The reference free energies are given by [15,23]

$$F_L^0 = E_0 - 3k_{\mathrm{B}}T \ln\left(\frac{\hbar\omega}{k_{\mathrm{B}}T}\right) \tag{5.8a}$$

$$F_S^0 = -k_{\mathrm{B}}T \ln\left\{4\pi \frac{\sinh(x)}{x}\right\}, \qquad \left(x = \frac{g\mu_{\mathrm{B}}H_{\mathrm{ext}}S_i}{k_{\mathrm{B}}T}\right). \tag{5.8b}$$

Consistent with the interpretation of the total energy within the quasi-harmonic approximation [18], the free energy can also be defined as the sum of the static energy E_0 and the thermal free energy $F_{\text{th}}(T)$, i.e. $F = E_0 + F_{\text{th}}$. F_{th} is the free energy responsible for the thermal excitations. The energy increase E_{th} and the heat dissipation in terms of entropy S are produced by the relaxation of the microstates during the excitation. From the free energy $F(T)$, the entropy $S(T)$ can be calculated using the thermodynamic relationship $S = -(\partial F / \partial T)_V$. However, as explained in the foregoing paragraphs, the temperature dependence of the static energy E_0 contained in F is not related to the thermal excitations [18]. It should thus be discounted when calculating the entropy. Besides, differentiating among finite data points of free energy could introduce very substantial numerical error. Thus, in the present work, the alternate relationship $S = (E_{\text{th}} - F_{\text{th}})/T$ is used instead.

5.2.5. Calculation of the isothermal elastic constants

The linear elastic properties of a cubic crystal such as BCC iron can be described by the three elastic constants c_{11}, c_{12} and c_{44}. Equivalently, the bulk modulus $B = (c_{11} + 2c_{12})/3$ and the tetragonal shear modulus $c' = (c_{11} - c_{12})/2$ can also be used, instead of c_{11} and c_{12} [25]. The isothermal elastic constants measure the resistances to small elastic strains *at constant temperature*, which can be derived from the free energy change due to isothermal straining of the

atomic lattice [26]. Thus, the bulk modulus B can be obtained by applying a uniform hydrostatic strain $\boldsymbol{\varepsilon}$ of infinitesimal magnitude,

$$\boldsymbol{\varepsilon} = \frac{1}{3}\begin{pmatrix} \delta & 0 & 0 \\ 0 & \delta & 0 \\ 0 & 0 & \delta \end{pmatrix}, \tag{5.9}$$

where δ is the magnitude of the strain. Then the free energy of the strained sample is given by

$$F(\delta) = F(0) + \frac{1}{2}BV\delta^2 + O(\delta^3), \tag{5.10}$$

where $F(0)$ is the unstrained free energy and V the instantaneous volume under the strain. Similarly, c' can be derived from a isochoric tetragonal shear strain $\boldsymbol{\varepsilon}$, in the form:

$$\boldsymbol{\varepsilon} = \begin{pmatrix} \delta & 0 & 0 \\ 0 & \delta & 0 \\ 0 & 0 & (1+\delta)^{-2} - 1 \end{pmatrix}, \tag{5.11}$$

with the corresponding free energy written as

$$F(\delta) = F(0) + 6c'V\delta^2 + O(\delta^3). \tag{5.12}$$

And c_{44} is calculated from the isochoric orthorhombic shear strain

$$\boldsymbol{\varepsilon} = \begin{pmatrix} 0 & \delta & 0 \\ \delta & 0 & 0 \\ 0 & 0 & \delta^2/(1-\delta^2) \end{pmatrix}, \tag{5.13}$$

with the corresponding free energy

$$F(\delta) = F(0) + 2c_{44}V\delta^2 + O(\delta^3). \tag{5.14}$$

The quadratic coefficients of $F(\delta)$ give the corresponding elastic constants. However, such a free energy change due to a small strain is usually small compared with the intrinsic thermal fluctuations of the large number of atoms in the system. To overcome such difficulties, the TI method [15,16] is adopted as described briefly in the following.

We consider a thermodynamic process, in which a strain $\boldsymbol{\varepsilon}$ is incrementally applied onto an unstained equilibrium crystal, according to $\boldsymbol{\varepsilon} = \lambda\boldsymbol{\varepsilon}_0$ with $0 \le \lambda \le 1$. Since the applied strain would affect the interatomic distance in MD scheme, if $\boldsymbol{r}_{ij}(\boldsymbol{\varepsilon})$ represents the interatomic distance between atom i and j under the intermediate state with strain $\boldsymbol{\varepsilon}$, we can write

$$\boldsymbol{r}_{ij}(\boldsymbol{\varepsilon}) = (\boldsymbol{I} + \boldsymbol{\varepsilon})\boldsymbol{r}_{ij}^0 \tag{5.15}$$

where $\boldsymbol{r}_{ij}^0$ denotes the interatomic distance under the stress-free condition and $\boldsymbol{I}$ is the identity matrix. Therefore, according to the TI method, the free energy change can be rewritten as

$$\begin{aligned} F(\boldsymbol{\varepsilon}_0) - F(0) &= \int_0^1 \left\langle \frac{\partial H_\lambda}{\partial \lambda} \right\rangle_\lambda \mathrm{d}\lambda \\ &= \int_0^1 \left\langle \sum_{i,j} \frac{\partial H_\lambda}{\partial \mathbf{r}_{ij}} \cdot \frac{\partial \mathbf{r}_{ij}}{\partial \lambda} \right\rangle_\lambda \mathrm{d}\lambda \\ &= \int_0^1 \left\langle -\sum_{i,j} \boldsymbol{f}_{ij}^\lambda \cdot \left(\boldsymbol{\varepsilon}_0 \mathbf{r}_{ij}^0 \right) \right\rangle_\lambda \mathrm{d}\lambda \\ &= \int_0^{\varepsilon_0} \left\langle -\sum_{i,j} \boldsymbol{f}_{ij}^\lambda \cdot \left(\boldsymbol{\varepsilon}_0 \mathbf{r}_{ij}^0 \boldsymbol{\varepsilon}_0^{-1} \right) \right\rangle_{\boldsymbol{\varepsilon}} \mathrm{d}\boldsymbol{\varepsilon} \end{aligned} \tag{5.16}$$

where $\boldsymbol{f}_{ij}^\lambda = -\partial H_\lambda / \partial \mathbf{r}_{ij}$ is the interatomic force of atoms i and j at the intermediate state defined by H_λ, the Hamiltonian with the applied strain $\boldsymbol{\varepsilon} = \lambda \boldsymbol{\varepsilon}_0$. In this regard, $Y(\boldsymbol{\varepsilon}) \equiv \left\langle -\sum_{i,j} \boldsymbol{f}_{ij}^\lambda \cdot \left(\boldsymbol{\varepsilon}_0 \mathbf{r}_{ij}^0 \boldsymbol{\varepsilon}_0^{-1} \right) \right\rangle_{\boldsymbol{\varepsilon}}$ can be treated as the corresponding thermodynamic force versus the generalized thermodynamic coordinate $\boldsymbol{\varepsilon}$, that measures the resistance of the deformation of $\boldsymbol{\varepsilon}$. Hence, the accumulate work done during this thermodynamic process

$$W(\boldsymbol{\varepsilon}') \equiv \int_0^{\varepsilon'} \left\langle -\sum_{i,j} \boldsymbol{f}_{ij}^\lambda \cdot \left(\boldsymbol{\varepsilon}_0 \mathbf{r}_{ij}^0 \boldsymbol{\varepsilon}_0^{-1} \right) \right\rangle_{\boldsymbol{\varepsilon}} \mathrm{d}\boldsymbol{\varepsilon} \tag{5.17}$$

is the mechanical work done with the crystal deformed from $\boldsymbol{\varepsilon} = 0$ to $\boldsymbol{\varepsilon} = \boldsymbol{\varepsilon}'$. For example, in the calculation of bulk modulus, the free energy of the uniformly strained crystal with strain δ can be written as

$$\begin{aligned} F(\delta) &= F(0) + \int_0^\delta Y(\varepsilon) \mathrm{d}\varepsilon \\ &= F(0) + \int_0^\delta \left\langle -\sum_{i,j} \boldsymbol{f}_{ij}^\lambda \cdot \mathbf{r}_{ij}^0 \right\rangle_{\boldsymbol{\varepsilon}} \mathrm{d}\varepsilon \end{aligned} . \tag{5.18}$$

5.3 Simulation Scheme

Phase trajectories used for calculating the mean energies and for TI are obtained for various temperatures via SLD, MD and SD simulations. NVT simulations are carried out with temperature-dependent equilibrium lattice parameters, which are obtained by NPT simulations beforehand, and Langevin thermostat [14,27] to keep the system at a pre-set temperature. The computation is performed using the Suzuki-Trotter decomposition [28] with a time-step of 1 femto-second. Canonical ensemble averages in Eq. (4.5) between 500K and 1300K are obtained using the phase-space trajectories, a temperature range that may be considered sufficiently wide for a credible analysis in the neighborhood of the FM/PM transition. We note that the BCC structure remain stable in this temperature range because the DD potential [17] used in our calculations does not reproduce the expected BCC to FCC structural phase transition at 1183K for iron [9].

The simulation cell contains 16000 atoms in a box of $20\times20\times20$ BCC unit cells in Cartesian coordinate system. Periodic boundary conditions are applied to avoid surface effects. To allow for the slowing down of the spin subsystem near T_C [29], at least 2 nano-seconds of equilibrium time is set. To obtain the equilibrated atomic volume under stress-free conditions, the dimension length along each direction in Cartesian coordinate system is sampled within the NPT

ensemble by Langevin thermostat and Berendsen barostat [30] in the sampling time range of 1 nano-second after equilibrium. In addition, for the calculations of free energy and elastic constants, another 2 nano-seconds is applied for the adiabatic switching process [31] in the TI, based on the equilibrium spin and lattice configurations, in which both forward and backward processes [32] are performed with time-step of 1 femto-second. Doubling the integration time and increasing the simulation box to 54000 atoms resulted in the free energy variations within 2% and 1.5%, respectively.

5.4 Thermal Properties

5.4.1 Temperature dependence of the effective crystal potential

In a crystalline solid, the lattice atoms vibrate around their equilibrium positions, acted on by pair-wise and many-body forces from the surrounding atoms. The crystal potential experienced by the vibrating atoms at low temperatures and zero pressure may be assumed harmonic, with fixed restoring force constants. However, the amplitude of the atomic vibration increases as temperature increases, and one can no longer ignore the anharmonicity in the crystal potential, which leads to amplitude-dependence in the force constants and a temperature-dependent effective crystal potential. This is reflected in the temperature dependence of the phonon spectral frequencies and line broadenings

as discussed in Chapter IV. A contributing reason is the change of the equilibrium atomic volume, or thermal expansion [33].

With the participation of spins, the spin-lattice interaction via the exchange field gives rise to two effects, namely, (1) the change of the crystal potential to include the influence of the exchange field and (2) the interaction of the thermal excitations of the lattice and the spin. The first effect produces temperature dependence of the atomic volume via spin-spin correlation, while the second one increases energy dissipation due to scattering of the lattice and spin waves. For illustration, we plot in Fig. 5.1 the ground-state crystal potential at 0K as a function of atomic volume, with and without the exchange field.

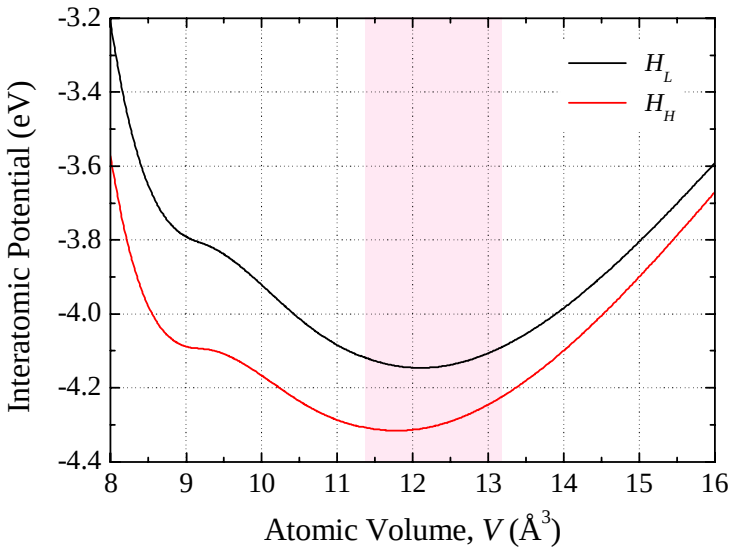

Fig. 5.1: The interatomic potentials in H_L and H_H (with time averaged spin-correlation at 0K) plotted as functions of atomic volume. The shaded area indicates the minimum region approximately, corresponding to the equilibrium atomic volume at finite temperatures.

Seen from Fig. 5.1, the exchange field provides an attractive component to the ground-state crystal potential, producing a contraction in the equilibrium atomic volume. An asymmetry in the force constant in regard to expansion and contraction of the atomic volume [34] is also apparent.

The same effect for the thermally excited states is shown in Fig. 5.2, in which the equilibrium atomic volume for H_H (with magnon excitation) and H_L (without magnon excitation) is plotted as a function of temperature.

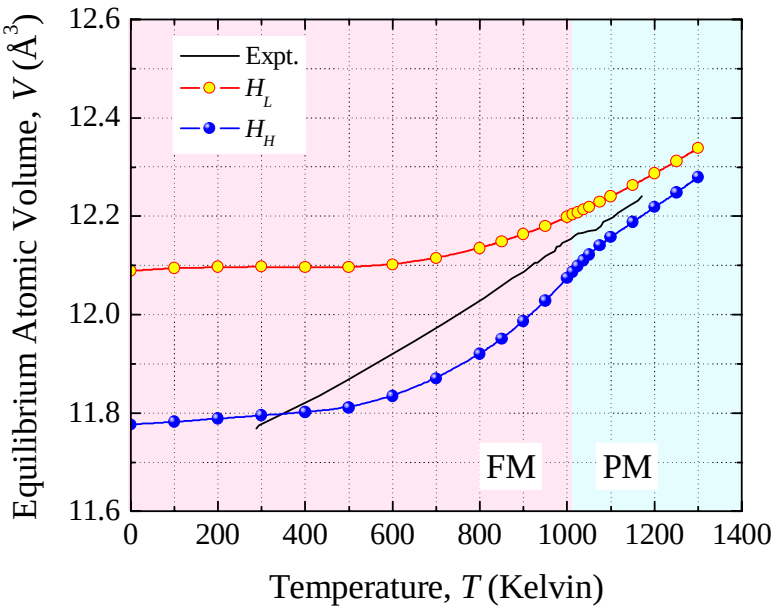

Fig. 5.2: The equilibrium atomic volume under the stress-free condition, with and without the magnon excitation. The results are compared to the experimental measurements done by Ridley and Stuart [35].

Comparison clearly shows volume contraction caused by the attractive exchange interaction between parallel spins [21]. At temperatures below 600K, the volume contraction is ~3% and is almost constant. At higher temperatures,

magnon softening (reduction of spin stiffness) leads to a loss of spin correlation when long-range magnetic order starts to disappear, with the reduction of the contraction from ~3% at 600K to less than 1% above the Curie temperature. The residual contraction is likely the result of the short-range magnetic order. Our results in Fig. 5.2 are in good agreement with the experimental data [35].

The second effect, one that is due to the enhanced dissipation caused by the increased scattering of the thermal excitations, namely, the lattice and spin waves, due to the spin-lattice interaction will be considered in the following subsections.

5.4.2 Thermal energy

The static and thermal energies of the systems for H_H, H_L and H_S under the stress-free condition are calculated and respectively plotted in Figs. 5.3 and 5.4, as functions of temperature. The lack of temperature dependence of E_0 for H_L is noted. It is due to the harmonicity of the DD potential. The temperature dependence of E_0 for H_H is relatively small but distinctly visible, particularly near the FM/PM phase transition. This shows that most of the temperature dependence of the atomic volume mainly comes from the inter-site exchange interaction, the strength of which is proportional to the temperature dependent spin correlation.

If atomic vibrations are simple harmonic, the total vibrational energy is given by $E_{\text{vib}} \equiv nk_{\text{B}}T/2$, according to the virial and equipartition theorems [36], where n is total degrees of freedom in the system [19], so that $E_{\text{vib}} = 3k_{\text{B}}T$ per

atom for the lattice subsystem and $E_{\text{vib}} = 1k_{\text{B}}T$ per atom for the spin subsystem. Due to anharmonicity, E_L and E_S in Fig. 5.4 are both larger than the respective simple harmonic values of $3k_{\text{B}}T$ and $1k_{\text{B}}T$. Similar to E_0, E_{vib} of the spin subsystem also shows much stronger temperature dependence than that of the lattice subsystem, particularly near the magnetic phase transition temperature. Indeed, comparing E_L with E_H in Fig. 5.4 shows that the excitation of magnons increases the total thermal energy by ~50%, contributing about a third of the total thermal energy. Comparing E_{L+S} with E_H identifies a thermal energy of about $0.3k_{\text{B}}T$ that can be attributed to the interaction between phonons and magnons near the magnetic phase transition. This is consistent with the enhanced phonon line broadening in this region discussed in Chapter IV.

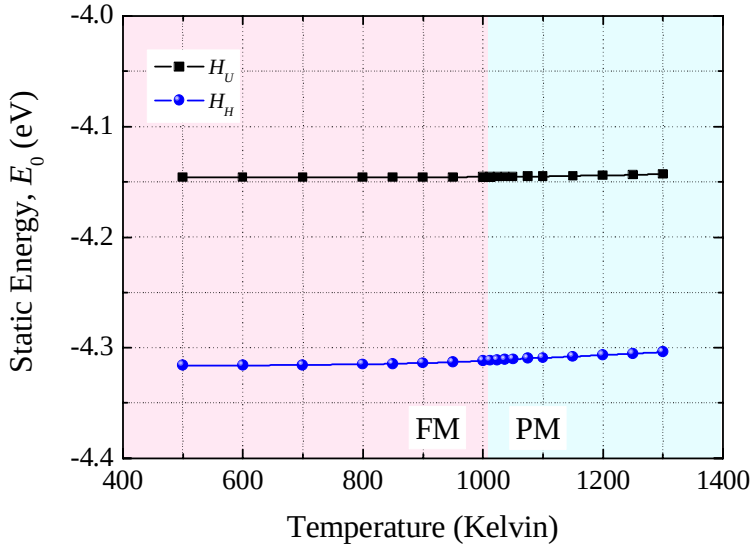

Fig. 5.3: The static energy E_0 of H_L and H_H at various temperatures, ranging from 500K to 1300K. The temperature dependence of E_0 comes from the change in equilibrium atomic volume under the stress-free condition.

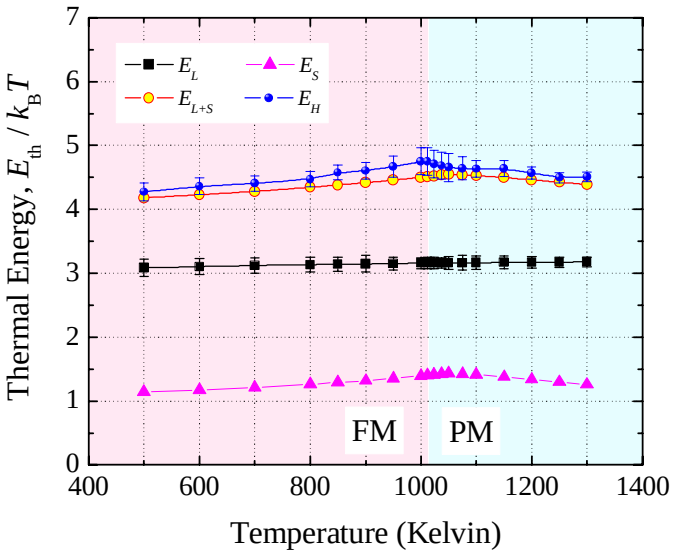

Fig. 5.4: The thermal energies in the unit of $k_B T$ as functions of temperature.

5.4.3 Grüneisen parameter

As discussed in Chapter II, anharmonicity of the crystal potential causes the frequencies of the lattice vibrations to depend on the equilibrium atomic volume V. To describe the resulting physical effects, the Grüneisen parameter for a vibration mode with frequency ω_i is defined as

$$\gamma_i = -\frac{\mathrm{d}\ln\omega_i}{\mathrm{d}\ln V}. \tag{5.19}$$

In non-magnetic materials, the Grüneisen parameter is completely determined by the lattice vibrations (phonons). Thermodynamically, under the quasi-harmonic approximation, the Grüneisen parameter can be shown to be related to thermal and mechanical properties of the solid, according to,

$$\gamma = \frac{\alpha V B_T}{C_V}, \tag{5.20}$$

where α and B_T are the thermal expansion coefficient and isothermal bulk modulus, respectively, which would be discussed in detail in the following sections; and C_V is the specific heat. However, in ferromagnetic materials, e.g. BCC iron, the free energy of the solid also contains contributions from the magnons (see Eq. 5.1d), which would therefore also show up in the Grüneisen parameter [20]. The magnetic Grüneisen parameter should describe the coupling among magnetic, thermal and elastic properties, such as magnetocaloric, magnetoelastic, and thermo-elastic properties.

However, an explicit expression of the magnetic Grüneisen parameter in a form similar to that in lattice dynamics, i.e. Eq. (5.20) is not available, awaiting further work. Fortunately, the Mie-Grüneisen equation, as introduced in Eq. (5.4), provides a possible approach to study the effects of spin vibrations on the Grüneisen parameter. Fig. 5.5 plots the calculated Grüneisen parameter as a function of temperature by using Mie-Grüneisen equation.

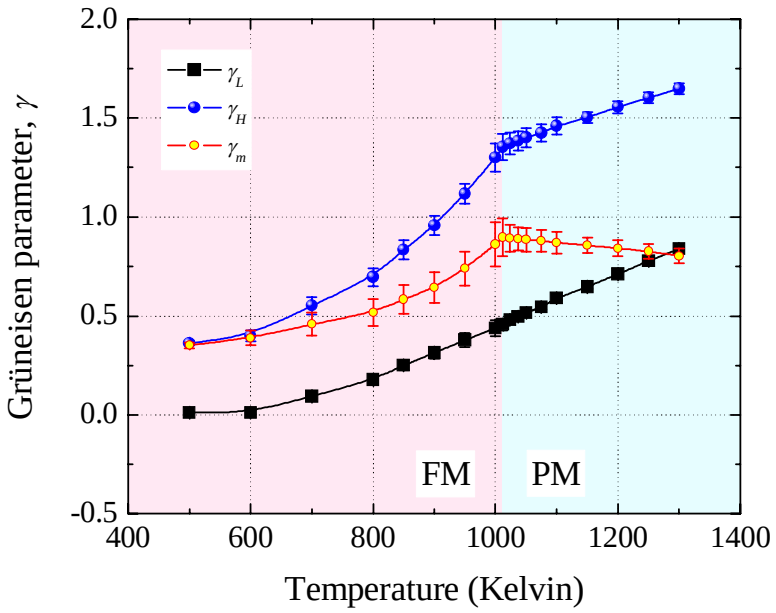

Fig. 5.5: The calculated Grüneisen parameter γ associated with H_L and H_H, the defined $\gamma_m = \gamma_H - \gamma_L$ represents contribution from the magnons.

In Fig. 5.5, γ_L and γ_H are respectively associated with H_L and H_H. γ_L measures the effect of lattice anharmonicity without the participation of spin dynamics, while γ_H includes the impact of magnons. The value of γ_L is smaller than 1 for the whole temperature range, which is relatively small compared to a normal value of between 1 and 3 in normal metals. This also points to the possibility that the restoring forces produced by the DD potential might have been overly linear. Indeed, this is consistent with our difficulty to produce the α/γ phase transition at the right temperature due to insufficient phonon softening. The values of γ_H are in general agreement with values for the Earth core derived from the seismic data (~1.8 [37] or ~1.4 [38]). We also plot $\gamma_m \equiv \gamma_H - \gamma_L$ in Fig. 5.5 to show the effect of the magnon phonon interaction. Physically,

contributions due to the spin dynamics are realized through the highly non-linear exchange field in the Heisenberg Hamiltonian. Compared with γ_L, it is clear that effects of magnon excitation, as expressed by γ_m is dominant throughout the entire temperature range examined. Since the amplitudes of lattice vibration increase with increasing temperature, the increase of γ_L with temperature is expected [39]. γ_m behaves similarly in the FM phase except for a much larger value at the lowest temperatures considered, where the amplitude of the lattice vibration is small. This is likely to be the result of the larger spin correlation at lower temperatures. Unlike γ_L, γ_m does not increase with temperature monotonically. It maximizes at T_C and starts to drop off as the long-range magnetic order disappears. Despite the increase of the mean phonon-energy, further temperature increase in the PM phase sees the reduction of γ_m.

It should be noted that the Mie-Grüneisen equation is derived based on the Einstein model in which all vibration modes share the same vibration frequency. Apparently, neglecting the distribution of vibrational spectrum is an assumption that might be oversimplified. In future work, we would try to calculate the magnetic Grüneisen parameter directly from the magnon spectra beyond the approximation in current calculation, which may provide more information about the effects of spin vibrations on thermal and mechanical properties in ferromagnetic materials.

Thermodynamically, the Grüneisen parameter can be derived from the following thermodynamic relation as shown in Eq. (5.20). However, Eq. (5.20) is based on the assumption that all the frequency changes with volume are equal. Fig. 5.6 shows the comparison of Grüneisen parameters obtained from Eq. (5.4) (abscissa axis) and Eq. (5.20) (ordinate axis). It can be seen that, the values of γ in H_H is generally consistent with each other, but the value of γ in H_L obtained from M-G equation is smaller than those from the thermodynamic relation as Eq. (5.20), which may result from the different assumption taken in these two methods.

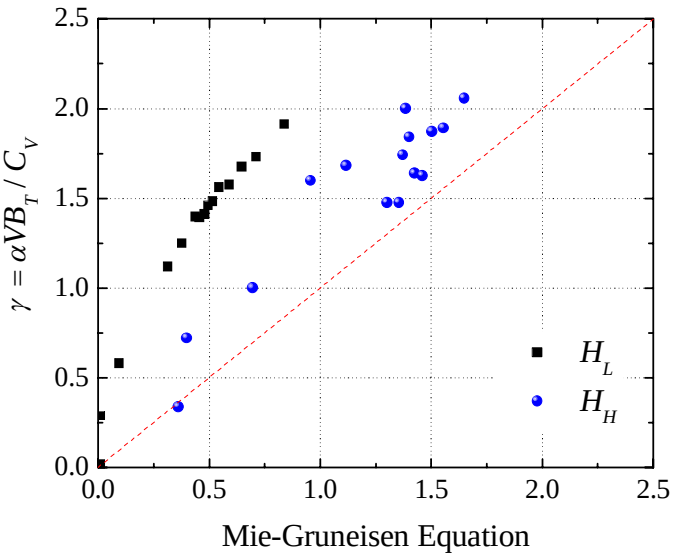

Fig. 5.6: The comparison of Grüneisen parameters obtained from Mie-Grüneisen equation as Eq. (5.4) (abscissa axis) and the thermodynamic relation as Eq. (5.20) (ordinate axis) of BCC iron in both case with (H_H, blue solid circle) and without (H_L, black solid squares) spin-vibrations. The red dashed line is the expected asymptote.

5.4.4 Thermal component of the free energy and entropy

From the calculated free energies (see Section 5.2) the thermal component F_{th} can be derived by subtracting off the static energy E_0. The results are plotted in Fig. 5.7 for various temperatures. The continuity of F_{th} throughout the entire temperature range confirms the second-order nature of the FM/PM transition, which is consistent with experiments and other calculations [13]. Noting the relatively small temperature-dependence of $E_{\text{th}} / k_{\text{B}}T$ (Fig. 5.4), it is obvious that most of the temperature dependence of $F_{\text{th}} / k_{\text{B}}T$ in Fig. 5.7 has to come from the entropy changes when the system is heated up [25].

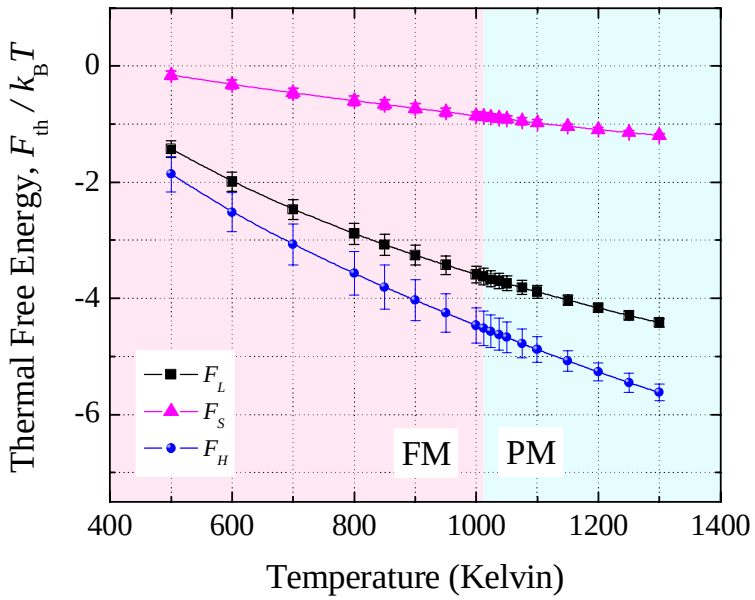

Fig. 5.7: The thermal free energy F_{th} in units of $k_{\text{B}}T$, obtained from $F_{\text{th}} = F - E_0$ with TI method.

The resulting entropies are plotted in Fig. 5.8. It is important to note that all

the entropies are temperature dependent, in contrast to the constant value usually assumed in many investigations. The entropy contribution S_S from magnon excitations doubles, for example, from $1.2\,k_B$ at 500K to $2.5\,k_B$ at 1300K. Comparison of S_{L+S} and S_H, on the other hand, shows that the increase of the total entropy due to phonon-magnon interaction decreases as the magnon softens and disappears with increasing temperature. For example, it is $\sim 1\,k_B$ at 500K, but practically disappears above 1200K.

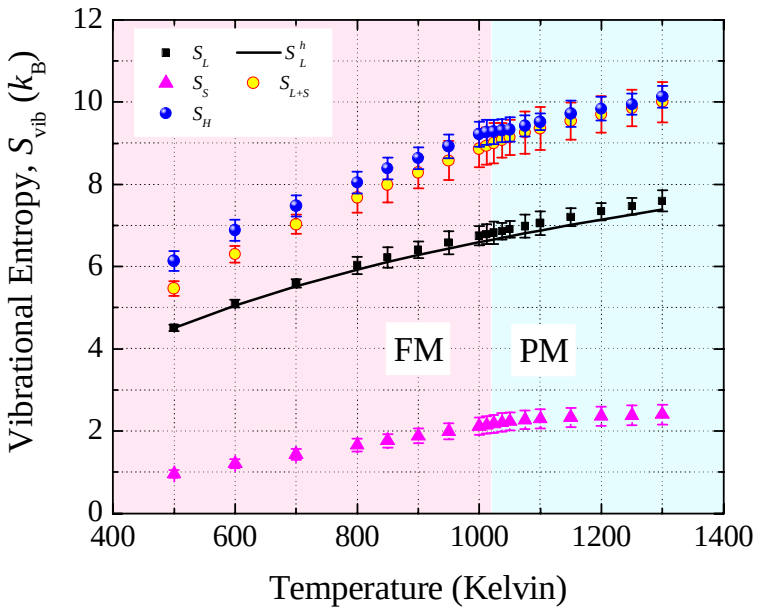

Fig. 5.8: The entropy S for various models. The solid line represents the Einstein Model (Eq. 5.21) using the entropy at 500K as reference and assuming the phonon modes is temperature independent.

The Einstein solid adopts the harmonic approximation, in which the atomic force constant is constant and the atomic vibration frequency is independent of

the lattice wave length. The corresponding entropy at temperature T can be expressed as $S(T) = S(T_0) + 3k_B \ln(T/T_0)$ [40], where $S(T_0)$ is the entropy at the reference temperature T_0. The increasing entropy with temperature comes from the increased phase-space volume sampled by the system as the vibration amplitude increases. Equivalently, the entropy increase comes from the increase in the number of phonon in the system. Accordingly, the entropy in the Einstein approximation for H_L is given by [40]

$$S_L^h(T) = S_L(T_0) + 3k_B \ln(T/T_0). \qquad (5.21)$$

Taking $T_0 = 500\text{K}$, the entropy in Eq. (5.21) is in good agreement with the calculated entropies from H_L in Fig. 5.8. Nevertheless, it is obvious that $S_L(T)$ has a slightly stronger temperature dependence due to phonon softening (see Eq. 2.60b). Comparison between H_{L+S} and H_H clearly shows the effect of phonon-magnon interaction in increasing the entropy due to the increased scattering. Reduction of the effect due to the disappearance of the long-range spin correlation is also apparent, when system crosses over from the FM phase to the PM phase.

Unlike the lattice system, the energy E_S and entropy S_S of a ferromagnetic spin system are both monotonic functions of temperature, so that S_S can be expressed as a function of E_S, as commonly done in literatures [41,]. In Fig. 5.9, S_S is plotted as a function of the reduced magnetic energy $E_S / |E_S^0|$,

E_S^0 being the energy of spin system at ground state (0K).

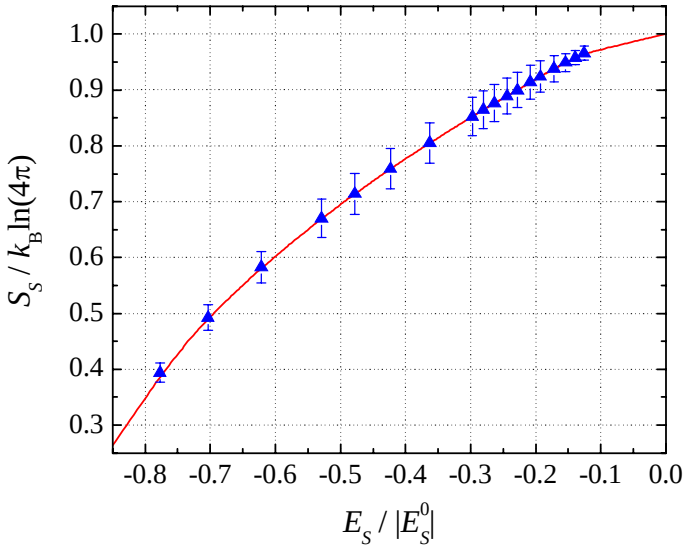

Fig. 5.9: The entropy of spin system plotted as function of reduced magnetic energy.

Since the spin system is totally disordered at sufficiently high temperatures, we must have $\lim_{T\to\infty} E_S = 0$. The high-temperature limit of S_S in a classical vector model is $\lim_{T\to\infty}\left(S / k_B\right) = \ln\left(4\pi\right)$, as expressed in Eq. (2.119) [40]. This is consistent with our results in Fig. 5.9. In Fig. 5.10, we plot $\left(\partial S_S / \partial E_S\right)^{-1}$ against T and verify their equality, thus confirming the thermodynamic relation $\left(\partial S_S / \partial E_S\right) = 1/T$ in our results.

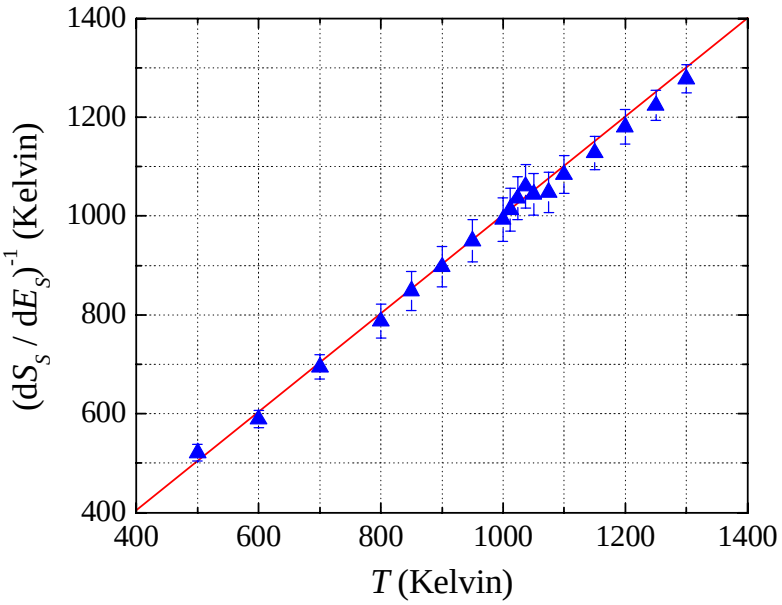

Fig. 5.10: The calculated $\left(\partial S_S / \partial E_S\right)^{-1}$ against T for verifying the thermodynamic relation $\left(\partial S_S / \partial E_S\right) = 1/T$ in our results. The solid line is the expected asymptote.

5.4.5 Specific Heat

Fig. 5.11 shows the specific heats of the lattice system H_L, the spin system H_S and the Heisenberg particle system H_H, respectively calculated by differentiating the corresponding the thermal energy E_{th} in Fig. 5.4, as a function of temperature.

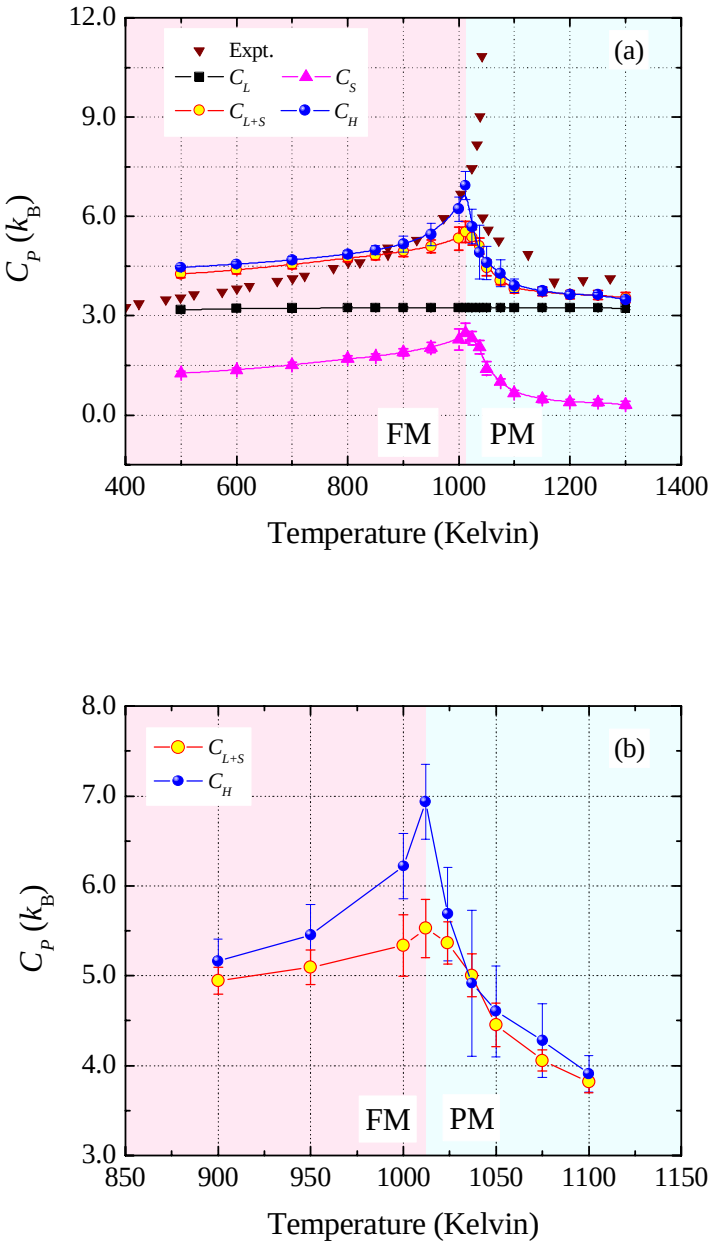

Fig. 5.11: The specific heat (a) in various models, experimental measurement [3,4] are plotted for comparison; (b) the enlarged region near Curie temperature.

Our spin system only has two degrees of freedom, so that the specific heat of the classical spin system far away from the transition point is about $1\,k_B$ in the FM phase and tends to zero in the PM phase due to the loss of long-range spin

correlation [19,42]. These characteristics are reflected in the calculated C_S in Fig. 5.11(a), which measures the heat capacity due to magnon excitations. The lattice specific heat C_L due to phonon excitations, on the other hand, is nearly flat in the whole temperature regime, with a value only slightly larger than the classical value of $3k_B$ [19,20] arising from a small amount of multi-phonon interactions. C_H contains contributions from thermal excitations due to both magnons and phonons, including effects due to their mutual interaction.

The difference of the specific heats C_H of the Heisenberg particle system and C_{L+S} in Fig. 5.11(b), is due to the interaction between the phonons and magnons. In this regard, C_H and C_{L+S} show good consistency with each other in the whole temperature regime except near the FM/PM transition, where slowing down of the spin vibrations [29] brings the frequencies of the magnons sufficiently close to those of the lattice vibrations. We note that, even with the Heisenberg model, the calculated values are only about half of the experimental values [3,4]. This may be due to the inadequacy of the simple model of the exchange function [14] we used in this work.

5.5 Thermomechanical Properties

In the foregoing sections, we have seen how the participation of spins can affect the free-energy change of atomic processes in a ferromagnetic metal like BCC iron. The participation of the exchange field can alter the free-energy

change of the process, by changing the effective crystal potential, particularly the anharmonicity. The participation of magnons in atomic processes may also change the entropic contributions from the phonons due to magnon-scattering. In this regard, magnon softening due to FM/PM phase transition will produce changes in all related lattice properties in BCC iron. Magneto-volume and magneto-elastic phenomena are typical examples, which will be discussed in the following.

5.5.1. Magneto-volume effect

The magneto-volume effect is the volume change of a crystalline solid, caused by spontaneous magnetic transition or forced by an external magnetic field. This effect is characterized by the anomalous temperature dependence of the thermal expansivity near the FM/PM phase transition.

Experimentally, Joule [43], in 1842, first reported such effects in the length of ferromagnetic rods. One of the important applications of magneto-volume effects is Invar alloy [44,45,46,47], such as quenched FCC $Fe_{65}Ni_{35}$, whose thermal expansion coefficient is near zero in a wide range of temperatures. Based on the experimental data, Lee [48], as well as Campbell and Creuzet [49], gave a comprehensive review for magneto-volume effects caused by local moments and other mechanisms. For systems with strong local moments, such as iron and nickel, Moriya and Usami [50] demonstrated that it is the local moments effect

that dominates the magneto-volume behavior, rather than itinerant electrons.

In addition to the empirical descriptions of magneto-volume effects, theoretical models had also been developed in the last few decades. For instance, Callen and co-workers [51,52] proposed a standard model based on quantum mechanics to describe the magneto-volume effects in ferromagnetic materials, involving interactions between phonon and magnon excitations at low temperatures. However, it is expected that the coupling between phonon and magnon excitations are strong at high temperatures, especially near the FM/PM phase boundary [53].

The role of magnon excitations in magneto-volume effects can be understood from a thermodynamic point of view [54]. Energetic and entropic contributions to the free-energy of the atomic ensemble, arising from both phonons and magnons and their mutual interactions, can be obtained from atomistic simulations. In previous atomistic calculations [55,56] based on the mean-field approximation, the spin degrees of freedom are adiabatically [1,1] decoupled from the lattice system, and the dependence of the exchange field on atomic environment is realized only in a time-averaged sense by assuming a uniform lattice expansion [57,58,59]. In such treatments, the dynamic nature of the atomic positions and the effects of spin dynamics are neglected.

Grossmann and Rancourt [60] recently proposed a microscopic approach to

account for the magneto-volume effect, in which molecular dynamics (MD) simulation for the lattice vibration was combined with Monte Carlo (MC) simulation for Ising-model-based spin dynamics. Nevertheless, the magnetic effects on lattice dynamics are still adiabatically treated as a perturbation and the motions of spin and lattice are not solved on equal footing. The entropic contribution due to the coupling of spin and lattice cannot be described appropriately, which is believed to be important in determining the mechanical properties at higher temperatures, i.e. near Curie temperature.

To examine the role of magnon excitations in the magneto-volume effect, we calculate the corresponding thermal expansivity following Eq. (5.5) from the equilibrium atomic volumes of BCC iron under stress-free conditions, with and without the influences of magnon excitations, at temperatures across the FM/PM phase boundary (See in Fig. 5.2). The results are plotted in Fig. 5.12, together with the experimental measurements [35]. Here, α_L is derived from H_L, reflecting the thermal expansivity due to pure phonon effects caused by the anharmonic nature of DD potential [17] used in our simulations. In this case, the strength of anharmonicity increases steadily with increasing temperature as the phonon density increases with the amplitude of the lattice vibrations. A similar trend can also be found in the curve of α_H derived from H_H, involving the influence of magnon excitations, except near the FM/PM phase boundary (~1020K in current calculation), in which α_H first increases with temperature,

reaching a maximum value around $80\times10^{-6}/\mathrm{K}$, then drops off to a around $45\times10^{-6}/\mathrm{K}$ in the boundary of PM phase, before finally increasing again to a constant value around $53\times10^{-6}/\mathrm{K}$ at 1300K.

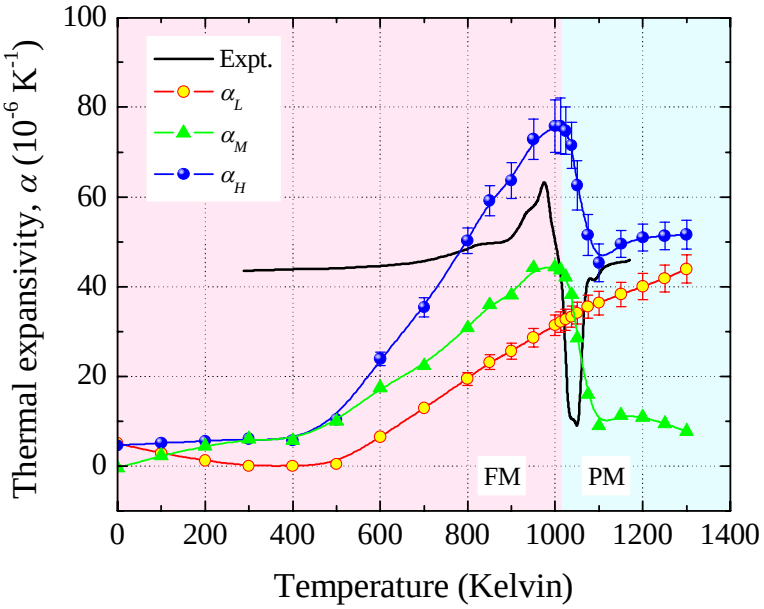

Fig. 5.12: The thermal expansion coefficients α_L and α_H obtained from the Hamiltonians H_L and H_H, respectively, with α_M is simply defined by $\alpha_M = \alpha_H - \alpha_L$. The black solid line is the thermal expansion coefficient derived from the experimental measurements [35].

Seen from Fig. 5.12, the temperature dependence of our calculated α_H is generally comparable with the experimental data [35]. The contribution from the magnetic excitation can be seen from the quantity $\alpha_M = \alpha_H - \alpha_L$. The anharmonicity caused by the participation of magnons is of the same order of magnitude as that caused by pure phonon-phonon interactions in the FM phase. The non-zero value of α_M in the PM phase reveals the existence of short range

magnetic order, which has been confirmed as persisting by neutron scattering experiments [61,62].

In this regard, the accelerated increase of thermal expansivity in ferromagnetic iron near the FM/PM phase boundary can be understood as the result of the enhanced phonon scattering by magnons with lowered frequencies, where the disappearance of long-range magnetic order gives rise to an abrupt decrease of thermal expansion coefficients. It should be noted that the current calculations only involve the effects due to the spontaneous magnetic phase transition in ferromagnetic material. Such effects can also arise from applied external magnetic field on magneto-volume (also named *Joule's magnetostriction* in literatures).

5.5.2. Magneto-elastic effect

We have seen the enhancement effect of magnons on the anharmonicity of BCC iron in the foregoing sections, such as the anomalous temperature dependence of thermal expansivity and Grüneisen parameter. Another important consequence of anharmonic effect on mechanical properties is the temperature dependence of the elastic constants [34]. The effect of magnetic state on the elastic properties falls under the namely magneto-elasticity, which is the subject of our study in the present section.

As discussed in the foregoing section, the isothermal elastic constants correspond to the resistance to the isothermal straining processes, during which the system suffered an applied small strain in the elastic region. The corresponding free energy change consists of three parts, namely (1) the static energy change due to the lattice distortion [26]; (2) the thermal energy change arising from the frequency shift of elementary excitations [18], such as phonon or magnon in ferromagnetic materials; and (3) the heat dissipation in term of entropy change, associated with the relaxation of elementary excitations. For harmonic vibrations, the frequencies of thermal excitations are independent of the atomic volume [18], and the changes of both thermal energy and entropy are negligible, so that the principal contribution to the strain free energy is arising from the static strain energy. The elastic constants derived from strain energies alone are called *adiabatic* elastic constants [63]. As expected, due to the participation of magnon excitations in ferromagnetic materials, the heat dissipation, arising from the scattering between phonons and magnons, has to be taken into account, especially near the FM/PM phase boundary. In this regard, the isothermal elastic constants can be treated as important indicators of anharmonicity due to the magnetic effects in ferromagnetic materials.

Calculating the free energy with sufficient accuracy is a challenging task. This is the static strain energy is customarily used for the calculation of elastic constants in the literature [64,65,66], despite missing the entropic contribution.

Consequently, the adiabatic elastic modulus is calculated rather than the isothermal one, which is consistent with the experimental one only at 0K or within the harmonic approximation [19]. Another challenge of calculating isothermal elastic constants BCC iron is the lack of appropriate simulation scheme treating the spin and lattice degrees of freedom in a self-consistent framework [60]. In the following, we present our results by using the SLD [14] simulations based on the modified TI method (See in Section 5.2.5).

Fig. 5.13 shows the resistant force $Y(\delta)$ and the hydrostatic strain free energy $F(\delta)$ as a function of strain δ at 900K without (Fig. 5.13a) and with (Fig. 5.13b) magnons. Seen from Fig. 5.13, the relation between $Y(\delta)$ and δ is closely linear, particularly when $|\delta| \to 0$. For values of $|\delta| > 10^{-2}$ outside the elastic region, the relation shows a small downward curvature. The free energy $F(\delta)$ is basically a quadratic function of δ at the elastic region. Higher-order terms can be seen to appear for larger strains in the inelastic region. Comparing with the quadratic fitting curve in Fig. 5.12 from which the isothermal bulk modulus is derived following Eq. (5.10), it is interesting to note that $F(\delta)$ is asymmetric to contraction and expansion.

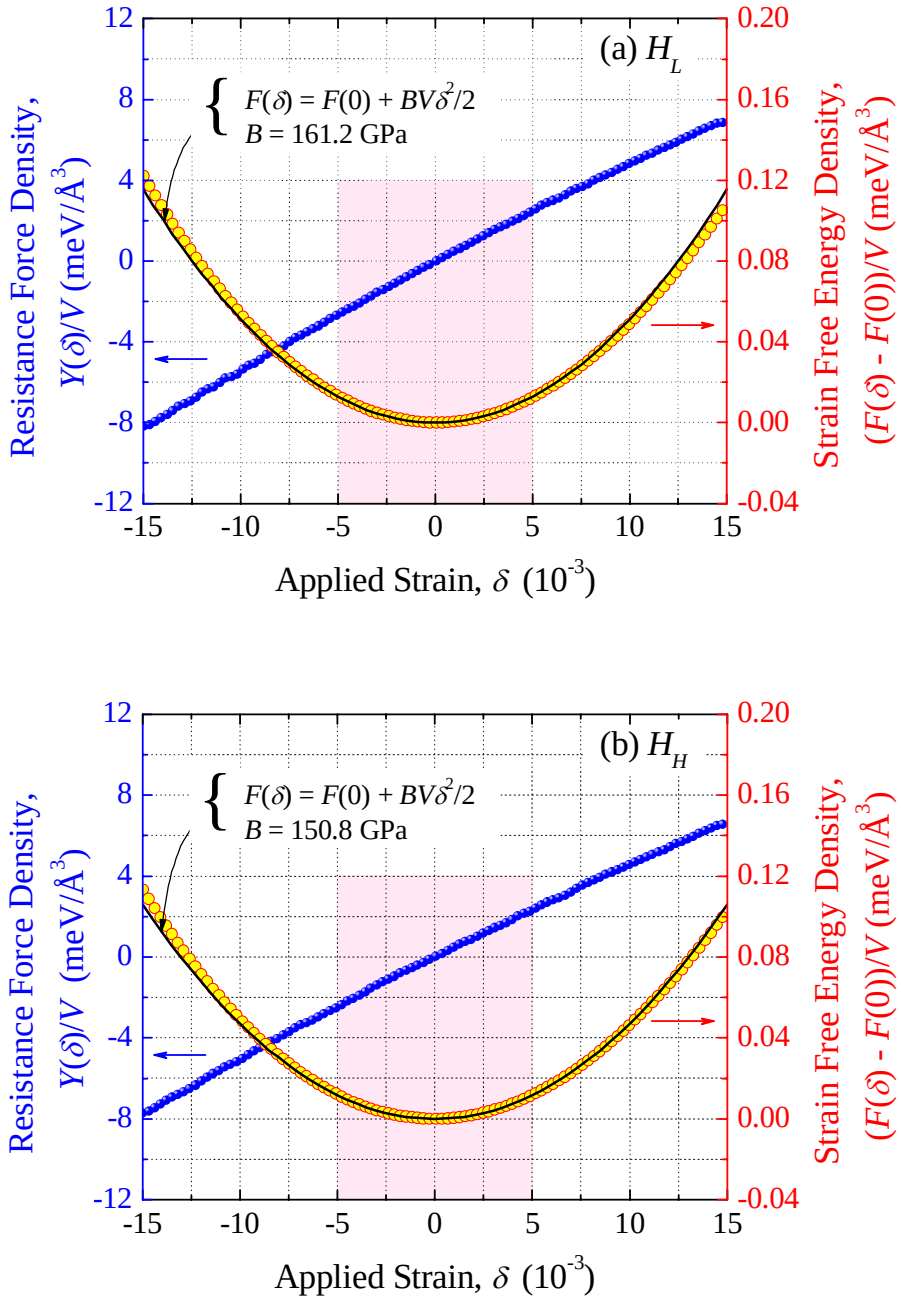

Fig. 5.13: The calculated resistance force (Solid circles) and the corresponding strain free energy (Open circles) at various applied strain on the designed path for the system, (a) without and (b) with the influence of magnon excitations for BCC iron at 900K. The solid lines represent the least squared quadric fitting in the range of $-5\times10^{-3} < \delta < 5\times10^{-3}$ (Shaded region) by following Eq. (5.10), respectively, with the values of B as ~161.2GPa and ~150.8GPa.

The isothermal bulk modulus B is calculated as a function of temperature,

with and without spin vibrations, and plotted in Fig. 5.14. Without magnons, the value of B decreases almost linearly with increasing temperature, from ~170GPa at 300K to ~155GPa at 1300K. According to lattice dynamics, such a negative temperature dependence is the result of phonon softening due to anharmonicity of crystal potential, which is consistent with the calculated phonon dispersion curves presented earlier in Chapter IV. On the other hand, with the participation of magnons, the calculated bulk modulus shows a much stronger temperature dependence at temperatures above 600K. In Fig. 5.14, B gradually decrease with increasing temperature, reaching a minimum (~140GPa) near the Curie temperature (~1020K), and then increases in the PM phase, with values comparable to the calculated results of H_L. Compared to the experimental measurements of Dever [67], the current calculated results are quantitatively in good agreement in the FM phase, whereas the larger value of the data in the PM phase is probably a result of the inaccuracy of the DD potential [17] in the anharmonic region, which fails to reproduce the phonon softening near the BCC-FCC phase boundary, i.e. 1183K [9].

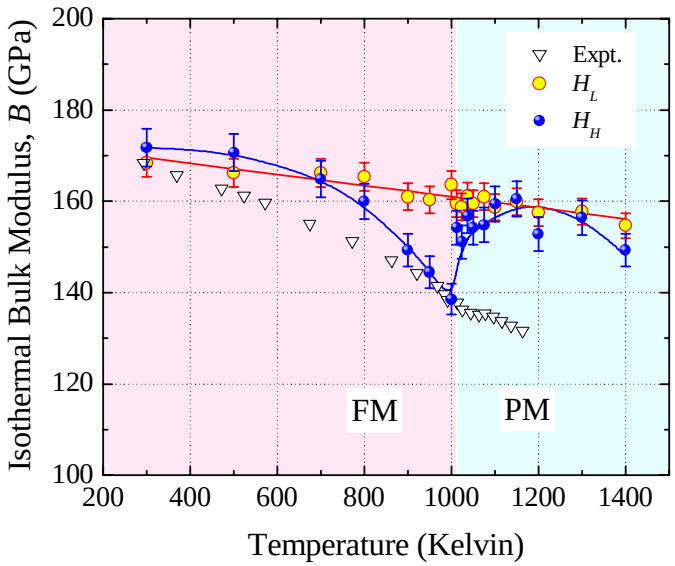

Fig. 5.14: The temperature dependence of isothermal bulk modulus calculated by using modified thermodynamic integration method from H_L and H_H respectively, comparing with the experimental measurement done by Dever [67]. The solid lines are guides for eye.

In addition, the values of B calculated from the magnetic Hamiltonian H_H are smaller than that of H_L in the temperature range considered and such difference reaches a maximum ($\approx 20\text{GPa}$) near the Curie temperature as shown in Fig. 5.14. As stated in the previous section, three components contribute to the free energy during the isothermal straining process. However, the difference between the thermal energy changes should be negligible due to the isothermal condition [18]. In addition, the static strain energy difference between H_L and H_H is expected to have the same temperature dependence as the spin thermal energy, which is positive. Consequently, it is reasonable to speculate that the negative downward cusp in the temperature dependence of B with magnons is mainly due to heat dissipation, associated with the relaxation of spin

configuration during the hydrostatic deformation process.

The tetragonal shear modulus c' is plotted in Fig. 5.15, in which the values of H_L and H_H more than doubles the experimental values in the temperature region from 300 to 1300K. This is expected, since c' tending to be zero at temperatures higher than T_C, reveals the softening of phonon modes along $[110]$ direction, which is typical of the structural phase transition from BCC to FCC at 1183K [68]. However, as stated earlier in the foregoing paragraph, the DD potential [17] used in our simulations does not produce such a phase transition, even at higher temperature. In addition, the temperature dependence of c' is consistent with experimental results [67]. The magnetic effect brings about a negative contribution to c' in the FM phase by comparing H_H to H_L, which gradually decreases with temperature increase. As discussed in bulk modulus, this magnetic contribution can be regarded as effects on the strain energy during the isochoric deformation process, by changing the force constant suffered by the atomic lattice. Due to the disappearance of the long range magnetic order in the PM phase, c' of H_H is almost equal to that of H_L, revealing that the short range magnetic order has no contribution to the free energy change during the isochoric deformation process.

A similar phenomenon can also be seen in the temperature dependence of orthorhombic shear modulus c_{44}, plotted in Fig. 5.16, in which c_{44} of both H_L

and H_H is almost constant in the PM phase, with a value of ~98GPa, which is comparable with the experimental data [67]. Compared to the results of H_L, the magnon excitations involved in H_H result in a steeper decreasing trend in the FM phase, i.e. from ~110GPa at 300K to ~100GPa at 1000K. In contrast to c', magnons gives rise to a positive contribution to c_{44} as shown in the difference of c_{44} between H_L and H_H in Fig. 5.16. Interpreted by Dever [67], such converse contributions to c' and c_{44} due to spin order is from the different dependence on strains between tetragonal and orthorhombic shear deformations.

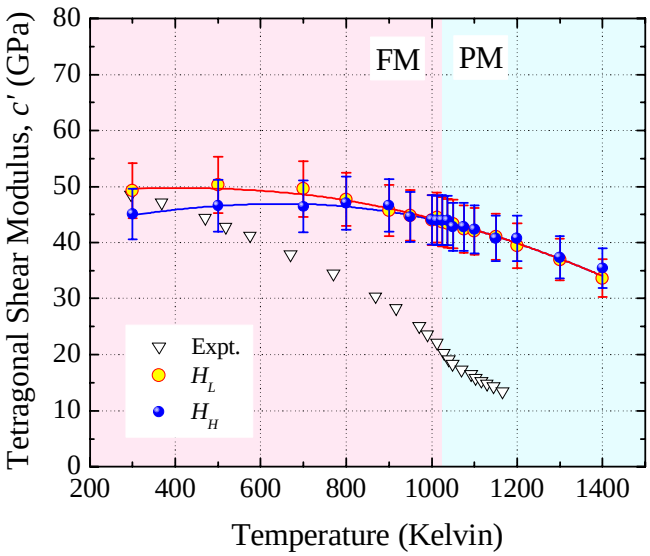

Fig. 5.15: The temperature dependence of tetragonal shear modulus in BCC iron, by comparing with the experimental measurement [67]. The solid lines are guides for eye.

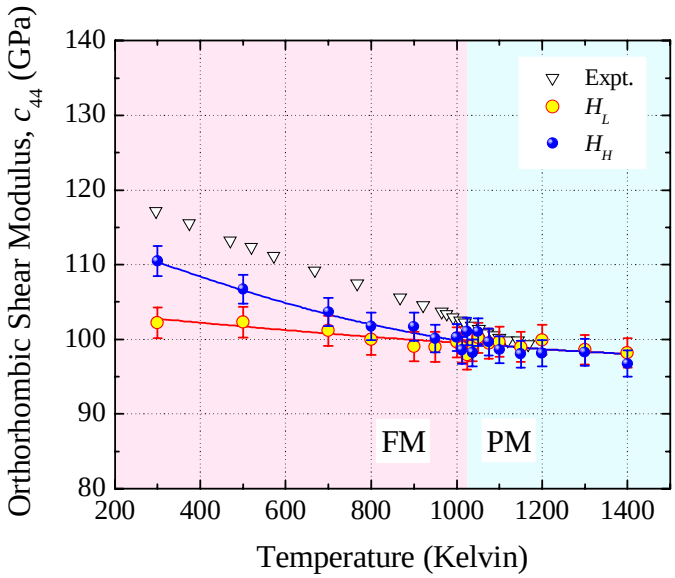

Fig. 5.16: The temperature dependence of orthorhombic shear modulus in BCC iron, by comparing with the experimental measurement [67]. The solid lines are guides for eye.

5.6 Brief Conclusion

The atomistic study of effects of magnon excitations on thermal, magnetic and mechanical properties of BCC iron is performed within the SLD framework, where an isotropic interatomic-distance dependent exchange integral is introduced to describe the coupling of spin and lattice. The associated quantities are calculated from the phase-space trajectories generated via MD, SD and SLD simulations, in which atoms are modeled as Heisenberg particles, involving phonons, magnons, and their interactions.

The second order nature of the FM/PM phase transition, for instance, the continuity of free energy, and the divergence of heat capacity near Curie

temperature, is revealed in our results.

The interaction between vibrations of the lattice and the spins introduce additional anharmonicity of the crystal potential. This has appreciable effects on lattice properties near the FM/PM phase transition region, such as thermal expansion, temperature dependence of the specific heat and isothermal elastic constants. Our results are in good agreement with either the theoretic predictions or experimental measurements.

Indeed, due to the atomic-distance dependent exchange integral, the excitation of magnons gives rise to the enhancement of phonon-scattering, especially near FM/PM phase boundary. Such magnetic effects significantly change the anharmonicity of BCC iron. For instance, the Grüneisen parameter, thermal expansivity and specific heat all show anomalous temperature dependence near FM/PM phase boundary. Moreover, the contributions from magnon excitations are practically large comparable with that due to the pure phonon-phonon interactions.

In this chapter, the role played by magnon excitations in the temperature dependence of isothermal elastic constants has been studied. During the hydrostatic straining process, the heat dissipation arising from dynamical relaxation of magnon excitations gives rise to a negative contribution to the strain free energy, and plays the principal role in the temperature dependence of bulk

modulus, which is a typical example of magneto-elastic effects. In the isochoric deformation processes, the spin order changes the force constant between lattice atoms, and the resulting strain energy due to the lattice distortion is regarded as the main contribution to the strain free energy, whereas the heat dissipation associated with the entropic change is almost negligible in determining the temperature dependence of shear moduli. The short-range magnetic order has little appreciable effects on the shear modulus.

In conclusion, the participation of magnons in BCC iron causes the magnon-phonon interaction, and changes the properties related to lattice dynamics, e.g. thermal expansion and elastic constants. At the meanwhile, the magnon itself also gives extra contributions to the thermodynamic properties of the whole coupled system, e.g. the free energy and entropy.

Reference

[1] N. W. Ashcroft and N. D. Mermin, *Solid State Physics* (Saunders College, Philadelphia, 1976).

[2] D. C. Wallace, *Thermodynamics of Crystals* (Dover, New York, 1998).

[3] D. C. Wallace, P. H. Sidles, and G. C. Danielson, J. Appl. Phys. **31**, 168 (1960).

[4] Y. S. Touloukian, and E. H. Buyco, *Thermophysical Properties of Matter* (IFI/Plenum, New York-Washington, 1970) Vol. 4.

[5] G. Inden, *Project Meeting CALPHAD V, 21-25 June 1976*, (Max-Planck Inst. Eisenforschung, Düsseldorf, W. Germany, 1976), pp. III.4/1-III.4/13.

[6] G. Inden, Physica, **103B**, 82 (1981).

[7] M. Hillert, and M. Jarl, CALPHAD **2**, 227 (1977).

[8] Y.-Y. Chuang, R. Schmid, and Y. A. Chang, Metall. Trans. A **16A**, 153 (1985).

[9] M. Yu. Lavrentiev, D. Nguyen-Manh, and S. L. Dudarev, Phys. Rev. B **81**, 184202 (2010).

[10] A. Richter, M. Pleimling, and A. Hüller, Phys. Rev. E **71**, 056705 (2005).

[11] E. G. Moroni, and T. Jarlborg, Europhys. Lett. **33**, 223 (1996).

[12] U. Pinsook, Phys. Rev. B **66**, 024109 (2002).

[13] F. Körmann A. Dick, B. Grabowski, B. Hallstedt, T. Hickel, and J. Neugebauer, Phys. Rev. B **78**, 033102 (2008).

[14] P.-W. Ma, C. H. Woo, and S. L. Dudarev, Phys. Rev. B **78**, 024434 (2008).

[15] D. Frenkel, and A. J. C. Ladd, J. Chem. Phys. **81**, 3118 (1984).

[16] G. Ciccotti, D. Frenkel and I. R. McDonald, *Simulation of Liquids and Solids: Molecular Dynamics and Monte Carlo Methods in Statistical Mechanics* (North-Holland, Amsterdam, 1987).

[17] S. L. Dudarev, and P. M. Derlet, J. Phys.: Condens. Mat. **17**, 7097 (2005).

[18] G. Leibfried, and W. Ludwig, Solid State Physics **12**, 275 (1961).

[19] M. Born and K. Huang, *Dynamical Theory of Crystal Lattices*, (Oxford University Press, London, 1954), pp. 38-60.

[20] M. Born, *Atomtheories des festen Zustandes* (2nd, ed., Teubner, 1923), pp. 652; E. Grüneisen, *Handb. der Phys.*, **10**, 22 (Springer, 1926).

[21] H. J. C. Berendsen, J. P. M. Postma, W. F. Van Gunsteren, A. Di Nola and J. R. Haak, J. Chem. Phys. **81**, 3684 (1984).

[22] A. H. Carter, *Classical and Statistical Thermodynamics*, (Prentice-Hall, Inc., New Jersey, 2001), pp. 37-40.

[23] J. E. Hunter III, W. P. Reinhardt, and T. F. Davis, J. Chem. Phys. **99**, 6856 (1993).

[24] D. E. Gray (Editor), *American Institute of Physics Handbook*, 3rd ed. (McGraw-Hill, New York 1972), pp. 4-115.

[25] H. Ibach and H. Lüth, *Solid-State Physics: An Introduction to Principles of Material Science*, 4th Ed., (Springer, Germany, 2009), pp. 94-103.

[26] L. D. Landau and E. M. Lifshitz, *Theory of Elasticity*, 3rd Ed., (Elsevier, Singapore, 1999) pp. 1-37.

[27] W. F. Brown, Jr., Phys. Rev. **130**, 1677 (1963).

[28] N. Hatano, and M. Suzuki, Lect. Notes Phys. **679**, 37 (2005).

[29] B. I. Halperin, and P. C. Hohenberg, Phys. Rev. **177**, 952 (1969).

[30] H. J. C. Berendsen, J. P. M. Postma, W. F. Van Gunsteren, A. Di Nola, and J. R. Haak, J. Chem. Phys. **81**, 3684 (1984).

[31] M. Watanabe, and W. P. Reinhardt, Phys. Rev. Lett. **65**, 3301 (1990).

[32] M. de Koning, and A. Antonelli, Phys. Rev. E **53**, 465 (1996).

[33] G. C. Fletcher, Au. J. Phys. **14**, 420 (1961).

[34] C. Kittel, *Introduction to Solid State Physics*, 8th ed. (John Wiley & Sons, New York, 2005), pp. 120.

[35] N. Ridley, and H. Stuart, Brit. J. Appl. Phys. **1**, 1291 (1968).

[36] F. W. Sears, and G. L. Salinger, *Thermodynamics, Kinetic Theory, and Statistical Thermodynamics*, 3rd ed. (Addison-Wesley Publishing Company, Inc. 1975), pp 264-266.

[37] J. Ramakrishnan, R. Boehler, G. H. Higgins, and G. C. Kennedy, J. Geophys. Res. **83**, 3535 (1978).

[38] F. D. Stacey, and P. M. Davis, Phys. Earth Planet. Int. **142**, 137 (2004).

[39] J. E. Hunter III, W. P. Reinhardt, and T. F. Davis, J. Chem. Phys. **99**, 6856 (1993).

[40] R. K. Pathria, *Statistical Mechanics*, 2nd ed. (Butterworth-Heinemann, Oxford, UK, 1996), pp. 66-77.

[41] A. J. Guttmann, in *Phase Transitions and Critical Phenomena*, edited by C. Domb and J. Lewovitz (Academic Press, New York, 1989). Vol. 13.

[42] B. Bernu, and G. Misguich, Phys. Rev. B **63**, 134409 (2001).

[43] J. Joule, Sturgeon's Annals of Electricity **8**, 219 (1842).

[44] M. Shiga, in *Materials Science and Technology*, edited by R. W. Cahn, P. Hassen, and E. J. Kramer (VCH, Weinheim, 1993), pp. 159.

[45] M. Dubé, P. R. L. Heron, and D. G. Rancourt, J. Magn. Magn. Mater. **147**, 122 (1995).

[46] M.-Z. Dang, M. Dubé, and D. G. Rancourt, J. Magn. Magn. Mater. **147**, 133 (1995).

[47] M.-Z. Dang, and D. G. Rancourt, Phys. Rev. B **53**, 2291 (1996).

[48] E. W. Lee, Rept. Prog. Phys. **18**, 185 (1955).

[49] I. A. Campbell and G. Creuzet, in *Metallic Magnetism*, edited by H. Capellmann, (Springer-Verlag, Berlin, 1986), p. 207.

[50] T. Moriya, and K. Usami, Solid State Commun. **88**, 911 (1993).

[51] E. R. Callen, and H. B. Callen, Phys. Rev. **129**, 578 (1963); **139**, A455 (1965).

[52] E. R. Callen, J. Appl. Phys. **39**, 519 (1968), and the reference therein.

[53] H. Wang, P.-W. Ma, and C. H. Woo, Phys. Rev. B **82**, 144304 (2010).

[54] M. Mantina, Y. Wang, R. Arroyave, L. Q. Chen, and Z. K. Liu, Phys. Rev. Lett. **100**, 215901 (2008).

[55] M. E. Lines, Solid State Commun. **22**, 75 (1977).

[56] R. C. O'Handley, and C.-P. Chou, J. Appl. Phys. **49**, 1659 (1978).

[57] C. P. Been, and D. S. Rodbell, Phys. Rev. **126**, 104 (1962)

[58] A. J. Holden, V. Heine, and J. H. Samson, J. Phys. F **14**, 1005 (1984).

[59] E. Z. Valiev, and A. Z. Menshikov, J. Magn. Magn. Mater. **46**, 199 (1984).

[60] B. Grossmann, and D. G. Rancourt, Phys. Rev. B **54**, 12294 (1996).

[61] M. K. Wilkinson, and C. G. Shull, Phys. Rev. 103, 525 (1956).

[62] J. W. Lynn, Phys. Rev. B **11**, 2624 (1975).

[63] B. B. Karki, G. J. Ackland, and J. Crain, J. Phys.: Condens. Matter **9**, 8579 (1997).

[64] P. Söderlind, O. Eriksson, J. M. Wills, and A. M. Boring, Phys. Rev. B **48**, 5844 (1993).

[65] O. Gülseren, and R. E. Cohen, Phys. Rev. B **65**, 064103 (2002).

[66] M. H. G. Jacobs, and R. Schmid-Fetzer, Phys. Chem. Minerals **37**, 721 (2010).

[67] D. J. Dever, J. Appl. Phys. **43**, 3293 (1972).

[68] E. C. Bain, Trans. A.I.M.E. **70**, 25 (1924).

CHAPTER VI

EFFECTS OF SPIN VIBRATIONS IN SELF- AND MONO-VACANCY DIFFUSION

The change of the self-diffusion activation energy of BCC iron across the FM/PM phase boundary is a well-known phenomenon. While this has long been suggested to be due to the magnetic effect on the activation process, mechanistic details have yet to be developed. In this Chapter, the role played by spin dynamics on the activation of vacancy diffusion is considered by performing atomistic simulations of the migration of a single vacancy in BCC iron across the FM/PM phase boundary using spin-lattice dynamics, allowing active participations of the interacting dynamics of the lattice atoms and spins. Effects due to the spin dynamics on vacancy formation and migration processes are monitored and analyzed with corresponding lattice-only and spin-only calculations. We find that spin vibrations play a very important role in the thermodynamics of the atomic processes involved with vacancy formation and migration, and that the non-Arrhenius vacancy diffusion anomaly of ferromagnetic iron can be attributed to the effects of changed spin dynamics at the FM/PM phase boundary.

6.1 Chapter Introduction

6.1.1 Introductory remarks

Monovacancy (simply called vacancy in the following) is one of the simplest but most fundamental point defects in crystalline solids. As shown in Fig. 6.1, a vacancy refers to the vacant site left behind by an atom moved from its lattice site inside the crystal to the surface. Vacancies form due to the thermal vibration of atoms as an excited state of the crystal. They spontaneously exist in thermodynamic equilibrium in a concentration determined by its free energy of formation and the ambient temperature, or during irradiation by energetic particles such as neutrons and electrons, etc., as well as plastic deformation. The state of the vacancy is associated with the relaxation of the neighboring atoms or ions, the rearrangement of the electron distribution, the change in the vibrational dynamics, and so on. In this regard, the vacancy plays essential roles in the dimension, microstructure, and practically all physical properties of the crystalline solid [1]. Furthermore, vacancy migration is important as a facilitator of mass transport and microstructure evolution in a crystalline solid. Self-diffusion (or tracer diffusion), for example, is achieved via vacancy diffusion. A remarkably wide scope of effects can be traced to the migration of vacancies, ranging from irradiation damage accumulation [2,3], microelectronic circuit failures [4], to stress relaxation [5] and creep [6], embrittlement [7] and

fracture [8], and the list goes on. Indeed, the relevance of vacancies goes far beyond academic interest on the defect itself, and is linked to a large area of science and technology in the solid state. The comprehensive understanding of the above-mentioned issues with respect to vacancy can be achieved from classical textbooks such as Borg and Dienes [9], and Nowick and Burton [10], as well as the work of Woo and others [11,12]. The brief introduction of the theoretical description in vacancy is presented here.

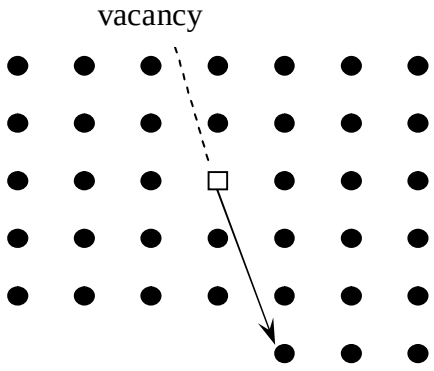

Fig. 6.1: Schematic of vacancy in crystalline solid.

In thermal equilibrium, the vacancy can exist in a solid with a temperature dependent concentration $C(T)$, i.e. $C(T) = e^{-F_F/k_B T}$, where $F_F = E_F - TS_F$ is the formation free energy, associated with the formation energy E_F required to break the bonds between an atom inside the crystal and its nearest neighbor atoms, and the heat dissipated in term of formation entropy S_F, during the vacancy creation process. In general, both E_F and S_F are temperature dependent. However, for metals that can be regarded as harmonic solids, e.g., BCC tungsten [13,14], these parameters are nearly temperature independent, over

a wide temperature range up to the melting point, so that the logarithm of the concentration is linearly proportional to the reciprocal of temperature, i.e. $\ln C(T) \propto 1/T$. In experiments, such a relation is often used to estimate E_F and S_F.

In another aspect, the diffusive displacement of the vacancy is described by the temperature dependent diffusion coefficient $D(T)$, associated with the average jump frequency $\nu(T)$. In general, the diffusion coefficient is a second rank tensor. For instance, the diffusivity tensor of vacancy in HCP crystal without external stress in the principle crystallographic system can be written as [15]

$$\boldsymbol{D} = \begin{pmatrix} D_a & 0 & 0 \\ 0 & D_a & 0 \\ 0 & 0 & D_c \end{pmatrix}, \tag{6.1}$$

where D_a and D_c are the diffusion coefficients along *a*-axis (in-plane) and *c*-axis (out-of-plane), respectively. However, the diffusivity tensor reduces to a scalar quantity in the case of cubic and isotropic lattices. Microscopically, $D(T)$ can be determined by the atomic information following the Einstein relation, i.e. in the isotropic case,

$$D = \frac{\overline{\Delta r^2}}{6\Delta t} \tag{6.2}$$

where $\overline{\Delta r^2}$ is the mean square displacement of the vacancy during the time interval Δt. Since the jump of vacancy is from one lattice site to another, the

jump length λ is unique in BCC structure, i.e. $\lambda = \sqrt{3}a/2$, a being the lattice parameter. Thus,

$$D = \nu a^2 / 8 . \tag{6.3}$$

The first investigation of ν was done by Eyring [16] via chemical reactions in gases, based on which West [17], Zener [18] and Vineyard [19] developed the "absolute" rate theory for crystals. In this model, the jump frequencies of the vacancy is related to its migration energy E_M and entropy S_M as

$$\begin{aligned} \nu(T) &= \nu_0 e^{-F_M/k_B T} \\ &= \nu_0 e^{-S_M/k_B} e^{-E_M/k_B T}, \end{aligned} \tag{6.4}$$

where ν_0 is called attempt frequency, F_M is the migration free energy, i.e. $F_M = E_M - TS_M$. As sketched as in Fig. 6.2, E_M corresponds to the potential barrier between the saddle point state (C) and the equilibrium state (A or B).

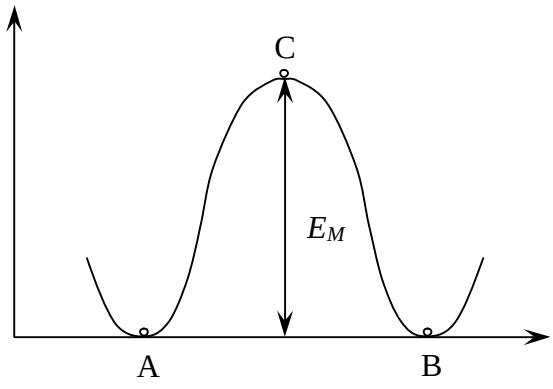

Fig. 6.2: The sketched migration energy during vacancy jump process.

For a stable crystal structure away from transitions, e.g., BCC tungsten, the atomic vibration can be assumed harmonic. Absent anharmonicity, the energy and entropy changes associated respectively with the statics and dynamics of the configuration change during the migratory process essentially only depends on the temperature independent interatomic potential. In this case, the Arrhenius plot of D is a straight line, as experimentally found in most simple metals with a non-spin-polarized electronic structure [13,14]. For instance, the self-diffusivity in BCC tungsten obtained from experimental measurement [20], as well as the atomistic calculations based on Ackland potential [21] and BND potential [22], respectively, shows linear Arrhenius-type behaviors in Fig. 6.3(a). Otherwise, due to anharmonicity arising from phonon softening [23,24], the Arrhenius plot of self-diffusivity in HCP Zirconium [23] shows the curvature near the structural phase transition point from HCP to BCC, as shown in Fig. 6.3(b).

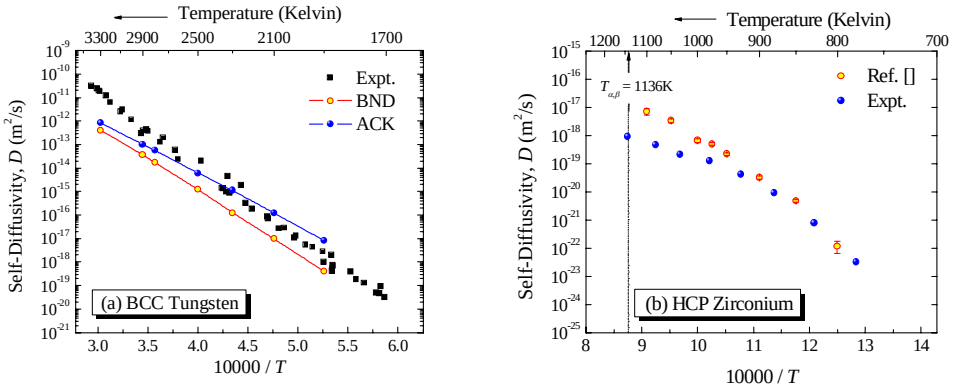

Fig. 6.3: The Arrhenius plot of self-diffusivity of (a) BCC tungsten and (b) HCP zirconium, obtained from experimental measurements and atomistic calculations based on the empirical interatomic potential. Here, “ACK” and “BND” respectively represent the Ackland [21] and BND [22] potentials used.

6.1.2 Vacancy in ferromagnetic iron

In Chapters IV and V, the participation of spin vibrations in the thermodynamics of ferromagnetic iron has been shown to produce extra anharmonicity arising from the phonon-magnon interaction, especially near the FM/PM phase boundary. Consequently, the corresponding entropy and enthalpy of self-diffusion are expected to be temperature dependent. The influence of magnetic effects was recognized since the 1960's. Borg and Birchenal [25] found the non-Arrhenius behavior of self-diffusion in his experiment with BCC iron. Later on, Hettich *et al.* [26] made more accurate measurement over a wide range temperature down to 259K below Curie temperature, and found a sharp change of slope near the FM/PM phase boundary The corresponding activation energy reduced from 2.9eV (FM) to 2.5eV (PM). This change is often discussed in the debate of whether vacancy or self-interstitial is responsible for the "stage III" resistivity recovery, a controversy that has lasted for fifty years [27,28,29,30,31]. The physical origin of this magnetic diffusion anomaly has been the subject of many investigations, which have been comprehensively reviewed up to year 1990 in Ref. [32].

The first model of self-diffusion in BCC iron was proposed by Zener [18], in which the activation free energy is related to the isothermal work done during the activation process in terms of the change in an appropriate elastic modulus, and

the temperature dependence of activation entropy and energy are expressed by the "so-called" Zener's equation. Varotsos *et al.* [33] then developed the $cB\Omega$ model based on the idea of Zener. However, the measured elastic constants of Dever [34] failed to support these continuum mechanical models, whereas the vacancy activation is associated with the local lattice distortion. On the other hand, in analogy to the atomic ordering transition in alloys, Girifalco and co-workers [35,36] added an empirical term proportional to the square of spontaneous magnetization, i.e. the mean magnetic moment (MM) per unit volume, to the non-magnetic migration enthalpy to taking into account the magnetic effects. Ruch *et al.* [37] fitted the diffusion data in self-diffusion experiment of iron, but failed to achieve the physical picture due to the empiricism involved. Besides, the short range magnetic order (SRMO) was neglected, despite its importance shown in Ising model predictions [38,39,40].

Across the magnetic phase boundaries, change of anharmonicity caused by the instability of the correlated spin dynamics (magnetic phase), and the coupling between the spin and lattice subsystems, could lead to important consequences. Therefore, while one may comfortably treat simple metals using *ab initio* calculations, modeling atomic processes in ferromagnetic iron across the FM/PM phase boundary could offer a much bigger challenge, particularly in regard to the thermodynamics involved [41]. In another aspect, a description of the finite-temperature behavior of electrons [42] with the Fermi distribution is

accurate when the interactions among the electrons, the spins and the lattice systems and their elementary excitations are sufficiently weak, which almost certainly excludes the strong-interaction regime near phase transitions. Being able to produce a thermodynamically accurate picture of the dynamical behavior of an atomic ensemble, MD calculations are widely used to study atomic processes. In the case of ferromagnetic materials with interacting spin and lattice subsystems, approximations involving either frozen spins [43], or frozen lattice (spin dynamics simulations [40]), have been used.

In the following Sections, based on the developed spin-lattice dynamics (SLD) scheme [44], the free energies of the lattice and spin subsystems in the activation processes of vacancy formation and migration are evaluated following the discussions in Section 3.3, by using the thermodynamic integration (TI) method [45,46,47]. The temperature-dependent enthalpies and entropies of vacancy formation and migration are then estimated to reveal the mechanism of magnetic effect on vacancy activation process in BCC iron.

6.2. Theory and Methodology

6.2.1. Hamiltonians

As discussed in Chapter III, the interactive spin and lattice coupling system, i.e. BCC iron, is described by H_H,

$$H_H = \sum_{i=1}^{N} \frac{\boldsymbol{p}_i^2}{2m} + U(\boldsymbol{R}) - \frac{1}{2}\sum_{i\neq j}^{N} J_{ij}(\boldsymbol{R})\boldsymbol{S}_i \cdot \boldsymbol{S}_j . \quad (6.5a)$$

Contributions from the lattice and spin vibrations to the respective free energies can be represents by the models H_L, H_S, and H_Δ, respectively,

$$H_L(\boldsymbol{R}) = \sum_{i=1}^{N} \frac{\boldsymbol{p}_i^2}{2m_i} + U(\boldsymbol{R}) \quad (6.5b)$$

$$H_S(\boldsymbol{S}) = -\frac{1}{2}\sum_{i\neq j}^{N} J_{ij}(\bar{\boldsymbol{R}})\boldsymbol{S}_i \cdot \boldsymbol{S}_j , \quad (6.5c)$$

$$H_\Delta(\boldsymbol{R},\boldsymbol{S}) = -\frac{1}{2}\sum_{i\neq j}^{N} \delta J_{ij}\boldsymbol{S}_i \cdot \boldsymbol{S}_j , \quad (6.5d)$$

where $U(\boldsymbol{R})$ is the interatomic potential, which can be derived from the Dudarev-Derlet (DD) potential [48] in the form as stated in Eq. (4.2).

6.2.2. Calculations of the diffusivity parameters

In the absolute rate theory [18,19,49], the self-diffusion coefficient D^{sd} via vacancy mechanism is defined in terms of the free energies of vacancy formation F_F and migration F_M and the attempt frequency ν_0,

$$D^{sd} = Z_f \frac{Z_m}{6} l^2 \nu_0 \exp\left(-\frac{F_F + F_M}{k_B T}\right) \quad (6.6)$$

where Z_f is the number of equivalent ways of forming a vacancy type, Z_m is the number of equivalent diffusion paths, and l is the jump distance. For a

mono-vacancy formation and migration in BCC structure, $Z_f = 1$, $Z_m = 8$ and $l = \sqrt{3}a/2$, with the lattice parameter a.

Based on the principles of statistical mechanics, the TI method is widely used to calculate the free energy of a canonical ensemble of atoms, from the phase-space trajectory, such as that derived from a MD-type simulation (See Section 3.3). Consequently, using the TI method, the activation probability of a thermodynamic process at a finite temperature T between two well-defined states is obtainable from the free energy difference. However, the difficulty of this approach is that the difference is usually very small compared with the intrinsic thermal fluctuations of a system containing a large number of atoms. This is especially true for the case of vacancy, where only a small number of atoms participate in this process. In the following, the TI method is modified to overcome this difficulty within the MD-type simulation scheme.

a) Vacancy migration free energy

Vacancy migration refers to the process in which an atom m in the vicinity of vacancy overcomes an energy barrier and performs a migratory jump into the vacant site. Following the statistical interpretation made by Vineyard [19], F_M is equal to the reversible work done required to bring the atomic system from equilibrium to the saddle-point state along a constrained path in the hyper-surface, with displacements along the migration direction forbidden. Indeed, such a

constraint approach is also adopted in the optimization numerical calculation, i.e. conjugated gradient (CG) method [50], for calculating the energy and configuration of the saddle point state, as well as the migration energy. In addition, the migration entropy in the usual harmonic approximation is also expressed via the vibration modes under this constraint condition.

Within the framework of the adiabatic switching TI method [51], the migration free energy can be obtained by performing dynamical atomistic simulations, in which the migrating atom m is slowly moved from its equilibrium lattice position $\boldsymbol{R}_m^e$ towards the saddle-point position $\boldsymbol{R}_m^s$ [52], along the path $\boldsymbol{R}_m^\lambda$, where

$$\boldsymbol{R}_m^\lambda = \boldsymbol{R}_m^e + \lambda\left(\boldsymbol{R}_m^s - \boldsymbol{R}_m^e\right), \tag{6.7}$$

by varying λ from 0 to 1. Here $\boldsymbol{R}_m^\lambda$ is treated as the switching parameter accompanying λ. During the switching process, the instantaneous position $\boldsymbol{R}_m$ of atom m is constrained in the following relation,

$$\left(\boldsymbol{R}_m \cdot \boldsymbol{n}\right)\boldsymbol{n} - \boldsymbol{R}_m^\lambda = 0 \tag{6.8}$$

where $\boldsymbol{n}$ is the unit jump displacement vector $\boldsymbol{R}_m^s - \boldsymbol{R}_m^e$. Consequently, the switching Hamiltonian H^λ can be defined as

$$H^\lambda = E_K + \tilde{U}^\lambda \tag{6.9}$$

where E_K is the kinetic energy and $\tilde{U}^{\lambda} \equiv \tilde{U}\left(\left\{\boldsymbol{R}_i \middle| \boldsymbol{R}_m^{\lambda}\right\}\right)$ is the constrained interatomic potential, in which all atoms are acted on by the atomic force due to $\tilde{U}^{\lambda}$, except the atom m is constrained according to Eq. (6.8). It should be noted that, in models involving the spin dynamics, i.e. H_H in Eq. (6.5a), $\tilde{U}^{\lambda}$ should be the sum of interatomic potential and the exchange interactions, i.e.

$$\tilde{U}^{\lambda} = U\left(\left\{\boldsymbol{R}_i \middle| \boldsymbol{R}_m^{\lambda}\right\}\right) - \frac{1}{2}\sum_{i\neq j}^{N} J_{ij}\left(\left\{\boldsymbol{R}_i \middle| \boldsymbol{R}_m^{\lambda}\right\}\right)\boldsymbol{S}_i \cdot \boldsymbol{S}_j \,. \tag{6.10}$$

It is clear that H^{λ} refers to the relaxed equilibrium state when $\lambda = 0$ and saddle-point state when $\lambda = 1$. In this regard, the free energy difference during the process, which is equal to the migration free energy F_M, can be derived as following based on Eq. (3.26),

$$\begin{aligned} F_M = \Delta F &= \int_0^1 \left\langle \frac{\partial H^{\lambda}}{\partial \lambda} \right\rangle_{\lambda} \mathrm{d}\lambda \\ &= \int_0^1 \left\langle \frac{\partial H^{\lambda}}{\partial \boldsymbol{r}_m} \cdot \frac{\partial \boldsymbol{r}_m}{\partial \lambda} \right\rangle_{\lambda} \mathrm{d}\lambda \\ &= \int_0^1 \left\langle -\boldsymbol{f}_m^{\lambda} \right\rangle_{\lambda} \cdot \left(\boldsymbol{R}_m^s - \boldsymbol{R}_m^e\right) \mathrm{d}\lambda \end{aligned} \tag{6.11}$$

where $\boldsymbol{f}_m^{\lambda} = -\nabla_{\boldsymbol{r}_m} H^{\lambda}$ is the force on atom m exerted by the surrounding atoms in the intermediate state λ. $\left\langle \boldsymbol{f}_m^{\lambda} \right\rangle_{\lambda}$ can be interpreted as the thermal force, so that the accumulated work done with the displacement $\left(\boldsymbol{R}_m^s - \boldsymbol{R}_m^e\right)$ can be expressed as

$$W(\lambda') = \int_0^{\lambda'} \left\langle -\boldsymbol{f}_m^{\lambda} \right\rangle_{\lambda} \cdot \left(\boldsymbol{R}_m^s - \boldsymbol{R}_m^e \right) \mathrm{d}\lambda , \tag{6.12}$$

when the atom m moves from $\boldsymbol{R}_m^e$ to $\boldsymbol{R}_m^{\lambda'}$. In this regard, the mechanic and thermodynamic interpretations of the TI process are consistent.

The starting position of atom m in the above-mentioned TI process should be $\boldsymbol{R}_m^e$, which is difficult to pre-determine in the dynamic simulation [52]. The reference perfect lattice position $\boldsymbol{R}_m^0$ of atom m is thus preferred in practice, from which the error introduced has been examined to be less than 1%. Moreover, the constraint mentioned above is enhanced by disallowing the velocity of atom m along the jump direction, and the in-plane relaxations and vibrations perpendicular to the jump direction are allowed, to ensure the system to reach the corresponding minimum free energy state of each H^{λ}.

The activation free energy from the spin subsystem, i.e. H_S in Eq. (6.5c), is estimated using the ensemble average TI method with the frozen lattice configuration. In this case, the Hamiltonians of initial and final states in Eq. (3.26) while implementing the TI method, are written as $H_0 \equiv H_S\left(\boldsymbol{R}^e\right)$ and $H_1 \equiv H_S\left(\boldsymbol{R}^s\right)$, where $\boldsymbol{R}^e \equiv \left\{\boldsymbol{R}_i^e\right\}$ and $\boldsymbol{R}^s \equiv \left\{\boldsymbol{R}_i^s\right\}$ are respectively the equilibrium and saddle point lattice configurations of H_H obtained from modified CG calculations [53]. The λ -Hamiltonian is defined as $H_{\lambda} = \lambda H_1 + (1-\lambda) H_0$ $(0 \le \lambda \le 1)$, which is different from the one used in lattice

dynamic estimations mentioned in Eq. (6.9). In addition, the average atomic volume used in the modified CG calculations is obtained by equilibrating the spin-lattice in H_H at corresponding temperatures under zero-pressure.

b) Attempt frequency

Vineyard interpreted [19] the attempt frequency ν_0 as an effective quantity having the unit of frequency, associated with the impact of vacancy migration on the phonon modes in harmonic approximation. Readers are referred to the detailed analysis in Ref. [19,54]. In atomistic simulations for a specific crystal, ν_0 is usually assumed to be temperature independent, and is estimated using either the Debye frequency, or Einstein frequency, or the lowest frequency peak in the vibrational spectrum along the diffusion direction [55]. Wen and Woo [52] suggested an alternate determination of ν_0 during adiabatic switching TI process for the calculation of migration free energy.

Because of thermal fluctuations, the actual vacancy migration paths are not unique. However, the most probable paths should still statistically concentrate near the constrained states with minimum free energy governed by H^λ defined in Eq. (6.9). In addition, selecting $\boldsymbol{R}_m^0$ rather than $\boldsymbol{R}_m^e$ as the starting position of atom m in Eq. (6.12) would result in a near-parabolic accumulated work-done curve. For instance, the calculated data points of accumulated work

done is plotted against the reduced atomic coordinate in Fig. 6.4 for the TI process of in-plane vacancy jump in hexagonal closed packed (HCP) Zr.

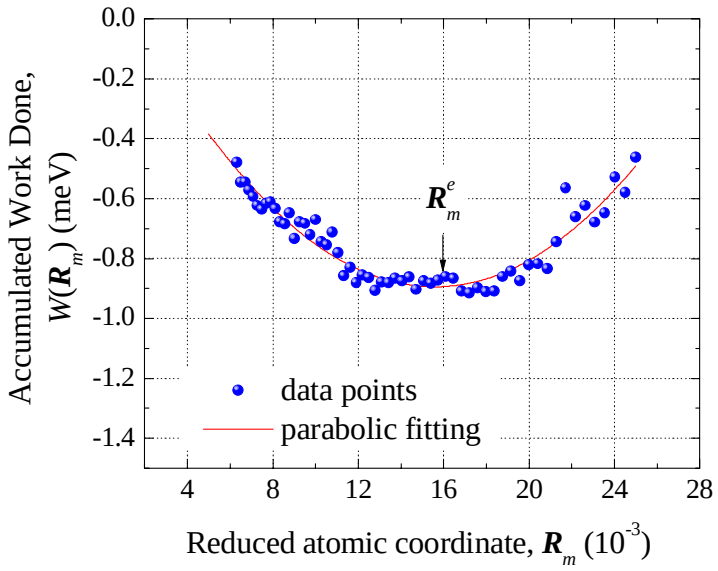

Fig. 6.4: The accumulated work done profile near $\boldsymbol{R}_m^e$ of the in-plane vacancy jump at 800K of HCP Zr during the adiabatic process of vacancy migration. Data points (solid points) are the calculation results following Eq. (6.12), with the least square parabolic fitting (solid line) following Eq. (6.13).

In this regard, ν_0 can be obtained from the fitting curvature around the minimum of $W(\boldsymbol{R}_m) \equiv W(\lambda')$, by assuming harmonicity, as

$$W(\boldsymbol{R}_m) \approx W(\boldsymbol{R}_m^e) + \frac{1}{2} m (2\pi\nu_0)^2 (\boldsymbol{R}_m - \boldsymbol{R}_m^e)^2 . \qquad (6.13)$$

The calculated ν_0 is found to be temperature dependent, and is associated with the crystalline structure, as well as the anharmonicity induced by multi-phonon interactions or other effects. For instance, Fig. 6.5 shows the temperature

dependence of ν_0 in both cases of in-plane and out-of plane jumps in HCP Zr, obtained from MD simulations. It can be seen that the calculated values of ν_0 following Eq. (6.10) are different from the corresponding Debye frequency, i.e. $\nu_D = 6.06\,\text{THz}$ of Zr [56]. In addition, the structural anisotropy of HCP Zr results in the different temperature dependences of ν_0 between in-plane and out-of-plane jumps. The strong decrease of ν_0 of the in-plane jump is believed to be caused by phonon softening near the structure phase transition boundary from HCP to BCC in Zr [52].

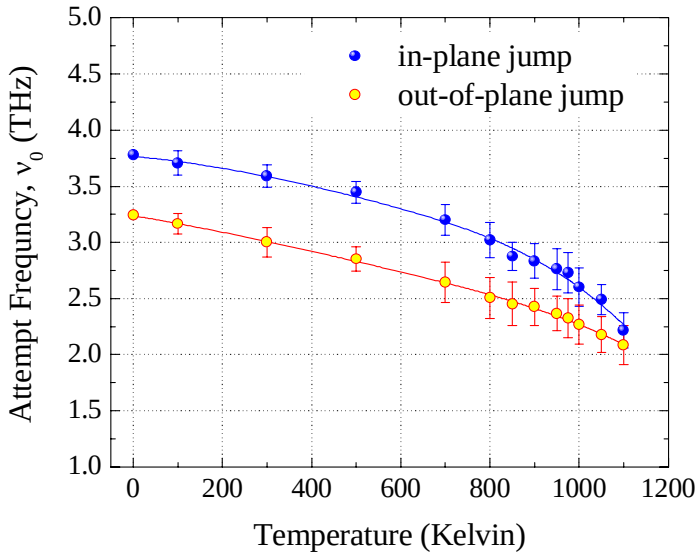

Fig. 6.5: The temperature dependence of vacancy attempt frequencies in both cases of in-plane and out-of-plane jumps in HCP Zr. Solid points are the calculation results following Eq. (6.13), while the solid lines are guides for eye.

c) Free energy of vacancy formation

In atomistic simulations built up with periodic boundary condition, F_F is usually defined as [57]

$$F_F = F_{N-1}^{vac} - \frac{N-1}{N} F_N^{per} \tag{6.14}$$

where F_{N-1}^{vac} is the free energy of the vacancy system containing $N-1$ atoms and a vacancy inside, and F_N^{per} is the free energy of the prefect system with N atoms. As stated in the foregoing paragraph, the straightforward estimation of F_F following Eq. (6.11) is prone to error arising from the intrinsic uncertainties due to the thermal fluctuation at finite temperatures. In this regard, the so-called vacancy creation approach [58] based on TI method is adopted in the current calculations, presented in the following.

Within the framework of TI method, a thermodynamic path is defined in the system of atoms connecting the initial and final states, in which all interactions between a specific atom α and all its neighboring atoms exist and vanish respectively. The free energy difference between them is equal to the formation free energy of vacancy. In this regard, the Hamiltonian during such a process can be defined by $H^\lambda = \lambda H^1 + (1-\lambda) H$, with $0 \le \lambda \le 1$, where

$$H^0 = E_K + \tilde{U}\left(\{\boldsymbol{R}_i, \boldsymbol{S}_i\}\right) \tag{6.15a}$$

$$H^1 = E_K + \tilde{U}\left(\{\boldsymbol{R}_i, \boldsymbol{S}_i\}_{i\neq\alpha}\right) + U_{ref} \tag{6.15b}$$

are the Hamiltonians of initial and final states, respectively. H^0 describes the perfect system containing N interactive atoms, and H^1 refers to the system with $N-1$ interactive atoms and atom α converted into a non-interacting reference atom described by the potential U_{ref}. Here the choice of reference potential depends on the degrees of freedom involved in the models, such as harmonic oscillator for lattice dynamics and paramagnet in an external field for spin dynamics, whose detail can be referred to the discussion in Chapter V.

In addition, the reference potential introduced is for the purpose of avoiding the divergence of free energy calculation. In practice, the presence of atom α tends to be oblivious to its neighboring atoms as $\lambda \to 1$, so that the distance between them may get too close, resulting in the divergence of the path integral [57,59]. To solve this problem, the velocities of the surrounding atoms are immediately reversed if motion into the vacancy is detected. Further, the switching process is only applied for $0 < \lambda < 0.9$. The ensemble average approach is applied to obtain the integrant for $0.9 < \lambda < 1$, meanwhile the cubic spline extrapolation approach is also suggested in Ref. [59]. Due to the insignificant difference in the final results, the former technique is adopted in the current calculation.

Consequently, the free energy difference in this thermodynamic process is obtained by

$$\begin{aligned}\Delta F &= \int_0^1 \left\langle \frac{\partial H^\lambda}{\partial \lambda} \right\rangle_\lambda \mathrm{d}\lambda \\ &= F_{N-1}^{vac} + \mu_{ref} - F_N^{per} \\ &= F_{N-1}^{vac} - \frac{N-1}{N} F_N^{per} + \mu_{ref} - \frac{1}{N} F_N^{per} \\ &= F_F + \mu_{ref} - \mu_b\end{aligned}, \tag{6.16}$$

where μ_{ref} and μ_b are the free energies of the reference atom and the single bulk atom governed by H^0, respectively, whose calculations are already done in Chapter V. F_F is then obtained by

$$F_F = \Delta F - \mu_{ref} + \mu_b . \tag{6.17}$$

d) Diffusivity via dynamical simulation

As stated in Section 6.1, the migration of vacancy can also be treated as a random-walk process of a single particle in a crystalline solid. Therefore, in an atomistic simulation, the vacancy jump frequency can be obtained from the waiting time t between jumps for each temperature in a series of NVT MD simulation runs [60]. Assuming an exponential distribution for the probability $p(t)$ of the waiting time t, i.e. $p(t) = \frac{1}{\tau} e^{-t/\tau}$, the mean waiting time $\tau(T)$ can be calculated by fitting to the simulation results, from which the mean successful vacancy jump frequency $\nu(T)$ at temperature T is calculated, thus the diffusion coefficient following Eq. (6.3).

6.3 Simulation Scheme

In the following calculations, the atomic system is set as containing 16000 iron atoms in a box of $20\times20\times20$ BCC unit cells in Cartesian coordinate system, with periodic boundary conditions applied to avoid surface effects. To ensure the complete relaxation of the spin and lattice degrees of freedom, at least 2 nano-seconds of equilibrium time is set in the canonical ensemble, realized by Langevin thermostat [44, 61] and quasi-harmonic approximation [62]. The equations of motion is solved by using Suzuki-Trotter decomposition [63] with a time-step of 1 femto-second. In the calculations of free energies, based on the equilibrium spin and lattice configurations, another 2 nano-seconds are applied for the adiabatic switching TI process, in which both forward and backward processes are performed. In addition, to facilitate dynamical measurement of the vacancy diffusion coefficient, at least 10 nano-seconds of sampling time are applied to obtain the stationary distribution of waiting time of vacancy jump.

6.4 Vacancy Migration and Formation Enthalpy and Entropy

6.4.1 Vacancy migration

The free energies of migration obtained using TI are plotted in Fig. 6.6 for various temperatures. F_M^L (for H_L) is calculated excluding spin dynamics and F_M^H (for H_H), including spin dynamics. The general trend for both F_M^L and F_M^H can be compared with the classic case in which both the entropy and enthalpy are constants, yielding a free energy versus temperature graph that is a straight line with negative slope. The curvatures seen in Fig. 6.6 signify

significant temperature dependency of the entropies and enthalpies. The effect of spin vibrations is most noticeable in the FM phase where there is long-range correlation. Away from the FM/PM transition temperature, spin vibrations apparently act to increase the entropy of the system. As one moves closer to the transition temperature, the entropy can be seen to increase faster than the energy, as the spin vibrations slowly lose their long-range correlation, leading to the large cusp of F_M^H near the magnetic phase transition at T_C. This will give rise to a discontinuous first temperature derivative [38,39,40]. Across the transition point in the PM phase, the effect of spin vibrations starts to disappear due to the loss of correlation of the spin vibrations. The ensuing temperature dependence is similar to that found in the elastic bulk modulus in experimental measurement. In Ref. [34], this discontinuity was attributed to the FM/PM phase transition of the spin-lattice coupled system.

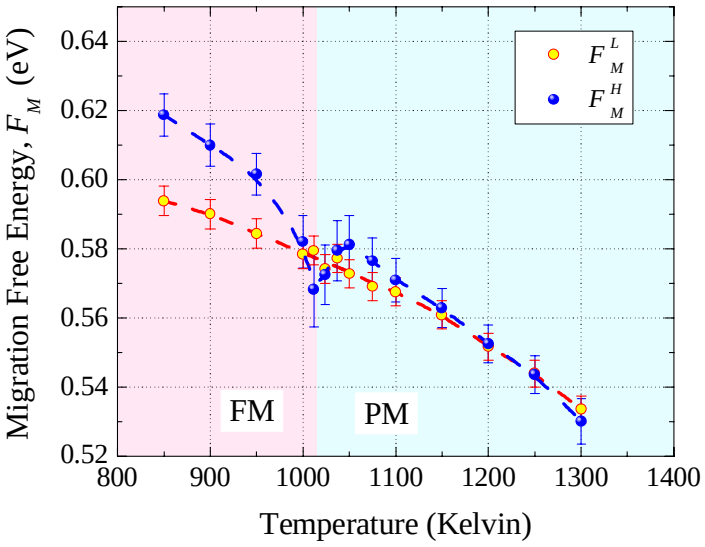

Fig. 6.6: The temperature dependence of migration free energies of vacancy calculated by using the modified TI method, without (H_L) and with (H_H) the influence of magnetic effects.

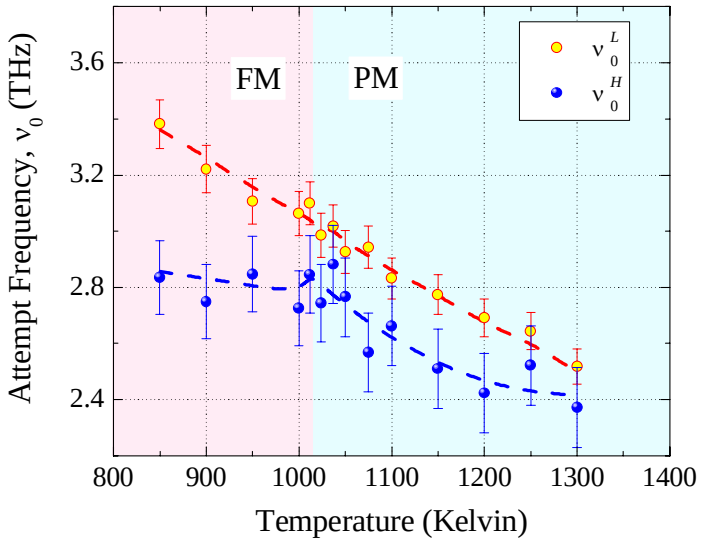

Fig. 6.7: The temperature dependence of attempt frequencies of vacancy migration derived from the work done during the corresponding adiabatic switching TI processes, without and with the impacts of magnetic effects, respectively, described by H_L and H_H.

Following Eq. (6.13), the attempt frequency of vacancy migration is derived from the corresponding work done during the adiabatic switching TI processes, which is plotted in Fig. 6.7, with and without spin vibrations. It can be seen that both ν_0^L and ν_0^H decrease with increasing temperature, i.e. from ~3.5THz at 850K to ~2.3 THz at 1300K for ν_0^L, and ~2.8THz at 850K to ~2.3 THz at 1300K for ν_0^H. With spin vibrations, ν_0^H is smaller than ν_0^L by about 10% to 20% in the temperature regime considered, showing the effects of the correlated spin vibrations in softening the crystal force constant that governs the lattice vibration frequencies [64]. Compared to the insignificant difference between F_M^L and F_M^H in the PM phase, the difference between ν_0^L and ν_0^H in the same regime demonstrates the complexity of the magnetic effect on the crystal potential. The values of the calculated attempt frequencies are only around one-third of the

Debye frequency of iron ($\nu_D = 9.385\,\mathrm{THz}$) [65] at room temperature. This is not surprising, since the Debye frequency is the largest frequency of phonon modes of the perfect crystal in the Debye model, whereas the attempt frequency of vacancy migration ν_0 is the most probable vibration frequency of the vacancy system at its ground state, closely related to the phase trajectory which is determined by the interatomic interaction and thermodynamic conditions (i.e. T and V) [19]. In this regard, the attempt frequency does not have to be close to the Debye frequency. In addition, with increasing temperature, thermal expansion of the atomic volume weakens the strength of the interatomic interaction, causing phonon softening [64], so that ν_0^L monotonically decreases. On the other hand, spin vibrations give rise to negative contribution of attempt frequency, as seen in Fig. 6.7. Moreover, enhanced interaction between the spin and lattice vibrations near the FM/PM phase boundary due to magnon softening results in the complicated temperature dependence of ν_0^H.

Vacancy diffusivities, D_L and D_H, obtained respectively from the waiting time and TI methods are compared in Fig. 6.8. The consistency between the results by these two independent methods is excellent, and lends credibility to the present methodology. Absent spin vibrations, vacancy diffusion coefficient D_L is a straight line in Arrhenius' plot. In comparison, the temperature dependent D_H shows an abrupt change of slope across the FM/PM phase boundary. This comparison clearly shows that the non-Arrhenius behavior is indeed a manifestation of the effect of correlated spin dynamics, particularly near the FM/PM transition [35,36,37].

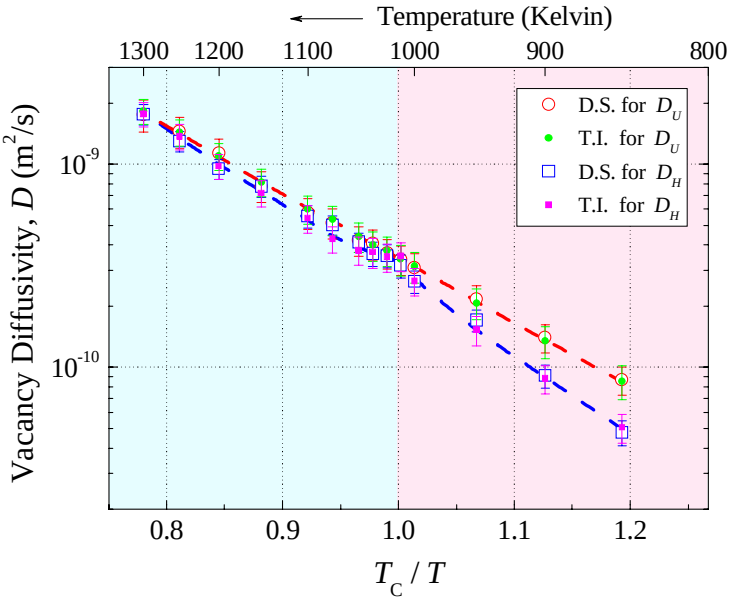

Fig. 6.8: The Arrhenius plot of vacancy diffusion coefficients obtained by both dynamical simulation (D.S. in the figure, open data points) measurements and TI method (T.I. in the figure, solid data points), respectively, of without (H_L) and with (H_H) the influence of magnetic effects. The solid lines are guides for eye.

The migration enthalpies, E_M^L and E_M^H, obtained by fitting to the slopes of the corresponding Arrhenius' plots in Fig. 6.5 [18], are given by

$$\ln\left(D_L\right) \approx \frac{0.64^{\pm 0.02}\,\text{eV}}{k_\text{B}T} - 14.08^{\pm 0.1}, \tag{6.18a}$$

and

$$\ln\left(D_H\right) \approx \begin{cases} \dfrac{0.82^{\pm 0.03}\,\text{eV}}{k_\text{B}T} - 12.10^{\pm 0.3}, & T < T_C \\ \dfrac{0.65^{\pm 0.02}\,\text{eV}}{k_\text{B}T} - 14.14^{\pm 0.2}, & T > T_C \end{cases}. \tag{6.18b}$$

In this regard, the fitted migration enthalpies are $Q_M^L = 0.64 \pm 0.02\,\text{eV}$ without

spin vibrations. Including the spin vibrations, the corresponding enthalpies change according to the spin correlations, with $Q_M^H = 0.82 \pm 0.03$ in the FM phase and $= 0.65 \pm 0.02$ eV in the PM phase. The migration entropies estimated from the pre-exponential factor $D_0 = Z_m \nu_0 a^2 / 8 \cdot e^{-S/k_B}$, are $S_M^L = 1.13 \pm 0.2 k_B$ without spin vibrations. When spin vibrations are taken into account, the spin correlation has a large impact on the entropy. In such cases, $S_M^H = 3.17 \pm 0.3$ in the FM phase and $= 1.24 \pm 0.2 k_B$ in the PM phase. It is clear that in the PM phase, where the long-range magnetic order due to correlation of the spin vibrations is lost, neither the entropy nor the and enthalpy [38,39,40] of the vacancy activation processes are affected. Our results are in good agreement with those obtained from resistivity recovery measurements [66,67] and with other simulation results [43,48,68,69,70,71,72], listed in Table 6.1. We emphasize that, Q and S obtained this way, from direct simulation by the Arrhenius-type fitting, are only valid assuming temperature independence.

6.4.2 Vacancy formation and self-diffusion

In the foregoing discussions, spin-dynamics is found to play an important role in vacancy migration In a similar way, spin vibrations are also expected to contribute to the vacancy formation and self-diffusion processes in BCC iron. To consider this possibility, we use the “so-called” vacancy creation approach to obtain the temperature-dependent formation free energies, i.e. F_F^L and F_F^H, via a TI approach. The results, with and without spin dynamics, are compared in Fig.

6.9, from which the impacts of spin dynamics can be measured.

In the temperature range from 850K to 1300K, F_F^L (without spin vibrations) is a linear function of temperature, decreasing from 1.56eV at 850K to 1.43eV at 1300K. With spin vibrations taken into account, F_F^H also follows a similarly decreasing trend with increasing temperature, falling from 1.63eV at 850K to 1.43eV at 1300K. However, the participation of spin vibrations generally increase the formation free energy, with a kink around T_C, which can be seen from Fig. 6.9. Similar to vacancy migration, the anomalous temperature dependence of F_F^H is believed to also come from the relaxation of spin subsystem during the vacancy formation process [35,36]. The current results are generally comparable to values obtained from positron annihilation experiments [73] and other simulations [48,69,70,73,74,75] (See in Table 6.1). It should be noted that, most of the formation enthalpy and entropy listed in Table 6.1 are obtained by subtracting the corresponding migration enthalpy and entropy from the corresponding self-diffusion entities, which are calculated by fitting the curves of Arrhenius plot in the same way as migration ones in Eqs. (6.18a) & (6.18b).

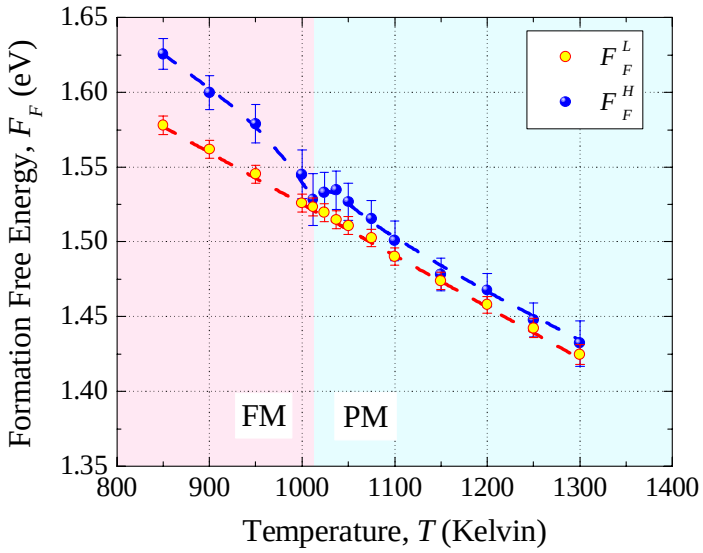

Fig. 6.9: The temperature dependence of vacancy formation free energies calculated by using the vacancy creation approach, without and with the influence of magnetic effects, respectively, described by H_L and H_H.

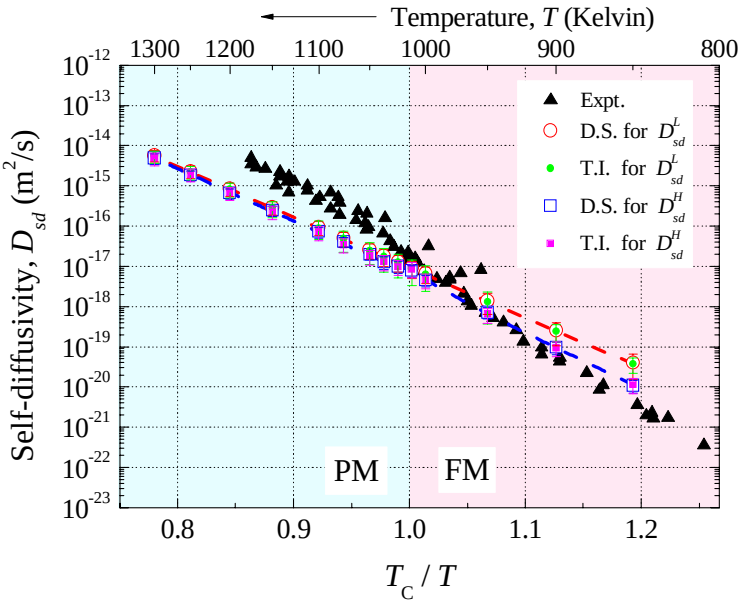

Fig. 6.10: The Arrhenius plot for Self-diffusion of BCC iron, calculated by direct simulation measurements (D.S. in the figure, open data points) and modified TI method (T.I. in the figure, solid data points), without and with the impacts of magnetic effects, respectively, described by H_L and H_H. A comparison with the experimental data (solid triangle) is also presented in this figure. The solid lines are guides for eye.

Finally, according to Eq. (6.6), the coefficients of self-diffusion obtained from wait-time in direct simulations (MD and SLD), TI method, and direct experimental measurements [25,26,32,76], are compared in Fig. 6.10. Compared to D_L^{sd}, the non-Arrhenius temperature dependence of $D_H^{sd}(T)$, of both TI calculation and dynamical simulation measurements near T_C, reveals that the presence of the long-range magnetic ordering from the correlated spin dynamics are indeed crucial to account for the self diffusion anomaly in BCC iron. Seen from Fig. 6.10, the calculated D_H^{sd} are quantitatively comparable with the self-diffusion experimental data, consistent with the expectation that self-diffusion in BCC iron is a vacancy mechanism, rather than an interstitial one. However, the values of D_H^{sd} in the PM phase are smaller than the corresponding experimental values [26,32,76,77], but with similar slopes (See in Table 6.1). We speculate that the migration entropy associated with the atomic vibrations is probably overestimated in the current calculations.

Thus, the free energies of formation and migration of mono-vacancy in α-iron, as well as the attempt frequencies for various temperatures are calculated, respectively with spin vibrations included and excluded. By simply fitting the resulting diffusion coefficients, the corresponding migration enthalpy and entropy are derived. Quantitative agreement with other calculated and experimental results is good. We found that it is the loss of long-range correlation in the spin vibrations across the FM/PM phase transition boundary which results in the slope change in both self- and mono-vacancy diffusion in α-iron. In these

results, the consistency between self-diffusion results and the corresponding experimental data shows that self-diffusion in α-iron is achieved by means of vacancy rather than self-interstitial. The smaller values of calculated self-diffusion coefficient at PM phase are speculated to be caused by the overestimation of the migration entropy, associated with the atomic vibrations governed by the used interatomic potential.

TABLE 6.1 The enthalpies and entropies of vacancy and self-diffusion

	H_L	H_H		Reference	
		FM	PM	FM	PM
E_M (eV)	0.64 ± 0.02	0.82 ± 0.03	0.65 ± 0.02	0.55 [66,67]	
				0.57~0.91 [43,48,69]	
E_F (eV)	1.87 ± 0.04	2.15 ± 0.07	1.91 ± 0.05	2.0 [73]	1.79~1.89 [73]
				1.81~2.18 [43,48,69]	
E_A (eV)	2.33 ± 0.02	2.97 ± 0.04	2.56 ± 0.03	2.87~3.02 [32,76]	2.57~2.68 [32,76]
				2.79~3.12 [48,68,69,70]	
S_M (k_B)	1.13 ± 0.2	3.17 ± 0.3	1.24 ± 0.2	2.3 [71], 2.06 [72]	
S_F (k_B)	3.71 ± 0.4	4.94 ± 0.8	3.81 ± 0.6	2.1 [74], 3.5[75]	
S_A (k_B)	4.84 ± 0.2	8.21 ± 1.1	5.05 ± 0.8	5.00 [77]	

6.5 Direct and Indirect Effects of Spin Vibrations

In the previous section, the participation of spin vibrations in BCC iron has been shown to be an important component in vacancy diffusion and self-diffusion. In the following, we will further consider the mechanistic details by separating such effects into those due to the spins alone, and others due to the interaction between the spin and lattice via the electron exchange interaction of nearby atoms.

6.5.1 Brief review

The energies of vacancy migration and formation are usually estimated using the Arrhenius law based on the assumed temperature independence of the enthalpy and entropy. However, this procedure is no longer valid if temperature dependence is strong. Flynn [78] proposed an empirical equation that can be used to derive the migration energy based on the continuum model, in which magnetic effects occur through lattice vibrations via the affected elastic constants. Schober *et al.* [79] suggested using the Green function to estimate the migration energy, but fail to consider the effects of spin dynamics. Such a difficulty is also faced in atomistic simulations using density functional theory (DFT). Although *ab initio* calculations can be performed to calculate E_M (or E_F) of BCC iron at the ground state (0K) [43], there is no appropriate method to include the dynamical effects needed to extend the validity to higher temperatures, such as near the

FM/PM transition. In this regard, many authors tend to adopt the Ruch's model [37], in which the magnetic contributions to E_M and E_F is taken into account within the framework of the molecular field approximation, i.e.

$$E_{M(F)}(T) = E^0_{M(F)} + \alpha_{M(F)} \frac{M^2(T)}{M^2(0)}, \tag{6.19}$$

where $E^0_{M(F)}$ is the non-magnetic contributions of the migration (formation) energy. $M(T)$ is the temperature dependent magnetization that vanishes in the PM state; $\alpha_{M(F)}$ is an empirical parameter, associated with the strength of exchange integral. Following Eq. (6.19), Pérez *et al.* [80] estimated E_M and E_F, as well as $\alpha_{M(F)}$ by fitting to the experimental data. However, the influence of short-range magnetic ordering (SRMO) [81,82], which does not vanish in the PM phase, is not taken into account. By using the Ising model, Fähnle *et al.* [38,39] and Khatun *et al.* [40] have demonstrated the importance of SRMO in both migration and formation processes of vacancy. In conventional MD simulations such as Mendelev *et al.* [83], there is no effective scheme to treat contributions from the spin dynamics [44].

In another aspect, in the harmonic approximation, migration/formation entropies can be expressed in terms of the phonon frequency change during the corresponding atomic process [19],

$$S_M = k_{\mathrm{B}} \ln\left\{ \prod_{i=1}^{3N-4} \omega_i^{vac} \Big/ \prod_{i=1}^{3N-4} \omega_i^{sad} \right\}, \tag{6.20a}$$

$$S_F = k_{\mathrm{B}} \left\{ \sum_{i=1}^{3(N-1)} \ln\left(\frac{k_{\mathrm{B}}T}{\hbar\omega_i^{vac}} \right) - \frac{N-1}{N} \sum_{i=1}^{3N} \ln\left(\frac{k_{\mathrm{B}}T}{\hbar\omega_i^{per}} \right) \right\}, \tag{6.20b}$$

where ω_i^{vac} is the ith normal frequency for the crystal containing a single vacancy with N lattice sites in the equilibrium state; ω_i^{sad} is the ith normal frequency for the same crystal in a saddle-point configuration, as shown in Fig. 6.2. ω_i^{per} stands for the frequencies in a non-vacancy crystal containing N atoms. Using Eq. (6.20b), Hatcher *et al.* [84] successfully calculated S_F for vacancy formation in BCC iron and obtained a value $\sim 2.1k_{\mathrm{B}}$. However, there is no direct calculation of S_M following Eq. (6.20a) [85], which is usually estimated by fitting to the Arrhenius plot of vacancy diffusion, either from experiments or atomic simulations. For example, Tsai *et al.* [86] performed molecular dynamics simulations to measure the vacancy diffusivity of BCC iron, but obtained a negative $S_M = -1.4k_{\mathrm{B}}$, which is in conflict with theoretical predictions. Mendelev *et al.* [83] considered the anharmonicity due to phonon-phonon interaction, and calculated both S_F and S_M but without the participation of spins.

Indeed, most of the first-principle calculations are performed with static spins in the fully ordered ferromagnetic state, where the activation energy and entropy of self-diffusion are estimated within the harmonic approximation. The

calculations, without accounting for the anharmonicity due to the spin dynamics, suffer from accuracy issues in the high temperature region, especially near the FM/PM phase boundary. We performed SLD simulation to investigate the role of spin dynamics in the temperature dependence of entropies and energies in vacancy migration and formation.

6.5.2 Direct contribution from spin dynamics

Fig. 6.11 (a) & (b) show the free energies of vacancy migration and formation, F_M and F_F, obtained from H_S in Eq. (6.5c) by using the modified TI method for a temperature range from 850K to 1300K. It can be seen that both F_M and F_F show similar temperature dependence, decreasing respectively from 17 to 1meV and from 80 to 5meV when the temperature increase from 850K to 1300K. The inflexions indicate the disappearance of long range magnetic ordering near T_C (~1020K in the current calculations). It should be noted that in H_S, there is not only the entropic information, but also the energetic dissipation due to the relaxation of the spin subsystem during the vacancy migration and formation processes.

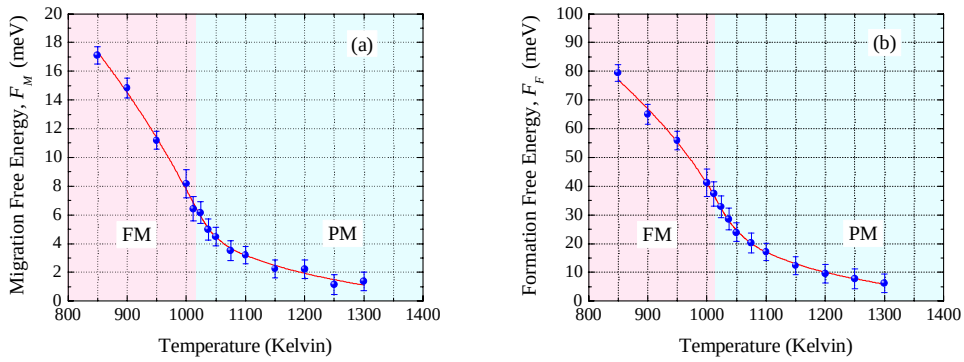

Fig. 6.11: The temperature dependence of free energies of (a) migration and (b) formation of vacancy in spin dynamics.

By differentiating the free energies with respect to temperature, i.e. $S_{M(F)} = -\partial F_{M(F)} / \partial T$, the corresponding entropies are obtained. As respectively shown in Fig. 6.12(a) & (b), both S_M and S_F show strong temperature dependence with a singular behavior near FM/PM phase boundary, which is believed to be the result of spontaneous magnetic phase transition in spin subsystem and the divergence of correlation length. From Figs. 6.12, it can be seen that the values of S_F, i.e. $\sim 2.0k_B$ at 850K and $\sim 5.0k_B$ near T_C, are about 4 times larger than that of S_M, i.e. $\sim 0.6k_B$ at 850K and $\sim 1.0k_B$ near T_C. The non-zero values in S_M and S_F reveals the importance of SRMO, as claimed by Fähnle *et al.* [38,39] and Khatun *et al.* [40]. Using the thermodynamic relation $E = F + TS$, the corresponding migration and formation energy due to the relaxation of spin subsystem can be obtained and plotted in Fig. 6.13(a) & (b), respectively. Similar to the entropies, cusps are present in

temperature dependent curves of E_M and E_F near T_C. E_F is around 5 times larger than E_M in the temperature range considered. The current calculations results about free energies, entropies and energies in vacancy migration and formation are quantitatively in good agreement with the theoretical prediction of two-dimensional Ising models [38,39,40].

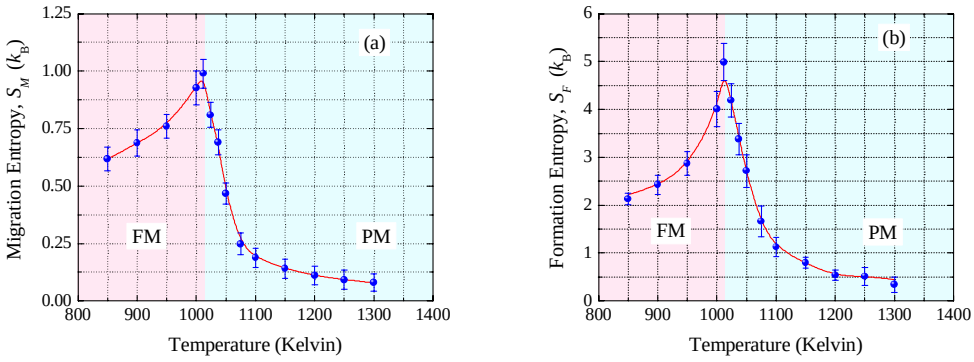

Fig. 6.12: The temperature dependence of (a) migration and (b) formation entropies due to the spin dynamics, derived from the free energies shown in Fig. 6.8. The results are in good agreement with the theoretical predictions by two-dimension Ising model.

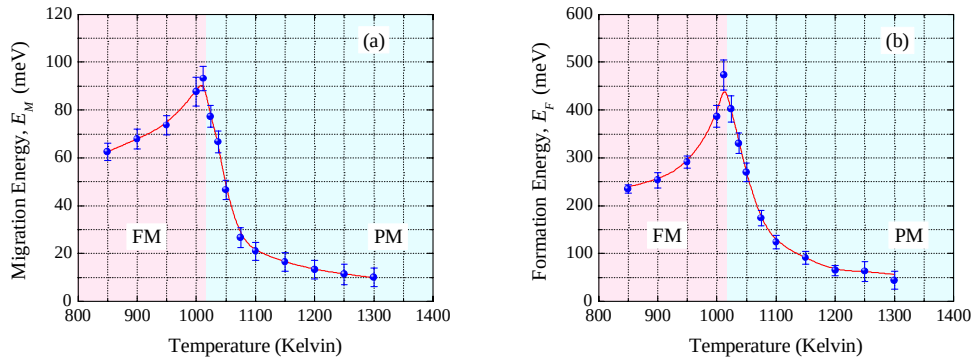

Fig. 6.13: The temperature dependence of (a) migration and (b) formation energies due to the spin dynamics, derived from the free energies shown in Fig. 6.8. The results are in good agreement with the theoretical predictions by two-dimension Ising model.

6.5.3 Indirect contribution from spin dynamics

Obtaining the free energies for spin subsystem, the contributions of the phonon-magnon interaction to the free energies in vacancy migration and formation processes can be estimated by comparing the results of H_{L+S} to that of H_H. Plotted in Fig. 6.14 (a) & (b), the temperature dependence of F_M and F_F are present, respectively, in the models of H_L, H_{L+S} and H_H. It can be seen that the results of H_{L+S}, either F_M^{L+S} or F_F^{L+S}, are comparable with those of H_H, in the whole temperature region except the cusps near FM/PM phase boundary, which indicates that the effects of phonon-magnon interaction is significant.

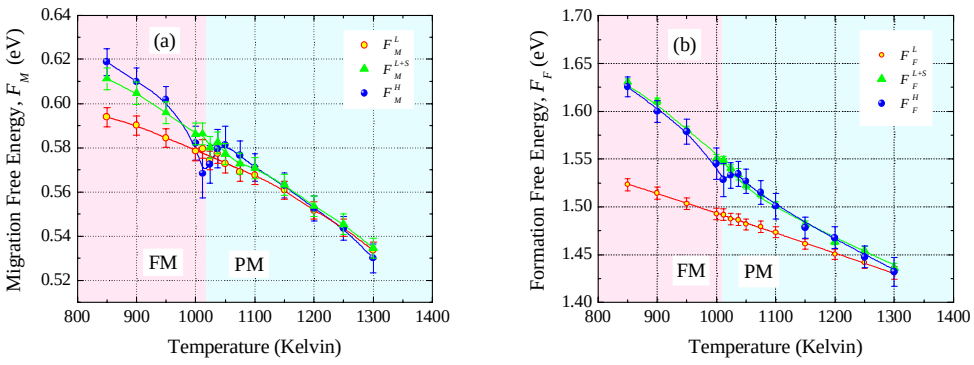

Fig. 6.14: The temperature dependence of free energies of vacancy (a) migration and (b) formation in H_L, H_{L+S} and H_H, respectively. The solid lines are guides for eye.

In principle, the energy of vacancy migration and formation, with respect to the lattice dynamics, can be also estimated by using the thermodynamic relation,

i.e. $E_{M(F)} = -\partial\left(F_{M(F)}/T\right)\Big/\partial\left(1/T\right)$. Nevertheless, the volume change during the vacancy migration should be taken into account, which is difficult to consider in the dynamical simulations. In addition, the energetic contributions originated from the changes in phonon modes during the vacancy migration and formation processes are regarded as the high order perturbation for transition metal [79]. Consequently, the change in potential energy in the above-mentioned atomic processes is the dominant one, which is consistent with the interpretation in absolute rate theory [17,18,19]. Therefore, in the current calculations, the migration energy is regarded as the static potential difference between the configurations of equilibrium and saddle point states generated by using the modified conjugated gradient (MCG) method [50,53], whereas the formation energy is treated as the energy difference between the relaxed vacancy equilibrium configuration and the corresponding non-defect configuration.

Fig. 6.15 (a) & (b) plot the temperature dependence of migration and formation energies in the models of H_L, H_{L+S} and H_H, respectively. Due to the anharmonicity originated from pure phonon-phonon interaction, both E_M^L and E_F^L linearly increase as temperature increasing, respectively, from 0.86eV and 1.91eV at 850K to 0.93eV and 1.95 eV at 1300K. The current results are comparable with the calculation results done by Mendelev *et al.* [83] by using quasi-harmonic approximation. In addition, the cusps present in the temperature dependent curves of F_M^H and F_F^H, due to the full dynamical interactions

between phonon and magnon excitations, demonstrate the effects of spontaneous FM/PM phase transition. Furthermore, the defined E_M^{L+S} and E_F^{L+S} represent the contributions from the non-interactive phonon and magnon excitations, i.e. $E_{M,F}^{L+S} = E_{M,F}^{L} + E_{M,F}^{S}$, from which the contributions due to the phonon-magnon interaction can be estimated by comparing to $E_{M,F}^{H}$. It can be seen that such interactive effect decreases the migration energy of ~0.06eV and decrease of formation energy of ~0.04eV, respectively, in the temperature range from 850 to 1300K. The values of the current calculation results are in good agreement with experimental data and other calculations, shown in Table 6.1.

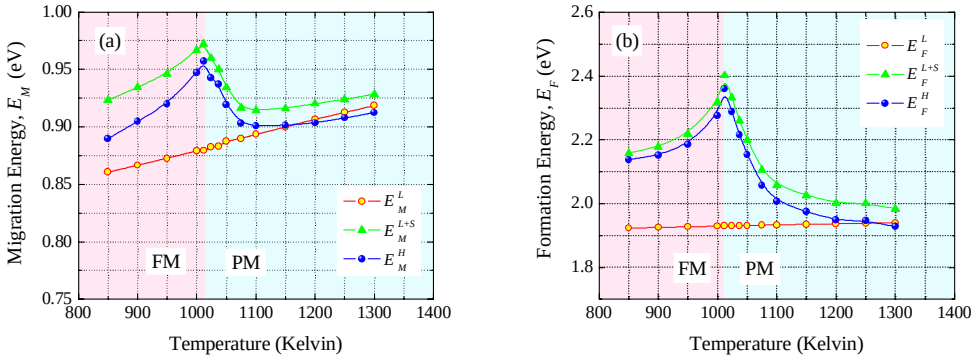

Fig. 6.15: The temperature dependence of vacancy (a) migration and (b) formation energies. The solid lines are guides for eye.

Similar to the energies, the entropies in vacancy migration and formation with respect to lattice dynamics is preferred by using the expression, i.e. $S_{M(F)} = \left(E_{M(F)} - F_{M(F)}\right)/T$, rather than $S_{M(F)} = -\left(\partial F_{M(F)} / \partial T\right)_V$ to avoid the error due to vacancy migration volume change during the migration (formation)

process. Fig. 6.16(a) & (b) show the temperature dependence of migration and formation entropies in the models of H_L, H_{L+S} and H_H, respectively.. In absence of the magnon excitations, both S_M^L and S_F^L reveal slightly linear temperature dependence in a wide temperature range, with the values of $\sim 3.2k_B$ and $\sim 4.0k_B$ respectively. In addition, the migration entropy due to magnon excitations S_M^S is around one-third of S_M^L, whereas S_F^S is as large as comparable to S_F^L in the FM phase, as shown in Figs. 6.13. That reveals the heat dissipation originated from the relaxation of spin subsystem is significant in the vacancy migration and formation processes. As a result, both S_M^{L+S} (or S_F^{L+S}) and S_M^H (or S_F^H) show the same temperature dependence, similar to that of S_M^S (or S_F^S), whose values is larger than S_M^L (or S_F^L) at low temperatures, but equal to S_M^L (or S_F^L) in the PM phase, due to the disappearance of the long range magnetic ordering. In addition, the difference between S_M^{L+S} (or S_F^{L+S}) and S_M^H (or S_F^H), due to the effect of phonon-magnon interaction, i.e. H_Δ in Eq. (6.1d), is very small to be negligible except at the temperature near T_C.

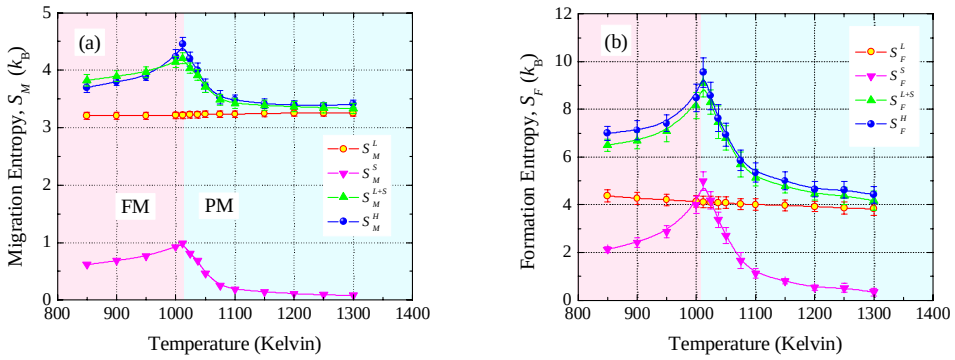

Fig. 6.16: The temperature dependence of (a) migration and (b) formation entropies. The solid lines are guides for eye

6.5.4 Brief conclusion

In summary, atomistic studies have been performed to discuss the effects of phonon and magnon excitations in vacancy migration and formation processes by using the modified thermodynamic integration (TI) method and modified conjugated gradient (MCG) method. The relaxation of spin subsystem gives rise to the strong temperature dependence of both entropies and energies in migration and formation, with a singular behavior near FM/PM phase boundary. This is a typical consequence originated from magnetic phase transition, which has been demonstrated by theoretical analysis in Ising model. In addition, the pure phonon-phonon interaction, giving rise to anharmonic effects, results in slightly temperature dependence in both entropies and energies. Furthermore, the effects due to phonon-magnon interaction have little contributions except near Curie temperature.

Reference

[1] G. J. Dienes, *Radiation effects in Solids*, Annual Reviews of Nuclear Science (Annual Reviews, Inc. Stanford, 1952), Vol. II.

[2] A. A. Semenov, C. H. Woo, and W. Frank, Appl. Phys. A **93**, 365 (2008).

[3] C. H. Woo, Radiat. Eff. Defects Solids **144**, 145 (1998).

[4] P. Borgesen, J. K. Lee, R. Gleixner, and C. Y. Li, Appl. Phys. Lett. **60**, 1706 (1992).

[5] N. Marzari, D. Vanderbilt, A. de Vita, and M. C. Payne, Phys. Rev. Lett. **82**, 3296 (1999).

[6] C. J. Vanderbeek, and P. H. Kes, Phys. Rev. B **43**, 13032 (1991).

[7] Y. Nagai, Z. Tang, M. Hassegawa, T. Kanai, and M. Saneyasu, Phys. Rev. B **63**, 134110 (2001).

[8] E. Hornbogen, and E. A. Starke, Acta Metall. **41**, 1 (1993).

[9] R. J. Borg and G. J. Dienes, *An Introduction to Solid State Diffusion*, (Academic Press, London, 1988).

[10] A. S. Nowick and J. J. Burton, *Diffusion in Solids: Recent Developments*, (Academic Press, New York, 1975).

[11] C. H. Woo, and E. J. McElroy (Eds.), J. Nucl. Mater. **159** (1988).

[12] C. H. Woo, *Modeling Irradiation Damage Accumulation in Crystals*, in: S. Yip (Ed.), *Handbook of Materials Modeling*, (Springer, Netherlands, 2005), pp. 959-986, and the references therein.

[13] J. Philibert, *Atom Movements – Diffusion and Mass Transport in Solids*, (Les Editions de Physique, 1991).

[14] H. Mehrer, *Diffusion in Solid Metals amd Alloys*, Vol. III/26 of Landolt-Bornstein, New Series, (Springer Verlag, 1997).

[15] C. H. Woo, and X. Liu, Philos. Mag. **87**, 2355 (2007).

[16] H. Eyring, J. Chem. Phys. **3**, 107 (1935).

[17] C. A. Wert, Phys. Rev. **79**, 601 (1950).

[18] C. Zener, in: *Imperfections in Nearly Perfect Crystals*, edited by W. Shockley, J. H. Hollomon, R. Maurer and F. Seitz, (John-Wiley & Sons, New York, 1952), pp. 289.

[19] G. H. Vineyard, J. Phys. Chem. Sol. **3**, 121 (1957).

[20] J. N. Mundy, S. J. Rothman, N. Q. Lam, H. A. Hoff, and L. J. Nowicki, Phys. Rev. B **18**, 6566 (1978)

[21] G. J. Ackland, and R. Thetford, Philos. Mag. A **56**, 15 (1987).

[22] C. Bjorkas, K. Nordlund, and S. Dudarev, Nuclear Instruments and Methods in Physics Research B **267**, 3204 (2009).

[23] J. Horvath, F. Dyment, and H. Mehrer, J. Nucl. Mater. **126**, 206 (1984).

[24] W. Frank, J. Nucl. Mater. **159**, 122 (1988).

[25] R. J. Borg, and C. E. Birchenall, Trans. Metall. Soc. A. I. M. E. **218**, 980 (1960).

[26] G. Hettich, H. Mehrer, and K. Maier, Script. Metal. **11**, 795 (1977).

[27] A. Seeger and M. Fähnle, in: *Computer Aided Innovation of New Materials II*, Eds. M. Doyama, J. Kihara, M. Tanaka, and R. Yamamoto, (North-Holland, Amsterdam, 1993), pp. 439.

[28] A. Seeger, Rad. Effects Defects Solids **111/112**, 355 (1989).

[29] W. Decker, J. Diehl, A. Dunlop, W. Frank, H. Kronmüller, W. Mensch, H.-E. Schaefer, B. Schendemann, A. Seeger, H.-P. Stark, F. Walz, and M. Weller, Phys. Stat. Sol. (a) **52**, 239 (1979).

[30] W. Frank, H.-J. Engell, and A. Seeger, Z. Metallk. **58**, 452 (1967).

[31] W. Frank, H.-J. Engell, and A. Seeger, Trans. Met. Soc. A.I.M.E. **242**, 749 (1968).

[32] M. Lübbehusen, and H. Mehrer, Acta Metal. Mater. **38**, 283 (1990).

[33] F. Vallianatos, Geologica Carpathica, **49**, 51 (1998).

[34] D. J. Dever, J. Appl. Phys. **43**, 3293 (1972).

[35] L. A. Girifalco, J. Phys. Chem. Solids **23**, 1171 (1962).

[36] M. Schoijet, and L. A. Girifalco, J. Phys. Chem. Solids **29**, 481 (1968).

[37] L. Ruch, D. R. Sain, H. L. Yeh, and L. A. Girifalco, J. Phys. Chem. Solids **37**, 649. (1976).

[38] M. Fähnle, and A. Seeger, Phys. Stat. Sol. (a) **91**, 609 (1985).

[39] M. Fähnle, and M. Khatun, Phys. Stat. Sol. (a) **126**, 109 (1991).

[40] M. Khatun, and J. W. Emert, Phys. Stat. Sol. (b) **231**, 341 (2002).

[41] M. Mantina, Y. Wang, R. Arroyave, L. Q. Chen, and Z. K. Liu, Phys. Rev. Lett. **100**, 215901 (2008).

[42] A. I. Lichtenstein, M. I. Katsnelson, and G. Kotliar, Phys Rev. Lett. **87**, 067205 (2001).

[43] C.-C. Fu, J. D. Torre, F. Willaime, J.-L. Bocquet, and A. Barbu, Nature Mater. **4**, 68 (2005).

[44] P.-W. Ma, C. H. Woo, and S. L. Dudarev, Phys. Rev. B **78**, 024434 (2008).

[45] J. G. Kirkwood, J. Chem. Phys. **3**, 300 (1935).

[46] D. Frenkel, and A. J. C. Ladd, J. Chem. Phys. **81**, 3118 (1984).

[47] G. Ciccotti, D. Frenkel and I. R. McDonald, *Simulation of Liquids and Solids: Molecular Dynamics and Monte Carlo Methods in Statistical Mechanics* (North-Holland, Amsterdam, 1987).

[48] S. L. Dudarev, and P. M. Derlet, J. Phys.: Condens. Mat. **17**, 7097 (2005).

[49] S. Glasstone, K. J. Laidler and H. Eyring: *The Theory of Rate Processes* (McGraw-Hill, New York and London 1941), pp. 1-27.

[50] J. E. Sinclair, and R. Fletcher, J. Phys. C **7**, 864 (1974).

[51] M. de Koning, and A. Antonelli, Phys. Rev. E **53**, 465 (1996).

[52] H. Wen, and C. H. Woo, J. Nucl. Mater. **420**, 362 (2012).

[53] C. H. Woo, and X. L. Liu, Philos. Mag. **87**, 2355 (2007).

[54] P. Wynblatt, J. Phys. Chem. Solids **30**, 2201 (1969).

[55] J. Ita, and R. E. Cohen, Phys. Rev. Lett. **79**, 3198 (1997).

[56] Q. Chen, and B. Sundman, Acta Materialia **49**, 947 (2001).

[57] M. de Koning, S. R. Debiaggi, and A. M. Monti, Phys. Rev. B **70**, 054105 (2004).

[58] E. Smargiassi, and P. A. Madden, Phys. Rev. B **51**, 117 (1995).

[59] S. Chiesa, P. M. Derlet, and S. L. Dudarev, Phys. Rev. B **79**, 214109 (2009).

[60] M. G. Ortega, S. R. Debiaggi, and A. M. Monti, Phys. Stat. Sol. (b) **234**, 506 (2002).

[61] W. F. Brown, Jr., Phys. Rev. **130**, 1677 (1963).

[62] G. Leibfried, and W. Ludwig, Solid State Physics **12**, 275 (1961).

[63] N. Hatano, and M. Suzuki, Lect. Notes Phys. **679**, 37 (2005).

[64] M. Born and K. Huang, *Dynamical Theory of Crystal Lattices*, (Oxford University Press, London, 1954), pp. 38-60.

[65] D. E. Gray (Editor), *American Institute of Physics Handbook*, 3rd ed. (McGraw-Hill, New York 1972), pp. 4-115.

[66] S. Takaki, J. Fuss, H. Kugler, U. Dedek, and H. Schultz, Radiat. Eff. **79**, 87 (1983).

[67] H. Schultz, *Landolt-Bornstien New Series, Group III*, Vol. **25**, edited by H. Ullmaier (Berlin: Springer) 1991.

[68] G. J. Ackland, D. J. Bacon, A. F. Calder, and T. Harry, Philos. Mag. A **75**, 713 (1997).

[69] C. S. Bequart, and C. Domain, Phys. Rev. B **65**, 024103 (2003).

[70] K. Tapasa, A. V. Barashev, D. J. Bacon, and Yu. N. Osetsky, Acta Mater. **55**, 1 (2007).

[71] N. Soneda, S. Ishino, A. Takahashi, and K. Dohi, J. Nucl. Mater. **323**, 169 (2003).

[72] V. A. Borodin, and P. V. Vladimirov, J. Nucl. Mater. **362**, 161 (2007).

[73] L. de Schepper, D. Segers, L. Dorikens-Vanpraet, M. Dorikens, G. Knuyt, L. M. Stals, and P. Moser, Phys. Rev. B **27**, 5257 (1983).

[74] R. D. Hatcher, R. Zeller, and P. H. Dederichs, Phys. Rev. B **39**, 5083 (1979).

[75] O. Seydel, G. Frohberg, and H. Wever, Phys. Stat. sol. (a) **144**, 69 (1994).

[76] Y. IIjima, K. Kimura, and K. Hirano, Acta Metall. **36**, 2811 (1988).

[77] A. Seeger, Phys. Stat. sol. (a) **167**, 289 (1998).

[78] C. P. Flynn, Phys. Rev. **171**, 682 (1968).

[79] H. R. Schober, W. Petry, and J. Trampenau, J. Phys.: Condens. Matter **4**, 9321 (1992).

[80] R. A. Pérez, and M. Weissmann, J. Phys.: Condens. Matter **16**, 7033 (2004).

[81] G. Hettich, H. Mehrer, and K. Maier, Scr. Metall. **11**, 795 (1977).

[82] J. Kučera, Czech. J. Phys. B **29**, 797 (1979).

[83] M. I. Mendelev, and Y. Mishin, Phys. Rev. B **80**, 144111 (2009).

[84] R. D. Hatcher, R. Zeller, and P. H. Dederichs, Phys. Rev. B **19**, 5083 (1979).

[85] S. Huang, D. L. Worthington, M. Asta, V. Ozolins, G. Ghosh, and P. K. Liaw, Acta Mat. **58**, 1982 (2010).

[86] D. H. Tsai, R. Bullough, and R. C. Perrin, J. Phys. C: Solid St. Phys. **3**, 2022 (1970).

CHAPTER VII

SUMMARY AND CONCLUSION

Spin-lattice dynamics (SLD) study of the effects of spin dynamics on the physical properties of BCC iron at finite temperatures, especially near the FM/PM phase transition point, have been performed in this thesis. Due to the anharmonicity of the crystal potential, lattice waves in BCC iron, i.e. phonons, soften (decreasing frequency) with shortened lifetimes as temperature increases. With anharmonic interaction between spins, spin waves (magnons) also behave similarly, especially near Curie temperatures, at which the characteristic frequencies and the lifetimes of magnons almost decrease to be zero, with the loss of the long range magnetic order. Interaction between the spin and the lattice caused by the exchange interaction of electrons with parallel spins between neighboring atoms, enhances phonon- and magnon-scattering, and results in more softening and shorter lifetime of both phonons and magnons. On the other hand, it is found that the spin-lattice coupling has little effects on the phonon dispersion relation, but affects the spin waves giving rise to a shift of Curie temperature from ~1100K to ~1000K. The temperature-dependent spin stiffness confirms such effects in spin dynamics, which is examined to be consistent with the theoretical predictions by mean-field theory.

By using the thermodynamic integration method, the free energies of BCC iron involving spin vibrations are calculated at finite temperatures, across Curie temperature. From the free energies, temperature-dependent vibrational energies and entropies and the related thermal, mechanical and magnetic properties are derived. The second-order nature of magnetic phase transition is shown in our results, e.g. the continuity of free energy, and the divergence of heat capacity near FM/PM phase boundary. In BCC iron, anomalous magnetic phenomena near the magnetic transition point are found to be results of spin-vibration enhanced anharmonicity. Examples are the complicated temperature dependence of thermal expansion coefficient, isothermal elastic constants, specific heat, as well as the Grüneisen parameter. Contributions from magnon excitations are particularly large compared with those from multi-phonon interactions. Moreover, the magnon excitations do not only provide the energetic contributions, but also the entropic contributions to the thermomechanical properties in BCC iron. For instance, the downward cusp in the curve of isothermal bulk modulus near Curie temperature is believed to be caused by the heat dissipation due to the microstates relaxation of magnons during the hydrostatic deformation process.

Based on SLD scheme, magnetic effects on the temperature dependence of self- and mono-vacancy diffusion in BCC iron have been studied. Using the modified thermodynamic integration method, the free energies in vacancy migration and formation are calculated at various temperatures, from which the

attempt frequency of vacancy migration is calculated for the first time atomistically. By simply fitting the resulting diffusion coefficients, the corresponding enthalpies and entropies of self- and mono-vacancy diffusion are calculated. Very good quantitative agreement with other calculation results and experimental data is obtained, which demonstrates the fact that the spin-lattice coupling gives rise to the magnetic diffusion anomaly near the FM/PM phase boundary, and self-diffusion in α-iron is indeed by means of vacancy rather than self-interstitial. The smaller values of calculated self-diffusion coefficients in the PM phase are speculated to be caused by the overestimation of the migration entropy, associated with the atomic vibrations governed by the used interatomic potential.

Furthermore, using the modified conjugated gradient method, the spin correlation effects on the temperature dependence of both entropies and enthalpies in vacancy formation and migration processes have been investigated over a wide temperature range, across the FM/PM phase boundary. The principal energetic contributions to vacancy migration and formation come from the changes in spin configurations, whereas no appreciable effects are provided by the spin-lattice coupling. Otherwise, the effects of frozen-magnon-enhanced phonon scattering and the spin-lattice coupling on entropies are not as important as the dynamical influence of spin correlation. Especially, the dynamical relaxation of spin configuration near the FM/PM phase boundary results in the

cusps of the temperature dependence of migration and formation entropy of vacancy, which is consistent with the theoretical predictions by the two-dimensional Ising models.

In a conclusion, due to the atomic distance dependent exchange interactions, the spin vibrations, varying with temperature due to the spontaneous phase transition in BCC iron, brings out the energetic and entropic contributions to the physical properties, i.e. thermodynamic, magneto-mechanic, and the properties related to point defects. In particular, the entropic effects are significant near the FM/PM phase boundary, which result in many anomalous magnetic phenomena.